Radiogalaxies with bent jets in a group of galaxies in the COSMOS field

Vulić, Paula

Master's thesis / Diplomski rad

2022

Degree Grantor / Ustanova koja je dodijelila akademski / stručni stupanj: **University of Zagreb, Faculty of Science / Sveučilište u Zagrebu, Prirodoslovno-matematički fakultet**

Permanent link / Trajna poveznica: https://urn.nsk.hr/urn:nbn:hr:217:579865

Rights / Prava: In copyright/Zaštićeno autorskim pravom.

Download date / Datum preuzimanja: **2025-03-13**

UNIVERSITY OF ZAGREB
FACULTY OF SCIENCE
DEPARTMENT OF PHYSICS

Paula Vulić

RADIO GALAXIES WITH BENT JETS IN A GROUP OF GALAXIES IN THE COSMOS FIELD

Master Thesis

Zagreb, 2022.

SVEUČILIŠTE U ZAGREBU
PRIRODOSLOVNO-MATEMATIČKI FAKULTET
FIZIČKI ODSJEK

Paula Vulić

RADIOGALAKSIJE SA SAVIJENIM
MLAZNICAMA U GRUPI GALAKSIJA U POLJU
COSMOS

Diplomski rad

Zagreb, 2022.

UNIVERSITY OF ZAGREB
FACULTY OF SCIENCE
DEPARTMENT OF PHYSICS

INTEGRATED UNDERGRADUATE AND GRADUATE UNIVERSITY
PROGRAMME IN PHYSICS

Paula Vulić

Master Thesis

Radio galaxies with bent jets in a group of galaxies in the COSMOS filed

Advisor: Professor Vernesa Smolčić, dr.sc.

Co-Advisor: Professor Matthew Bayliss, dr.sc.

Master Thesis grade: _____

Committee: 1. _____

2. _____

3. _____

Master Thesis defence date: _____

Zagreb, 2022.

Radiogalaksije sa savijenim mlaznicama u grupi galaksija u polju COSMOS

Sažetak

Tri radioizvora (10913, 44 i 4092) pronađeni su u polju COSMOS, unutar grupe galaksija na $z \approx 0.35$, prethodno detektirane u rendgenskom valnom području. Radiogalaksije 10913 i 44 imaju izduženu i zanimljivo oblikovanu radiomorfologiju (savijene mlaznice). Mi analiziramo galaksije i njihovo $10' \times 10'$ okruženje u optičkom valnom području. Modelirajući raspodjelu svjetla njihovih optičkih ekvivalenata Sersicovim profilom dobivamo vrijednosti Sersicovog indeksa: 3.946 ± 0.005, 4.77 ± 0.01 i 4.37 ± 0.02 za redom 10913, 44 i 4092. Prema rezultatima modeliranja, čini se kako su optički ekvivalenti radiogalaksija 10913 i 44 eliptične galaksije, moguće s jezgrom. Raspodjela svjetla u središnjem dijelu optičkog ekvivalenta radioizvora 4092 dobro slijedi Sersicov profil, međutim u vanjskim dijelovima galaksije ostaje rezidualno svjetlo, koje se treba dalje istražiti. Analizom prostorne raspodjele optičkih izvora u $10' \times 10'$ okolini radioizvora te izdvajanjem samo onih iz područja povećane gustoće, detektiramo veću nakupinu gusto raspoređenih galaksija koja se prostorno poklapa s prethodno detektiranom grupom u rendgenskom području te se sastoji od podstruktura. Nije uočena povezanost između indeksa boje galaksija članova i njihovog položaja unutar velike nakupine. Nađena je dugačka ($\approx 6 \, \mathrm{mag}$), gotovo vodoravna struktura širine $\approx 1 \, \mathrm{mag}$ u dijagramima magnituda - boja za galaksije, vjerojatno crveni niz. Precizniji rezultat te moguće bolje definiran (uži) crveni niz traže dodatnu analizu, uz uporabu preciznijih sprektroskopskih crvenih pomaka. Dobiveni rezultati su u skladu s idejom da je potencijalna grupa neopušten sustav, moguće opažen u procesu nastanka kroz spajanje više manjih grupa (vjerojatno po jedna oko svakog od radioizvora). Dodatno i u nekim aspektima naprednije istraživanje je potrebno, kako u optičkom području tako i na drugim valnim duljinama (radiovalno i rendgensko područje), kako bi se ova mogućnost dalje istražila.

Ključne riječi: aktivne galaktičke jezgre, radiogalaksije, savijene mlaznice, COSMOS, grupe galaksija, neopušteni sustavi, optičke valne duljine, profil svjetla, Voronoi teselacija, dijagrami magnituda-boja

Radio galaxies with bent jets in a group of galaxies in the COSMOS field

Abstract

Three radio sources (10913, 44, and 4092) are found in the COSMOS field within a massive galaxy group detected in X-ray at $z \approx 0.35$. Two of them, radio galaxies 10913 and 44, have extended and interestingly shaped radio morphologies, i.e. bent jets. We analyze the radio sources and their $10' \times 10'$ environment in the optical regime. Modeling the light distributions of their optical counterparts with the Sersic profile we obtain Sersic index values: 3.946 ± 0.005, 4.77 ± 0.01, and 4.37 ± 0.02 for 10913, 44, and 4092 respectively. The results of modeling suggest that the optical counterparts of radio galaxies 10913 and 44 are elliptical galaxies, possibly with a core. The light distribution in the central part of the optical counterpart of radio source 4092 follows the Sersic profile well. However, residual light in its outer parts remains and needs to be investigated further. By analyzing the spatial distribution of optical sources in the $10' \times 10'$ environment of radio sources and extracting the ones in highly dense areas, we detect a large concentration of densely distributed galaxies, that spatially corresponds to the group detected in X-ray, and that has substructures. The color index of the member galaxies does not seem to affect their position within the large concentration. We find a long ($\approx 6\,\mathrm{mag}$), nearly horizontal, and $\approx 1\,\mathrm{mag}$ wide structure - likely a red sequence in the corresponding galaxy color-magnitude diagrams. Using spectroscopic instead of photometric redshift in future work, would give more precise results and possibly better-defined (narrower) sequence. The obtained results agree with the idea of the potential galaxy group being a non-relaxed system, possibly caught in the process of its creation through the merging of more than one smaller group (likely around each radio source). Additional and in some aspects, more advanced research is needed in optical as well as at other wavelengths (radio, X-rays) to further investigate this scenario.

Keywords: active galactic nuclei, radio galaxies, bent jets, COSMOS, galaxy groups, non-relaxed systems, optical wavelenghts, light profile, Voronoi tessellation, color-magnitude diagrams

Contents

1 Introduction

1.1 *Active galactic nuclei*

Active galactic nuclei (AGNs) are astronomical sources known for their high luminosity, detected over the entire electromagnetic spectrum. Their bolometric luminosity[1] can rise to $L_{bol} \approx 10^{48} \, erg \, s^{-1}$, which can make them easily detectable at very high redshifts (up to $z \approx 7.1$) [25]. This high power emission comes from a small emitting region (in most bands), i.e. AGNs are compact objects, which implies high energy densities [25]. It is widely accepted that the emission from AGNs arises from the process of accretion onto the central supermassive black hole (SMBH) of the corresponding galaxy. AGNs span a wide range of different morphologies and dynamical properties, which is often referred to as AGN zoo. However, such diversity is only partially related to intrinsic differences between AGNs, and is also a consequence of differences in astrophysical parameters such as their orientation, accretion rate, presence of strong jets as well as their environment [25]. Ongoing efforts to better understand the physics behind AGNs, and their role in galaxy evolution primarily rely on various wavelength regimes being able to provide different windows on the matter.

1.1.1 Accretion process

Energy in AGNs is produced through processes connected to the central black hole. The only mechanism of energy production that has an efficiency high enough so that luminosities of order $\approx 10^{47} - 10^{48} \, erg \, s^{-1}$ could be observed is gravitation [32]. Matter (plasma) is being attracted, and it falls onto the central black hole, thereby losing its gravitational potential energy, i.e. converting it to kinetic energy. Since the infalling gas in general has finite angular momentum, it can not just fall straight onto the black hole, but instead an accretion disk forms, perpendicular to the angular momentum vector. The disk rotates like a Keppler disk, i.e. differentially since its angular velocity depends on the radius. This causes some friction in the disk and a part of the kinetic energy of the rotating matter converts to heat and gets emitted through thermal radiation [32]. During this process, the matter is slowly, however,

---

[1]The total amount of energy emitted per second by an astronomical source, in all forms and at all wavelengths

constantly losing its angular momentum, and therefore it is moving inwards to lower orbits until it eventually falls onto the black hole [32]. This inward motion moves the whole process forward, encouraging further conversion of gravitational potential energy to kinetic energy, and ultimately to heat [32]. Thermal radiation of the disk in an AGN extends to the UV or soft X-ray range [32].

The above-described emission process assumes that the disk is optically thick[2], so that the energy can be emitted locally. In AGNs where the disk is not optically thick, and therefore the emission process is not very efficient, the generated heat is being advected inwards together with the gas instead of being radiated away [32]. However, it is assumed that this is precisely what favors the generation of outflows from the central part of the AGN, i.e. the formation of jets [32] (see section 1.2.2).

1.2   Radio galaxies

Radio galaxies are the type of AGNs that stand out for their increased emission at the radio wavelengths ($\approx$ 10 MHz - $\approx$ 10 GHz). In section 1.2.1 we explain the origin of this radio emission, while different morphologies of radio emission are presented in section 1.2.2. Section 1.2.3 deals with the optical counterparts of radio galaxies - bright host galaxies, and we introduce a special type of radio galaxies - namely wide angle tail galaxies in section 1.2.4.

1.2.1   Emission from radio galaxies

The high radio luminosity, that we observe from radio galaxies, is mostly due to synchrotron emission. This non-thermal emission comes from relativistic electrons moving in a magnetic field [42] (as illustrated in the top panel of figure 1.1). The observed synchrotron emission is a superposition of emission from single electrons [37] (as shown in the bottom panel of figure 1.1). It is linearly polarised, and it has a continuum spectrum with the flux density (flux per unit frequency F_ν expressed in Jy, mJy, etc.[3]) depending on frequency (ν) according to [41]:

$$F_\nu \propto \nu^{-\alpha} \tag{1.1}$$

---

[2]Once generated, photons can not easily escape the medium, as opposed to optically thin.
[3]1 Jy (jansky) is equivalent to $10^{-26} \ W/m^2/Hz$

In the expression (1.1), α is the spectral index - a measure of a radio spectral energy distribution slope in the log-log plane [41] :

$$\alpha = -\frac{\partial \log F_\nu}{\partial \log \nu} \qquad (1.2)$$
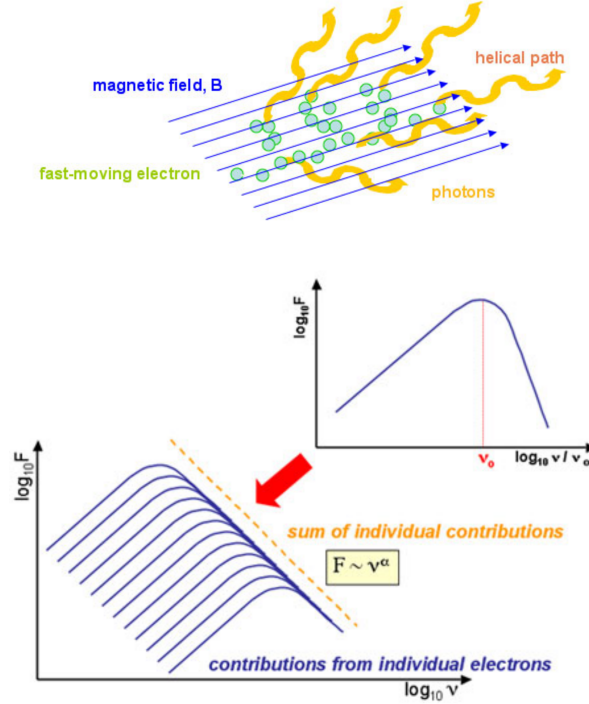
Figure 1.1: Electrons in plasma follow helical paths, emitting synchrotron radiation. Image credits: Swinburne University of Technology [37].

The spectral index is an important tool in the radio analysis of sources. It is commonly used to distinguish between different mechanisms of radio production in sources. A steep spectrum ($\alpha \gtrsim 0.5$) is due to the synchrotron emission of relativistic electrons, while a flat spectrum ($\alpha \lesssim 0.5$) is a sign of a thermal bremsstrahlung emission from HII regions [46]. However, it is also typical for the synchrotron emission in a central AGN region of radio galaxies. The source of synchrotron radiation in AGNs (and therefore also in radio galaxies) are processes related to the central SMBH. Except for this, synchrotron radiation in galaxies can be due to supernova remnants, in which case we are referring to star-forming galaxies (SFGs) instead of AGNs [25]. Although synchrotron radiation accounts for most of the radio emission from either AGNs or SFGs, it can also be detected in optical to X-ray in some quasars[4].

---

[4]Quasars (quasi-stellar objects) are a type of AGNs. They are very luminous, typically found at very high redshifts, and known for their extremely broad emission lines due to very high random velocities of the gas.

Along with the radio synchrotron radiation, the inverse-Compton process plays an important role in forming the total observed emission from radio galaxies. This radiation is a consequence of relativistic electrons interacting with photons, and causing them to Thompson-scatter to high energies [42] (visible in optical and/or X-ray).

1.2.2 Morphology of radio emission

Depending on the extent of their radio emission, radio sources can roughly be classified as point sources or extended sources. The morphology, in the radio regime, depends on the observed frequency and can often be very complex, consisting of several extended source components and a compact central one [32]. For extended radio morphologies the Fanaroff-Riley (FR) classification exists [7], dividing sources into edge-darkened (FR-I) and edge-brightened (FR-II) (see figure 1.2 and its description). This classification scheme is widely accepted and commonly used.
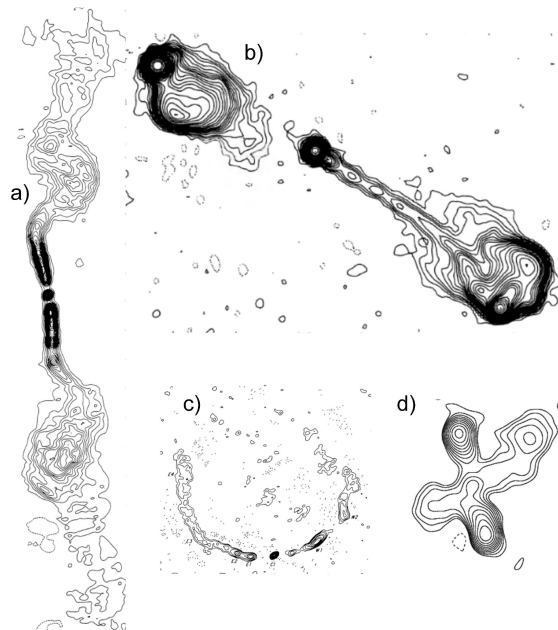
Figure 1.2: Different radio morphologies: a) A typical example of FRI type source with the central part being brighter than the edges, b) A typical example of FRII type source with bright edges, c) An example of C- shaped WAT galaxy, d) An example of X-shaped morphology. The image was adopted from [25].

We usually observe the extended components as jets, hotspots, and lobes. Figure 1.2 b) displays a radio galaxy of type FRII, highlighting all of the mentioned radio features. Jets are narrow and long radio features, originating from collimated flows of charged plasma flowing out from the central AGN. The radio jets are feeding lobes - clouds of diffuse radio emission, that mostly come in pairs and are placed on either

side of the active nucleus [42]. The jets of very luminous sources often terminate in bright hotspots in the lobes. The appearance of the bright hotspots, which are usually seen in FRII sources, is believed to be a manifestation of shocks, formed when the high-velocity jet (speeds higher than the speed of sound in plasma) abruptly terminates at the end of the source [5]. Referring to bent or wrapped appearances of radio galaxies, one can further classify sources as wide-angle tail, narrow-angle tail, X-shaped, etc. (again, see figure 1.2)

1.2.3   Bright ellipticals hosting radio galaxies

AGNs are the central engine of normal galaxies - their host galaxies. Radio galaxies were the first sources identified with optical counterparts in the early radio surveys [32]. Their host galaxies are essentially large elliptical galaxies. There are a few main characteristics of ellipticals. Firstly, boxy ellipticals (bright and dwarf elliptical galaxies) have spherical or ovoid shapes which they ought to the randomness of stellar orbits[5], i.e. they are velocity dispersion supported. This is different from disky ellipticals which are, as spiral galaxies, supported by rotation. The shape of ellipticals is characterized by two parameters, namely projected lengths of semi-major and semi-minor axes on the sky [38] (see figure 1.3). Secondly, they have a low content of interstellar matter[6], and consequently little or no star formation, i.e. they are being dominated by the old stellar population [44]. The latter results in ellipticals being red[7]. Ellipticals span a wide range in sizes, luminosities and masses [38]: from dwarf-ellipticals with an effective radius going down to $0.3\,\mathrm{kpc}$ ($L \approx 10^5\,L_\odot$, $M \approx 10^7\,M_\odot$, where $L_\odot$ and $M_\odot$ are luminosity and mass of the Sun), to giant elliptical galaxies found in the centers of galaxy clusters that can reach values in hundreds of kpc ($L \approx 10^{13}\,L_\odot$, $M \approx 10^{13}\,M_\odot$) [38]. The luminosity profiles $I(R)$ (where I is the intensity of light, and R is the projected distance from the center of the galaxy) of elliptical galaxies are usually well fit by Sersic's law [44; 43]:

$$I(R) = I_e \exp\left\{ - b_n \left[\left(\frac{R}{R_e} \right)^{1/n} - 1 \right] \right\} \tag{1.3}$$

---

[5]There are as many stars orbiting in one direction as there are orbiting in the opposite

[6]Gas and dust filling the space in between the stars in a galaxy. This material is constantly being ejected from the existing stars, especially in supernova explosions, and new stars are being created from it under the right conditions.

[7]The light observed from elliptical galaxies is shifted towards the red end of the spectrum compared to the light from spiral galaxies.

Here, n is the Sersic index describing how steep the light profile is. The case of $n = 1$ corresponds to the exponential profile, while $n = 4$ corresponds to the deVaucouleur profile. R_e is the effective radius, i.e. the radius containing the half of the galaxy's light and b_n is a parameter that depends on n. I_e is the intensity of the light at the radius R_e.

Massive ellipticals are often found surrounded by other (usually smaller) galaxies, i.e. in the centers of clusters or groups of galaxies where they reside at the bottom of the gravitational potential well, which is further explained in section 1.3 - Clusters and groups of galaxies.
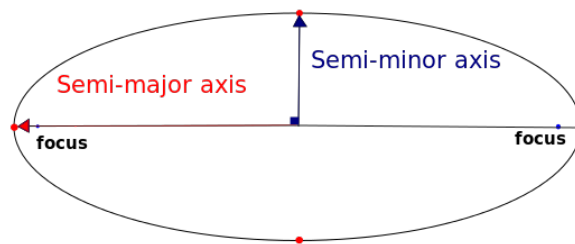
Figure 1.3: An ideal representation of the elliptical shape of a galaxy. In this work, semi-minor axes are denoted as a, while semi-major are denoted as b.

1.2.4 Wide angle tail galaxies

One special kind of radio galaxy is the so-called wide-angle tail (WAT) radio galaxy (see figure 1.2 c). WATs are essentially found in galaxy clusters (and are therefore being used to search for them, especially at larger redshifts (and up to $z \approx 1$) where other methods fail in preciseness and sensitivity[8] [32; 34]), and their jets are bent forming a C-shape. Previous studies of WAT galaxies show that their host (optical counterpart) is usually elliptical, the most luminous galaxy in the cluster - the brightest cluster galaxy (BCG) [3]. Often, radio galaxies in clusters have a different radio morphology compared to isolated ones since their components (jets) interact with the intracluster medium (ICM) and are affected by it. The jets will bend under the so-called ram pressure if the galaxy is moving at a significant velocity relative to the ICM [32]. According to previous research, this kind of interaction with the ICM is believed to cause the bending in WATs [2]. However, for the ram-pressure to bend the jets into a C-shape, much larger velocities of the WAT host galaxies relative to

---

[8]for clusters at high redshift we are biased by the dimming of galaxies in the optical and the ICM in X-ray emission

the ICM are needed than what is observed for BCGs [20; 1; 23] that are generally found at rest, close to the centers of clusters. The solution was suggested, in numerous studies, that the necessary pressure can be provided through cluster mergers [27; 19; 8; 29; 30]. During the cluster merger, the kinetic energy of the intracluster medium, which is mostly gas, would quickly dissipate, causing the two separate gaseous components to merge into a single one. On the other hand, the radio galaxy will not be decelerated at the same rate as the surrounding ICM, i.e. it will be kicked into motion with respect to the ICM [30]. Studies have reported that the BCGs that host WATs are usually misplaced from the center of cluster [30], and that clusters hosting the WAT galaxy often have significant substructure observed in X-ray [8] (substructure in ICM[9]) implying that the systems are not relaxed nor spherically symmetric. Several WAT galaxies and their environments have been investigated in the COSMOS field ([34], [24]). In these studies, environment analysis shows indications of group merger events, i.e. signs of intensive dynamics.

1.3 Clusters and groups of galaxies

Galaxies tend to gather in larger systems of galaxies. One can distinguish between galaxy groups (up to ≈ 50 members with the total mass going up to $\approx 10^{13}$ $M_\odot$) and galaxy clusters (more than ≈ 50 members with the total mass up to $\approx 10^{15}$ $M_\odot$) [32]. The transition between groups and clusters is smooth. They can be parts of even bigger structures as superclusters (groups of smaller galaxy clusters and groups), and they bind gravitationally into galaxy filaments that form large-scale structure (a net) of the Universe, according to the Cold dark matter model (CMD model) [32]. Groups and clusters do not only consist of stars in galaxies, and in between them (intra-cluster light). This only makes about $\approx 3\%$ of the total cluster mass. They also contain the intra-cluster medium (ICM) (baryonic matter[10] contained in the ICM contributes with about $\approx 15\%$) and they mostly consist of dark matter (about $\approx 80\%$) [32]. These systems are ideal laboratories to study interactions between galaxies and how that affects the galaxy population because of their high galaxy number density (compared to the rest of the Universe) [32].

---

[9]emission from the ICM is observed at X-ray wavelenghts

[10]Strictly, this is matter composed of baryons, i.e. protons, neutrons, and everything composed of them (atomic nuclei). In astrophysics, this term refers to all objects made of normal atomic matter, essentially ignoring the presence of electrons which, after all, represent only a small part of the mass.

1.3.1 Dynamics of a system

The aforementioned systems of galaxies are well described by the model of the gravitational potential well of the group/cluster. Usually, the massive systems have one, dominant central galaxy - namely the brightest cluster galaxy (BCG) that resides at the bottom of this gravitational potential well. However, the latter is only a characteristic of virialized galaxy systems. Clusters being virialized means that the collapse of matter has finished and the formation process of the galaxy cluster has completed [28].
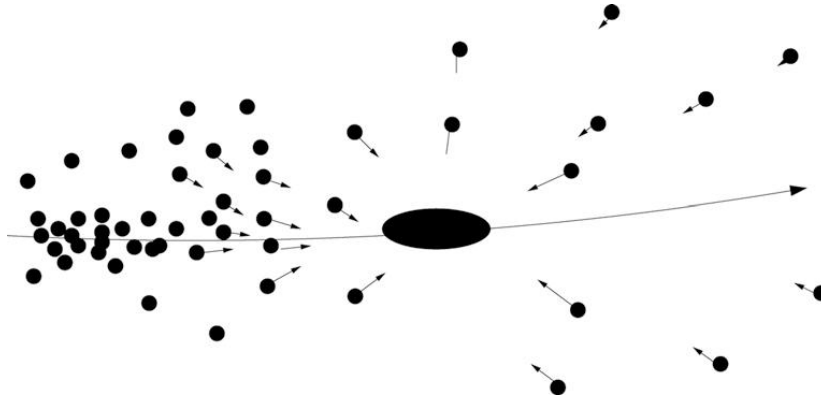
Figure 1.4: A visual representation of the dynamic friction mechanism.

Such a cluster is relaxed and it is often called a regular cluster, as opposed to irregular clusters that are still in the process of evolution. The main mechanism responsible for BCG being dragged down to rest at the center of the system is so-called dynamical friction. Through this process, an overdensity of mass establishes along the track of a more massive object moving through a statistically homogenous distribution of less massive objects. Therefore, originating from that overdensity, the gravitational field appears that slows down the more massive object, i.e. a massive galaxy gets dragged down to the bottom of the cluster's potential well [32] (see figure 1.4). Dynamical friction is a collective process. Generally, the dynamics of a galaxy cluster is governed by its collective gravitational potential, i.e. through collective processes that take place in clusters. Another important example is violent relaxation - a process that happens during a gravitational collapse of a mass concentration. This process helps to quickly establish a virial equilibrium (all galaxies obtain the same velocity distribution by this process) [32].

1.3.2 Intra-cluster medium

The space between the galaxies in a group or a cluster is filled with the intra-cluster medium (ICM), a hot, diffuse gas mostly consisting of ionized hydrogen and helium. The temperature of this medium is typically of order 10^7 K (for a cluster with $M \approx 10^{13} \, M_\odot$) and it can go up to the order of 10^8 K (for very massive clusters with $M \approx 10^{15} \, M_\odot$). No matter its extremely low density ($\approx 10^{-3}$ particles per cubic centimeter [18]), it is estimated that the mass in the intracluster gas is about five to ten times larger than the mass of stars in galaxies (where this ratio is bigger for more massive clusters) [32]. However, that is only a small fraction of the total cluster mass, since the majority of it consists of dark matter [39; 32].

Besides AGNs, clusters of galaxies are the brightest extragalactic sources of X-ray emission. This emission originates from the ICM. It is extended (as opposed to point-like emission from AGNs), optically thin[11] thermal[12] bremsstrahlung[13]. More precisely, electrons radiate while accelerating in the Coulomb field of protons and atomic nuclei in the hot collisionally ionized intracluster gas [32]. It is possible to use the morphology of X-ray emission from the ICM to distinguish between regular (relaxed) and irregular (non-relaxed) groups/clusters of galaxies. The former is characterized by smooth X-ray brightness distribution, the center of which coincides with the optical center of the group/cluster. On the other hand, the emission from irregular clusters often does not have one, but more, significantly bright substructures that correspond to different cluster galaxies or subgroups. [32].

1.3.3 Color magnitude diagram for groups/clusters

Color-magnitude diagrams (CMDs) display the relation between color (color index) and magnitude for a set of sky objects, in this case, galaxies. The color index is the difference in magnitudes observed through different bands. In the color-magnitude space, galaxies appear bimodally distributed [32]. One can distinguish between luminous, red galaxies and less luminous, blue galaxies. The former is often referred to as the red sequence, and the latter is called the blue cloud [32] (see figure 1.5 and note that stellar mass correlates to a galaxy's K_s-band luminosity, taking into account

---

[11]Once generated photon easily escapes the medium

[12]Thermal emission is produced by particles that are in the local thermodynamic equilibrium (LTR), i.e. they have Maxwellian velocity distribution.

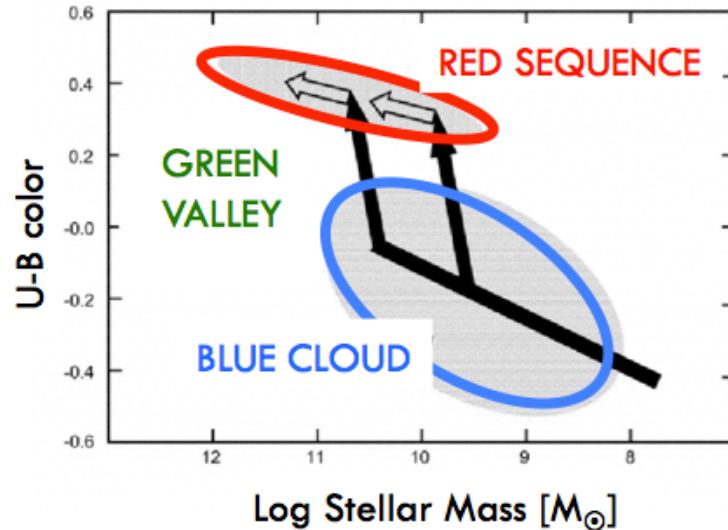[13]Emission from charged particles when accelerating

Figure 1.5: An image of different features that appear in galaxy color-magnitude diagrams. The red sequence is formed by older, usually elliptical galaxies that often reside in clusters while the blue cloud is formed by younger galaxies that still experience star formation. Green Valley is a transit area. The image was adopted from [6]

the galaxy's mass-to-light ratio [13]). As the names suggest, the red sequence is well defined meaning its scattering in color is small, compared to the scattering in the blue cloud. This is because the color of an old stellar population only slightly depends on its exact age, i.e. all early-type galaxies are similar in their (red) color [32]. A small slope in color-magnitude diagrams, i.e. somewhat redder colors for more luminous galaxies can be either due to somewhat higher ages of galaxies that are more luminous, or higher metallicities [32]. Higher metalicity makes the emission a little redder. On the other hand, blue galaxies own their color to the star formation in them. The larger scattering in color is most probably due to different levels of star formation in them [32]. The galaxies in between the red sequence and the blue cloud are called green valley galaxies [32]. It is observed and well established that elliptical (early-type) galaxies reside preferentially in more dense regions of the Universe, i.e. there is a large fraction of early-type galaxies in clusters [32]. Hence, the color-magnitude diagram of a cluster should have a very well-defined, nearly horizontal red sequence. The higher the redshift of a cluster the redder its red sequence is.

2 Goals of the thesis

Two radio galaxies, close to each other and with interestingly shaped, extended radio morphology were detected in the northern part of the COSMOS field at the redshift $z \approx 0.35$. Their jets are bent, i.e. they are probably wide-angle tail galaxies. According to the *COSMOS X-ray Group Catalog* [9], these two galaxies seem to be in the same group detected in the X-ray regime. This group may be a product of the merging of two smaller galaxy groups around individual radio galaxies. The merger scenario could explain the galaxies' bent jets. Additionally, we work with a third, point-like radio source, that is close to our two sources in the plane of the sky, at the same redshift as one of them, and also placed within the aforementioned galaxy group detected in X-ray. It could be the center of another smaller group of galaxies that may be gravitationally interacting (possibly merging) with the ones around the other two radio galaxies at $z \approx 0.35$.

Investigating this system to better understand the shape of radio galaxies and the formation and evolution process of the hosting galaxy group includes analyzing galaxies and their environment at different wavelengths. Here, we study the three radio sources and their environment in optical. We model the distribution of light from their optical counterparts by using the astronomical software Galfit. We extract optical sources within $10' \times 10'$ environment of the radio sources and analyze their spatial distribution via the Voronoi tessellation method. We single out optical sources from more dense regions (based on the results of the Voronoi tessellation) of the $10' \times 10'$ environment. Furthermore, using the latter sample of optical sources we create color-magnitude diagrams, and analyze the structure of features we find in them. We test if the position of the optical sources in the more dense regions of the $10' \times 10'$ environment depends on their color index.

3 Data

Since the primary goal of this work is an optical analysis of the three sources of interest and their environment, we mostly work with optical/NIR data. However, to better motivate our choice of sources and to better understand the final result it is inevitable to also use the data at other wavelengths (radio, X-ray). We have selected our sources and related data from the *Cosmic Evolution Survey* (COSMOS[14]) [33] field.

3.1 COSMOS

The *Cosmic Evolution Survey* (COSMOS) [33] is a project to survey a two square degree equatorial field centered on right ascension $\mathrm{RA} = 10^h\ 00^m\ 28.6^s$ and declination $\mathrm{DEC} = +02°\ 12'\ 21.0''$. This area was carefully chosen with the idea of minimizing the amount of interstellar medium and stars in our galaxy (the Milky Way galaxy) that would obscure our view of distant sources of interest. Data in the COSMOS field have been collected using most of the world's major telescopes, both on the Earth and in space at different wavelengths (from radio to X-rays). The main goal of the COSMOS project is to investigate different galaxies by means of both, their fundamental physical properties and how their close environment affects them [4].

The radio sources that we study here are from the COSMOS [33] field. They are presented in section 3.2, where the way how we choose them is also explained in detail. The data that we use for the analysis are taken from different observation projects in the field, focused at different wavelengths (from radio to X-ray) the details of which are given below in sections 3.1.1 - 3.1.4. We use radio data (details in section 3.1.3) to detect and describe our radio sources. We use optical data (details in section 3.1.1 and 3.1.2) to investigate the distribution of other galaxies in the surroundings of the radio sources, as well as for studying the distribution of light from the optical counterparts of the radio sources. We also use X-ray emission from the COSMOS field (details in section 3.1.4), i.e. we use the information about galaxy groups in our area of interest that were detected and whose properties were described based on the X-ray emission. We use this to better understand the environment of our radio galaxies.

---

[14]https://cosmos.astro.caltech.edu/page/astronomers

3.1.1 Optical/NIR data

To analyze the distribution of light from optical counterparts - host galaxies of the three radio sources, we use imaging data - maps (subimages from unrotated tiles [14]) observed with the *Wide Field Channel* (WFC) detector of the *Advanced Camera for Surveys* (ACS) mounted on the *Hubble Space Telescope*[15](HST). For presenting the optical counterparts together with their radio contours, we use the subimages from the mosaic [14] that was created by rotating the tiles and combining them (the mosaic is oriented with the North up). We choose the unrotated tiles rather than the mosaic for the analysis because it makes the Point-spread function (PSF) matching procedure more simple since the tiles are in the default unrotated frame of the ACS-WFC CCDs. The WFC is a mosaic detector that consists of two $(2048, 4096)$ pixel CCDs. It has $15 \times 15\ \mu\mathrm{m}$ pixels. The plate scale[16] is $(\mathrm{dx}, \mathrm{dy}) = (0.0500, 0.0500)\ \mathrm{arcsec/pixel}$. A field of view of the camera is $202'' \times 202''$. The ACS-WFC provides high throughput[17] and wide field imaging. A large portion of the COSMOS field ($1.6\ \mathrm{deg}^2$) was covered with the HST-ACS-WFC observations through f814w filter in two observing cycles from 2003 to 2005. This filter was chosen based on its exceptionally high transmission ($> 90\% - 95\%$) across an extremely wide wavelength range ($\approx 7300 - 9500$ Å). The observed data were processed, and the individual tiles, as well as the mosaic were created [14] and made avaliable through the IRSA[18] system. The individual raw exposures were first processed through charge transfer efficiency (CTE) correction[19] [21], and then they were run through an *IRAF/STSDAS* pipeline including dark current[20] subtraction, flat-fielding[21], bias[22] subtraction, low-level background removal (mostly due to scattered light) and other minor corrections. Moreover, ex-

---

[15]HST - *Hubble Space Telescope*: https://www.stsci.edu/hst

[16]The plate scale of a telescope is the relation between the angle across the celestial sphere and the corresponding distance across the image, i.e. it is the number of degrees (or arcminutes, arcseconds) corresponding to the number of centimeters (or milimeters, etc.) at the focal plane of a telescope where an image of an object is 'seen'

[17]The amount of data that flows through it

[18]$https://irsa.ipac.caltech.edu/data/COSMOS/index\_cutouts.html$

[19]Charge transfer efficiency is the ability of a CCD to easily move electrons without them being traped and then released afterwards causing a spurious signal. This efficiency decreases with time as cumulative radiation damage (continuous bombardment of high-energy particles above the Earth's atphmosfere) creates more charge traps.

[20]Dark current noise is the constant, device generated current that exists when no light is incident.

[21]Flat-field correction (FFC) is used to improve quality in digital imaging. It cancels the effects of image artifacts caused by variations in sensitivity between different pixels on the detector and by distortions in the optical path.

[22]A fixed-pattern noise (i.e. bias) in the image originating from the uniqueness of each specific sensor; even within the same model, no hardware part is ever exactly the same.

posures were cosmic-ray (CR) cleaned, astrometrically aligned, and the final mosaic was created [14]. The final plate scale of the unrotated tiles, as well as of the mosaic is $(\mathrm{dx}, \mathrm{dy}) = (0.0300, 0.0300)$ arcsec/pixel.

To investigate how other galaxies (optical sources) in the vicinity of the three radio sources are distributed in space and to produce color-magnitude diagrams for galaxy samples specially selected from that environment we use data from the recently published photometric catalog *COSMOS2020 CLASSIC* [40] (hereafter COSMOS CLASSIC). This catalog is one in a set of two new multiwavelength catalogs of distant universe *COSMOS2020* [40] (the other one is called *FARMER*). The COSMOS CLASSIC was created using traditional, aperture photometric methods on new imaging data that have been collected in the COSMOS field since the last public catalog in 2015[23]. It provides multiwavelength photometry data from different telescopes/cameras: Subaru[24]/HSC/Suprime-Cam, VISTA[25]/VIRCAM, CFHT[26]/MegaCam, HST/ACS, Spitzer[27]/IRAC, GALEX[28]. Moreover, it provides photometric redshifts and other physical parameters (absolute magnitude, stellar mass, and others) obtained through two independent codes *LePhare* and *EASY*. Here, we use photometric redshifts calculated using *LePhare* (later marked as lp_zPDF).

Except for the photometric redshifts from the COSMOS CLASSIC catalog [40], we also use less numerous, however, more reliable spectroscopic redshifts from the publicly unavailable catalog created by M. Salvato, 2017. (private communication). These data were mostly used for additional testing of already existing results obtained using photometric redshifts, as in general galaxies of interest have a calculated photometric redshift, however, not necessarily a spectroscopic measurement.

3.1.2 Masked areas

Some optical sources may not be visible, i.e. there is a lack of data about them in the COSMOS CLASSIC catalog [40] because they are covered or contaminated by a bright foreground star. Except this, the contamination can also be due to defects in

---

[23]*COSMOS2015* (Laigle et al. 2016)
[24]*Subaru telescope*: https://subarutelescope.org/en/
[25]VISTA - *Visible and Infrared Survey Telescope for Astronomy*: https://eso.org/public/teles-instr/paranal-observatory/surveytelescopes/vista/
[26]CFHT - *Canada France Hawaii telescope*: https://www.cfht.hawaii.edu/
[27]*Spitzer Space Telescope*: https://www.spitzer.caltech.edu/
[28]GALEX - *Galaxy Evolution Explorer*: http://www.galex.caltech.edu/

the camera. It is important to be aware of where these sources/defects are when performing analysis on a set of data affected by this problem. In this work, we use region files listing all such sources in the area in which objects are detected in the COSMOS CLASSIC catalog [40] (including the part of it that we are interested in analyzing). These files come together with the catalog release. There are 4 of them: HSC bright star masks, SuprimeCam masks (same as in the last catalog *COSMOS2015*), UtraVista region masks (areas that are not covered by the UltraVISTA[29] survey), and UltraDeep stripes (areas that are not inside the ultra-deep region of UltraVISTA survey). There are corresponding flags in the catalog with a value of 1 if an object is inside the masked region (i.e. bad) and 0 if it is outside (i.e. good). We filter our optical data by the value of FLAG_COMBINED which combines the first 3 of the 4 above presented masks. This flag is only 0 if the values of all three individual flags are 0.

3.1.3 Radio data

Radio data were used to select our AGNs (radio sources) and to study the morphology of their radio emission, the results of which are briefly presented here in section 3.2. We use the information on radio flux densities from two radio continuum maps at different frequencies (3 GHz, 1.4 GHz).

The 3 GHz (*VLA-COSMOS 3 GHz* continuum mosaic) and 1.4 GHz (*VLA-COSMOS Deep* 1.4 GHz mosaic) flux density data are taken from the *VLA-COSMOS 3 GHz Large Project* [35] and *VLA-COSMOS Deep Project*, respectively [31]. The former was constructed from 384 h of the *Very Large Array* (VLA) observations of the COSMOS field and is characterized by $0.75''$ resolution, and an average $2.3\,\mu\mathrm{Jy/beam}$ rms noise. The latter was created from the VLA observations of $50' \times 50'$ central region of the COSMOS field, reaching a resolution of $2.5''$, and an average rms noise of $\approx 12\,\mu\mathrm{Jy/beam}$. Hereafter, the radio continuum mosaics will be referred to as the 3 GHz and 1.4 GHz maps. Additionally, we use rms noise maps joined to the radio maps and obtained as a part of the related projects [35; 31], as well as the corresponding radio source catalogs. Exceptionally, at 3 GHz we use the *COSMOS VLA 3GHz Multiwavelength Counterpart Catalog* [36] (3 GHz catalog hereafter).

---

[29]https://ultravista.org/

3.1.4 X-ray data

We do not perform a detailed analysis of the X-ray emission from our area of interest - the surroundings of the three radio sources. However, we use the *COSMOS X-ray Group Catalog* [9]. This catalog contains 247 groups of galaxies in the COSMOS field that were detected by observing and analyzing the X-ray emission originating from the intra-cluster(group) medium (ICM) which was previously explained in section 1.3.2. The groups are listed in the catalog together with some of their important properties: sky coordinates (RA, DEC), spectroscopic redshift, radius r_{200}, and X-ray luminosity l_x. Here r_{200} is the radius where the density of the intra-cluster medium is larger than the critical density of the Universe[30] by a factor 200. The catalog also gives us the information about the total (baryonic and dark matter) mass m_{200} enclosed inside the r_{200} radius[31].

3.2 Choosing radio sources of interest and their radio properties

We work with 3 mutually close radio sources from the COSMOS field, namely: COS-MOSVLA3 J100026.49+024229.7 (hereafter 44, according to the ID from the catalog at 3 GHz), COSMOSVLA3 J100028.28+024103.3 (hereafter 10913), and COS-MOSVLA3 J100035.05+024154.6 (hereafter 4092). The details, i.e. the exact co-ordinates, spectroscopic redshifts, and photometric redshifts are shown in table 3.1. All three sources lie at the redshift $z \approx 0.35$. The first two are extended sources, i.e.

3 GHz ID	name	RA	DEC	3 GHz flux [μ Jy]	spec_z	phot_z CLASSIC
10913	COSMOSVLA3 J100028.28+024103.3	150.1179	2.6843	32090.0	0.34926	/
44	COSMOSVLA3 J100026.49+024229.7	150.1104	2.7083	2250.2	0.35062	0.3412
4092	COSMOSVLA3 J100035.05+024154.6	150.1461	2.6985	28.3	0.35062	0.3506

Table 3.1: Sources, their names from the 3 GHz catalog and properties from the COSMOS CLASSIC catalog [40], and internal catalog of spectroscopic redshifts in the COSMOS field. The radio galaxy 10913 does not have a valid photometric redshift since its light is contaminated by a bright star nearby.

their radio morphology is elongated. One of them, 10913 is of FRII type[32] and un-doubtedly a WAT galaxy, while the radio source 44 is of FRI type and possibly a WAT.

---

[30]The critical density is the average density of matter required for the Universe to just halt its expansion, but only after an infinite time. A Universe with the critical density is said to be flat. $\rho_c \approx 10^{-26} kg/m^3$

[31]With the assumption that the density within this radius equals to 200 ρ_c

[32]Extended radio sources can be divided based on the distribution of their flux into edge darkened (FRI) and edge-brightened (FRII) sources [7].
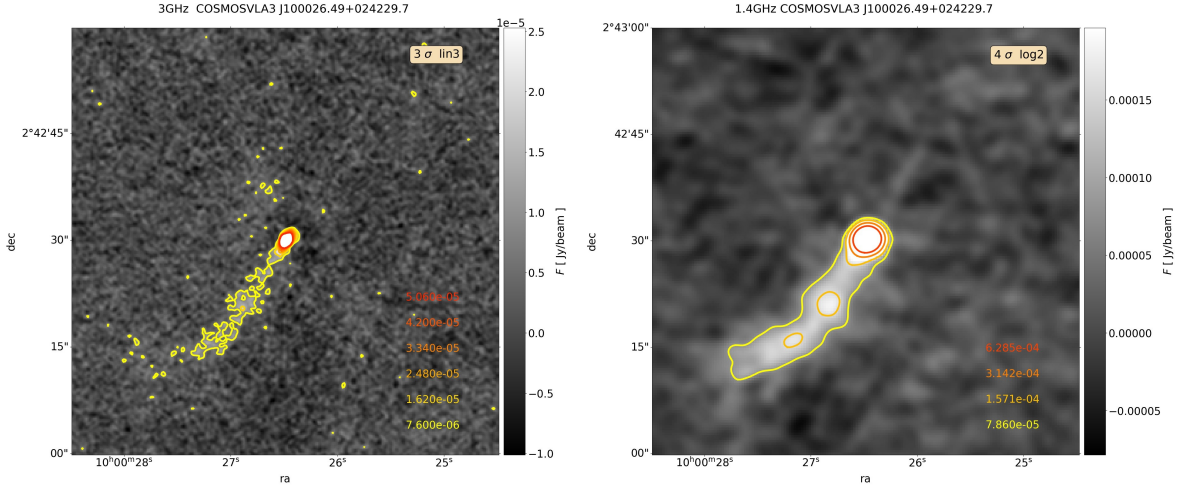
Figure 3.1: Radio contours for radio galaxy 44 at 2 different frequencies (left: 3 GHz, right: 1.4 GHz). The label in the upper right corner of each image shows details of the radio contour model. It indicates the flux density value at which contours start and the scale used. The scale is either logarithmic with base 2 (log2), which is the case at 3 GHz, or linear (lin N), where N is linear step value, which we used at 1.4 GHz to make contours look more clear. The image scale is from -4σ to 10σ, where σ is the median local rms noise. Different contours are plotted in different colors, and corresponding level values are given, in the same colors in the corner of each image.
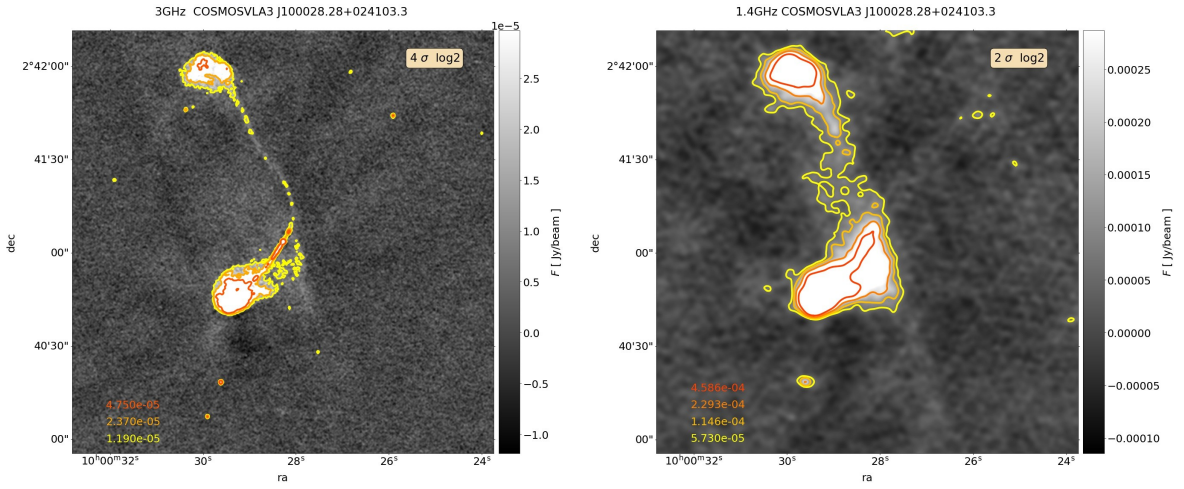

Figure 3.2: Contours for radio galaxy 10913 at 2 different frequencies. The labels in the upper right corners show the radio contour model details. At both frequencies, the logarithmic scale with base 2 makes the contours look the clearest. Image scale is from -4σ to 10σ, where σ is the median local rms noise.

However, only one of its jets is visible, which is most probably due to the relativistic beaming effect[33]. Radio galaxies 44 and 10913 are shown at 2 different frequencies (3 GHz, 1.4 GHz) with radio contours overlayed onto them in figures 3.1 and 3.2, respectively.

---

[33]The forward-going lobe of the radio galaxy, inclined at some angle relative to the line of sight, is observed to be brighter than the back-going lobe (that is sometimes not even visible)
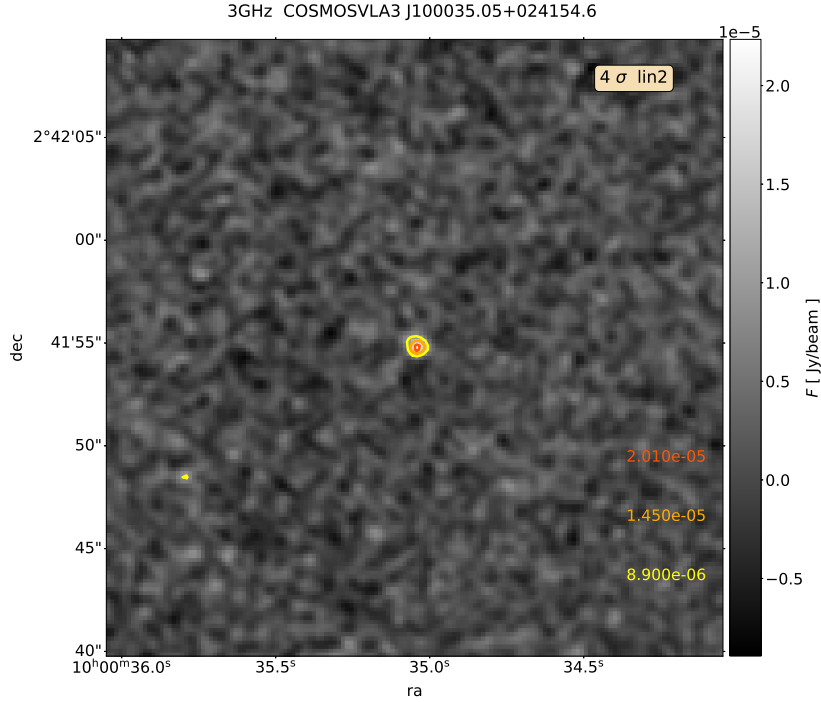
Figure 3.3: Contours for radio source 4092 at 3 GHz. The label in the upper right corner shows the radio contour model details. The linear scale with base 2 makes the contours look the clearest. Image scale is from -4σ to 10σ, where σ is the median local rms noise.

The sources were selected for the analysis due to a combination of two reasons. Firstly, both radio galaxies, 44 and 10913 seem to be in the same galaxy group, detected and listed in the *COSMOS X-ray Group Catalog* [9] (details in section 3.1.4). The second reason is their elongated and interestingly shaped morphology, suggesting that there might be more than one smaller group of galaxies (likely corresponding to individual radio galaxies) merging in their environment. This suggests that their common galaxy group may be a product of a (possibly still ongoing) group merger.

The third (point-like) radio source 4092 was first included in the analysis based on the results of the Voronoi tessellation - one of the methods that we use later in this work, to analyze the spatial distribution of optical sources in the environment of the three radio sources. This source is placed close to the remaining two (10913 and 44) in the plane of the sky. It is very close in redshift to radio galaxy 10913 and at the same redshift as radio galaxy 44. It is quite bright (see table 3.1) and multiple optical sources are present around it, suggesting this may be another galaxy group, involved in the above-mentioned merger. Since this is a point source and the morphology of its emission would appear roughly the same at both radio wavelengths (with some differences in the amount of flux), we only show it at 3 GHz in figure
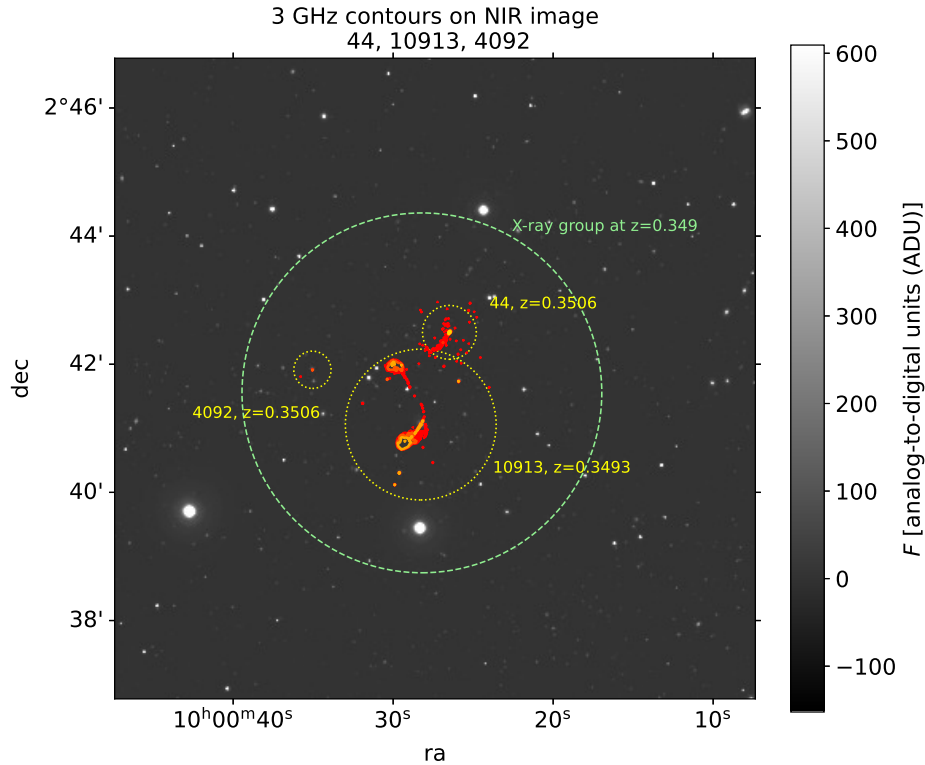
18

3 GHz contours on NIR image
44, 10913, 4092

Figure 3.4: All three sources (radio contours superimposed on the NIR image from UltraVISTA K_s band [22]) in the context of their environment. Individual radio sources are circled in yellow (to highlight them), and the light green circle represents a galaxy group in this area, detected in X-ray (*COSMOS X-ray Group Catalog* [9]). The group's radius r_{200} was adopted from the catalog and it is the radius where the intra-cluster medium density that emits X-rays is larger than the critical density of the Universe by a factor of 200.

3.3. All three radio sources are shown in figure 3.4. We overlay their 3 GHz radio contours (the same from figures 3.1 (left panel), 3.2 (left panel), and 3.3) on the UltraVISTA K_s band near-infrared (NIR) image [22] of a $10' \times 10'$ area centered at the average coordinates of radio galaxies 10913 and 44. Individual radio sources are circled in yellow and we additionally plot one light-green circle representing the galaxy group mentioned above. This group was presented among 247 galaxy groups in the *COSMOS X-ray Group Catalog* [9] (details in section 3.1.4), constructed from observations of diffuse X-ray emission (Chandra and XMM-Newton telescopes), and it is the only one whose center is located within this $10' \times 10'$ area, and whose redshift is close to that of the three radio sources. The central coordinates, the redshift and the radius of this galaxy group were adopted from the catalog: $\mathrm{RA} = 10^h\ 00^m\ 28.21^s$, $\mathrm{DEC} = +02°\ 41'\ 33.07''$, $z = 0.349$, $r_{200} = 2.8'$, $m_{200} = (9.1 \pm 0.3) \times 10^{13}\ M_\odot$. Radius r_{200} and the total mass m_{200} were previously explained in section 3.1.4. Based on

these data, we are dealing with a massive galaxy group, centered close to the most luminous of the radio galaxies - 10913 (see table 3.1), which probably also contains radio galaxy 44 and possibly radio source 4092. Most importantly, the group is hypothesized here to be a very dynamic system, possibly in the process of merging, what remains to be discovered by examining in detail the properties of individual radio sources as well as their surroundings.

4 Method

4.1 Fitting galaxies to models

The three radio sources have bright optical counterparts. Here, we fit the light distribution of each radio source, i.e. its optical counterpart observed through the f814w filter with the WFC detector of the ACS camera on the HST telescope, to the Sersic model (previously introduced in section 1.2.3). We work with three images (one for each source) that are extracted from the unrotated tiles, created from the HST-ACS-WFC observations in the COSMOS field [14]. More details about the data used are given in section 3.1.1. The fitting is done by using the astronomical software Galfit [26]. The optical counterparts are shown in figures 4.1, 4.2, and 4.3 for 10913, 44, and 4092, respectively. In these figures, 3 GHz radio contours (from figures 3.1 (left panel), 3.2 (left panel), and 3.3) are superimposed on the HST images at optical wavelenghts. In order to show the galaxies in optical together with their full radio morphology, these images are larger than the HST-ACS-WFC image (subimage from the unrotated tile) used for fitting the light distribution (which are shown later in section 5.1).
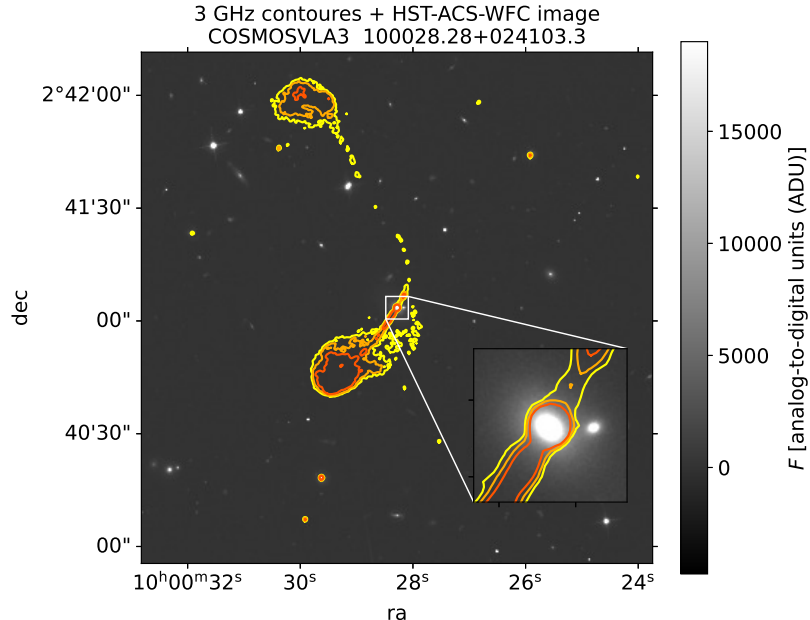

Figure 4.1: 3 GHz radio contours superimposed on the HST-ACS-WFC (f814w filter) image [14] of the optical counterpart of radio galaxy 10913. The figure contains a panel at the bottom right with a zoomed-in image of the galaxy's central part.
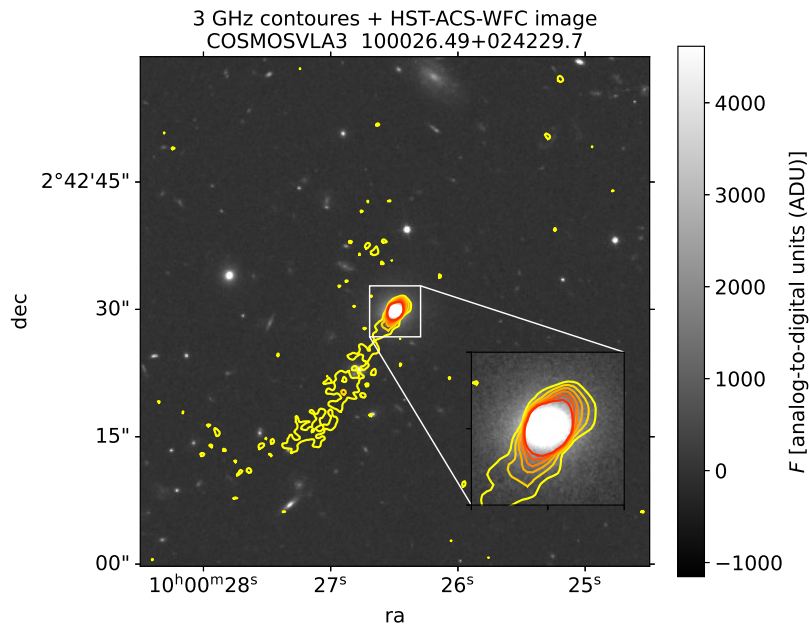
Figure 4.2: 3 GHz radio contours superimposed on the HST-ACS-WFC (f814w filter) image [14] of the optical counterpart of radio galaxy 44. The figure contains a panel at the bottom right with a zoomed-in image of the galaxy's central part.
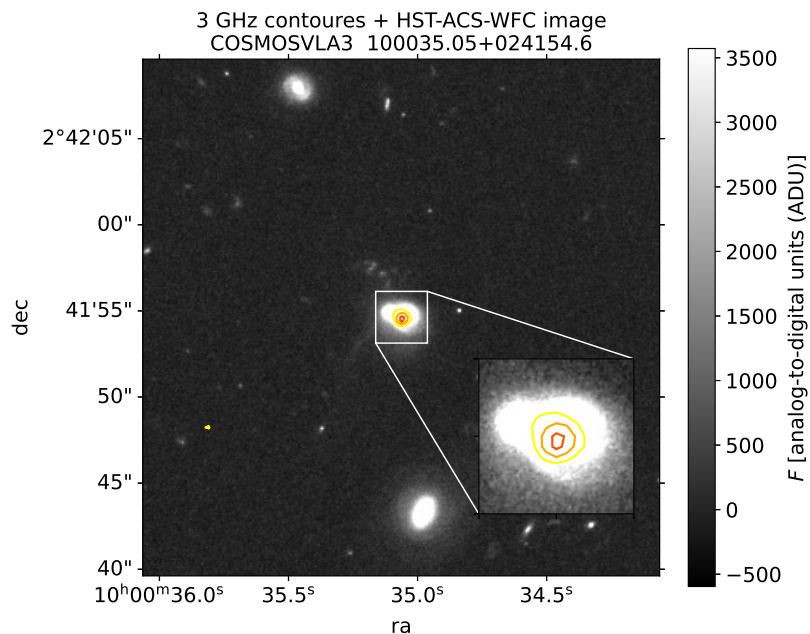

Figure 4.3: 3 GHz radio contours superimposed on the HST-ACS-WFC (f814w filter) image [14] of the optical counterpart of radio source 4092. The figure contains a panel at the bottom right with a zoomed-in image of the galaxy's central part.

4.1.1 Galfit software

Galfit [26] is an astronomical software that uses mathematical functions to describe light profiles of galaxies and their components. Galfit simply performs fitting and it does not extract a point spread function (PSF) from images, determine the initial

parameters of the fit, mask out neighbors, locate galaxies in images, calculate the best image size to fit or determine the sky level a-priori. However, this has to be performed prior to modeling, for it to be successful. Therefore, careful preparation of the input image and the initial parameters by the user is of crucial importance. To perform the fitting, Galfit needs: an image of a galaxy (galaxies) and the corresponding error (sigma) image, i.e. one standard deviation of counts at each pixel, an image of the point spread distribution function, a bad pixels mask (if any), and a file listing values of many different parameters (further described below). Everything above is required as an input directly from the user except for the error (sigma) image, which Galfit can create internally from the input image. Required parameters are divided into two groups: technical parameters and model parameters. Technical parameters include paths to all of the input and output files, the input image dimension (entire image or just a part of it) to fit, a PSF fine sampling factor (which equals to 1 if the PSF has the same sampling as the data), the size of a convolution box (for convolving the initial image with the PSF), a magnitude photometric zero-point, a plate scale[34]$(\mathrm{dx}, \mathrm{dy})$, and result displaying options. Here, we adopt the value of the magnitude photometric zero-point from the headers of the images. It is the same value for all three images: $21.1\ \mathrm{mag}$. For each image, we choose the size of the convolution box to be smaller than the image itself (roughly one-fourth of the image size in pixels), so that different sources in the image can be convolved with the PSF. This is especially important if using the aforementioned technique of fitting away extra sources in images. Finally, the plate scale for the HST-ACS-WFC drizzled[35] data is $(\mathrm{dx}, \mathrm{dy}) = (0.030, 0.030)\ \mathrm{arcsec/pixel}$.

Galfit performs the fitting by determining the values of free parameters in assumed models and it gives the information on the goodness of the fit (χ^2). That is why Galfit needs the second group of parameters - the model parameters. The user needs to define what model(s) of the spatial distribution of light to use for fitting and provide the initial guess for each of its(their) free parameters. It is possible to simultaneously fit the same part of the image (or two different parts) to different models. The initial guesses have to be correct enough for the fitting process to converge. A good approach to fitting is to start simple, with a single or two different models and

---

[34]Previously explained in a footnote in section 3.1.1

[35]Drizzle is a digital image processing method for the linear reconstruction of undersampled images.

then build up until all the light is fitted away from the initial image. The user can visually track the goodness of fit by inspecting the resulting cube that consists of 3 images: the initial image, the model(s) evaluated for the parameter values resulting from the fit, and the residual image. It is possible to decide for every single model used in fitting if the result is going to be subtracted from the initial image to produce the residual. Galfit supports a variety of different theoretical light distribution models: Sersic, Nuker, deVaucouleur, Exponential, Ferrer, and other profiles. It is also possible to fit the sky level while fitting the sources.

4.1.2 Preparing galaxy images

We extract the images of the galaxies from the HST-ACS-WFC unrotated tiles, observed in the f814 band (previously described in section 3.1.1). The tiles, as well as subimages extracted from them, are available through IRSA. For each galaxy, the corresponding subimage is centered at the galaxy's RA and DEC coordinates (see table 3.1), and its size is chosen to cover all the light that arises from the galaxy, as well as a portion of the sky. Where possible, we tried to avoid including sources other than the galaxy of interest in the image. However, we still ended having some neighboring sources in the images because truncating them to exclude the extra soruces would also exclude a significant portion of the galaxy's light. Finally, we multiply the images with the $EXPTIME$ value from the image header to obtain pixel values in analog-to-digital units (ADUs). This is done because Galfit requires pixel values to be in ADUs to be able to produce the corresponding sigma image internally.

4.1.3 Preparing the PSF image

For an accurate modeling of a light distribution of a galaxy, Galfit needs a point spread function image. This function describes the two-dimensional distribution of light in the telescope focal plane for an astronomical point source, spreading of which is a result of both, diffraction effects on the telescope's aperture and aberrations in the system. Galfit convolves the image (or each of its parts if the convolution krenel size is smaller than the image itself) with the PSF image before fitting. Here, we work with the HST data observed with the Wide field channel detector on the ACS camera. For HST observations, there is a special tool for creating PSFs called

TinyTim [15]. We modeled our PSF image with TinyTim in 3 steps: tiny1, tiny2 and tiny3. Running the first step - tiny1, the user is asked for the input information about the camera, the detector and the filter used as well as other techical details and expectations for the PSF size and the form of the point object's spectrum. Techincal details were adopted from the headers of the images and are the same for all three of them. All input parameters are listed in table 4.1. Tiny1 generates a parameter file based on the input information, and tiny2 creates a PSF using that parameter file. Finally, tiny3 is the third step which is only needed if working with ACS data because they are significantly distorted. It takes the PSF function created by tiny2 and integrates it onto distorted pixels on a distorted grid. The PSF created this way has the same orientation as the subimages extracted from the unrotated tiles (i.e. the both are in the default unrotated frame of the ACS-WFC CCDs) and it has a plate scale of $(\mathrm{dx}, \mathrm{dy}) = (0.050, 0.050)$ arcsec/pixel (default HSC-ACS camera plate scale), however the data we work with were processed [14] and have a pixel scale of $(\mathrm{dx}, \mathrm{dy}) = (0.030, 0.030)$ arcsec/pixel. Galfit can properly work either if the PSF and the data image have the same pixel scale, or if the PSF is more finely sampled than the data itself and the data-PSF plate scale ratio is an integer number. Here, we choose the latter option since it is the simplest possible solution. We first create a 5 times oversampled PSF with the TinyTim software by selecting $\mathrm{SUB} = 5$ option in the tiny3 function, which corresponds to a plate scale of $(\mathrm{dx}, \mathrm{dy}) = (0.010, 0.010)$ arcsec/pixel. This PSF is more finely sampled than the data and can be directly passed to Galfit. In this case, the PSF Fine-Sampling Factor in the galafit analysis has to be set to 3 (the data/PSF plate scale $\frac{0.030}{0.010} = 3$). This way we get the final PSF image that is used as an input for Galfit.

Parameter	Value
Camera	ACS - Wide Field Channel
Detector chip (1 or 2)	2
Position on the detector (pixels)	(2073,1035)
Filter	f814
Form of an object spectrum	M3V
PSF's diameter [arcsec]	3 (reccomended)
Secondary mirror despace [microns]	3 (typical value from figure 9. from [16])

Table 4.1: Parameters given to the TinyTim tool to create the PSF needed for Galfit analysis

4.1.4 Choosing models and their initial parameters

Since the galaxies host radio AGNs at a relatively low redshift ($z \approx 0.35$), we expect them to be bright and elliptic. The best accepted model to describe the light distribution of both dwarf and general elliptical galaxies is the Sersic profile (previously discussed in section 1.2.3). Hence, we try to fit the galaxies to a single Sersic model while keeping the sky background in images fixed at the a-priori estimated value. There are some additional sources in the images that can be dealt with in two ways. Either we can simultaneously fit them away while modeling the main source, or we can exclude them from the fit by providing a mask file (a list of bad pixels that cover them). Both ways are correct, and we make use of them depending on the case. We have to provide a set of initial guesses for the free parameters of the chosen Sersic model: Sersic index and the effective radius (enclosing the half of the total light from the galaxy being fitted). Here, our initial guess for the Sersic index is 4 since we are expecting the galaxies to be elliptical, and for each galaxy we estimate its effective radius by inspecting its image in DS9 [11]. Moreover, to fit a light distribution to the Sersic profile Galfit asks for initial guesses of the following parameters: position of a source to fit (x, y), its integrated magnitude, axis ratio (semi-minor/semi-major axis) and the position angle (0 if the semi-major axis is aligned parallel to the y-axis and increases toward the counter-clockwise direction). We obtain rough values of position, size and orientation parameters by visually inspecting the images in DS9, and the rough guess for an integrated magnitude is calculated as [26]:

$$m_{tot} = -2.5 \times log_{10}\Big(\frac{F_{tot}}{\text{EXPTIME}}\Big) + \text{mag\_zpt} \tag{4.1}$$

Here, F_{tot} is the total integrated flux from the source being fitted (which we estimate by inspecting the source image in DS9), while EXPTIME and mag_zpt are the total exposure time and the magnitude zeropoint from the corresponding image header.

4.1.5 Dealing with the sky background

It is important to take care of the sky background present in images in order for Galfit to fit the light distributions of the galaxies correctly. Here, we estimate the background level in our images a-priori and fix the sky parameter to that value while performing the fit. The subimages from the HST-ACS-WFC tiles [14] were purposely

chosen to be large enough so that there is enough sky background, i.e. that they are not dominated by the primary source of interest. We visually inspect the images in DS9 [11] and in each of them we find a boxy region that contains no sources. For each image, the background is then estimated as the median value (in ADUs) of pixels within the chosen box. The resulting background values are presented amongst the other results and backround box regions used for calculation are shown in the final images in section 5.1.

4.2 Analyzing the spatial distribution of optical sources in the environment of the radio sources via Voronoi tessellation method

Bright optical galaxies hosting radio sources usually lie in the centers of galaxy groups or clusters as explained in section 1.3.1. The properties of radio sources can largely depend on the characteristics of their environment. Therefore it is important to observe a radio source and its hosting galaxy in the context of the adjacent group or cluster. In order to learn more about the environment of our radio sources of interest and how it affects them, we single out the optical sources from their environment, and we analyze their spatial arrangement. Optical sources taken from the COSMOS CLASSIC catalog [40], which hereafter we refer to, are mostly classified as galaxies. However, we also include objects that are classified in the catalog as X-ray sources (as it is the optical counterpart of the radio galaxy 44). We also try to only include sources classified as galaxies, however the results remain unchanged. With special attention, we examine if and where there is one or possibly more spatial overdensities. To do so, we use a method called Voronoi tessellation.

4.2.1 Voronoi tessellation

Voronoi tessellation (in literature also found as Voronoi decomposition or Voronoi diagrams) is a method of space segmentation that is widely used in various fields of science and technology [45]. This method divides a plane into smaller regions (polygons) called Voronoi cells. Each cell corresponds to only one of the finitely many points in the plane called Voronoi seeds, i.e. there are as many seeds as Voronoi cells. A single cell consists of all points in the plane closer to its seed than to any other seed in the plane. This is illustrated in figure 4.4. Directly from the rules for
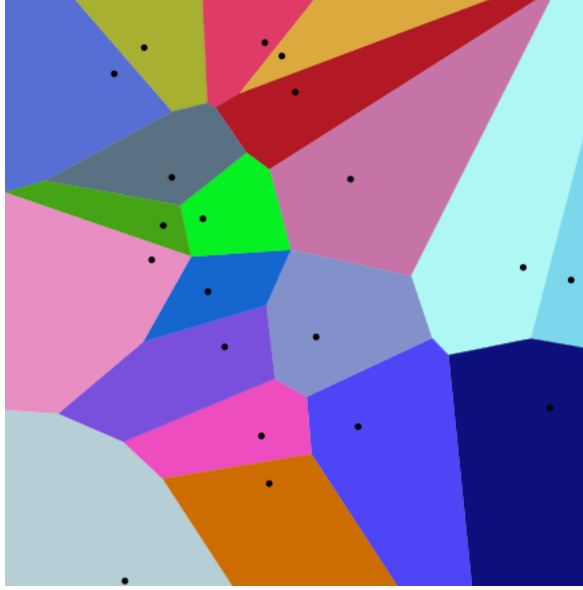
Figure 4.4: An example of a Voronoi diagram. The image was adopted from: https : //en.wikipedia.org/wiki/Voronoi_diagram#Illustration

the construction of a Voronoi diagram it follows that cell areas are going to be larger in parts of the plane where there are fewer seeds. Thus, a cell area can be used to estimate the local spatial density of seeds. Furthermore, since there is only one seed per cell, one can define the local density of seeds as the inverse of the cell area:

$$\rho_i = \frac{1}{A_i} \tag{4.2}$$

Here, ρ_i is a local density of seeds in the vicinity of the i-th seed, and A_i is the area of the i-th cell that corresponds to the i-th seed. Using this approach one can not just detect, but also quantitatively describe and compare local densities in different parts of the plane. We can use the Voronoi tessellation method to identify regions in the environment that are overdense or underdense with respect to the custom density threshold that we previously defined. Here, we apply this method in 2 dimensions (in the plane of the sky) by using the Voronoi module from scipy.spatial subpackage in Python. Using this method is not necessarily more correct if performing it on a 3-dimensional set of galaxies [45]. This is due to the lack of preciseness in redshift data (which represents the third dimension) compared to high preciseness of data in the plane of the sky, i.e. RA and DEC coordinates [45]. This problem is especially pronounced here since we work with more numerous, but less accurate photometric redshifts instead of spectroscopic ones.

4.2.2 Preparing the initial data set

To study the environment we first have to determine what the environment of our radio sources is. A few questions arise. How big in the plane of the sky and how wide along the line of sight should be our initial set that we call environment? Where should be the center of the set? One fair choice is to simply experiment with different sizes and different centers of the initial set of galaxies. However, in doing so, we can use a couple of guidelines derived from observational facts.

Sizes of groups and clusters of galaxies are of the order of a few $h^{-1}\,\mathrm{Mpc}$ up to $10\,h^{-1}\,\mathrm{Mpc}$, where h is the dimensionless equivalent of the Hubble constant (defined as $H_0 = 100\,h\,\mathrm{km\,s^{-1}\,Mpc}$). The h is often added to the measured properties of individual galaxies, i.e. groups/clusters of galaxies. Since the value of the Hubble constant is still uncertain, the value of this parameter can vary (from 0.67 to 0.74). Thus, we can conclude that the sizes of groups and clusters reach values of a few Mpc. Our system of radio sources and the adjacent group lies at $z \approx 0.35$, which corresponds to a distance (real, comoving radial distance) of $\approx 1380\,\mathrm{Mpc}$. This was calculated using the *Ned Wright's cosmology calculator*[36], with the following parameters: $H_0 = 70\,\mathrm{km\,s^{-1}\,Mpc^{-1}}$, $\Omega_M = 0.286$, $\Omega_\lambda = 0.714$. Using these two facts we can approximate the angular size of our environment in the range from $\approx 2.49'$ for a group with a diameter of $1\,\mathrm{Mpc}$ to $\approx 12.46'$ for a cluster with a diameter of $5\,\mathrm{Mpc}$.

Taking into account the above facts we choose the environment to be a truncated pyramid (see figure 4.5) with dimensions as follows. The cross-section of a pyramid is a box, $10' \times 10'$ in the plane of the sky and centered on the average RA and DEC coordinates of the system of radio galaxies 10913 and 44: right ascension $\mathrm{RA} = 10^h\ 00^m\ 27.3^s$ and declination $\mathrm{DEC} = +02°\ 41'\ 46.56''$. It would be correct to take the central coordinates of the above-mentioned X-ray detected group (see section 3.2) to be the spatial center for the sample of optical sources. However, the spatial difference between the X-ray center and the average coordinates of the system of radio galaxies 10913 and 44 is small compared to the $10' \times 10'$ dimensions of the sample. Therefore, the result would remain unchanged.

In the third dimension (along the line of sight) we set the central redshift value to be an average of spectroscopic redshift values for 10913, 44 and 4092, i.e. $\bar{z} = 0.3502$. The central redshift would be the same if we just averaged values for the
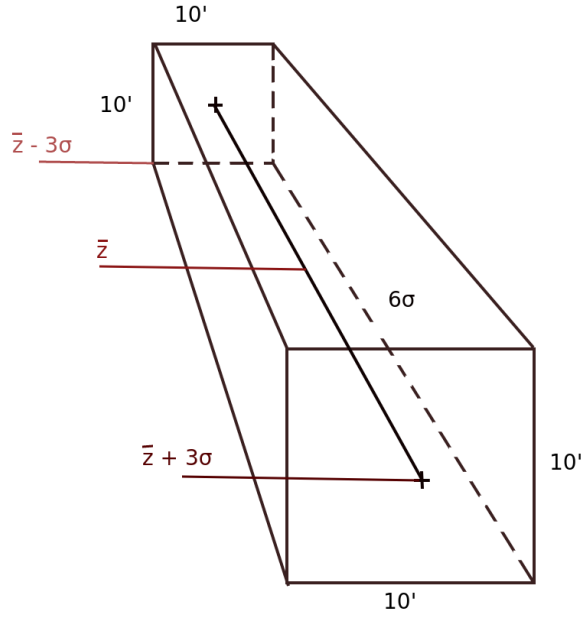
---

[36]http://www.astro.ucla.edu/ wright/CosmoCalc.html

Figure 4.5: A visual representation of the environment, i.e. its dimensions. It is $10' \times 10'$ in the plane of the sky and $6\,\sigma$ wide in the third dimension. Here, σ is a normalized medium absolute deviation (NMAD), that is, a measure of the deviation of photometric redshifts from the corresponding spectrometric redshifts and it has different values depending on which sample ($i < 24$ or $i < 25$) we work with.

sources 44 and 10913 since 4092 has the very same spectroscopic redshift as 44. Wideness of the box, i.e. its size in the third dimension is determined as $z \in [\bar{z} - 3\sigma,\ \bar{z} + 3\sigma]$. Here, σ quantifies the precision of the $\mathrm{phot\_z}$ data from the COS-MOS CLASSIC photometric redshift catalog [40] (see section 3.1.1 for details) and it is called normalized median absolute deviation (NMAD). NMAD value is derived directly from photometric redshift data through comparison with the more accurate spectroscopic redshifts and is defined by [40]:

$$\sigma = 1.48 \times \mathrm{median}\left(\frac{\Delta z - \mathrm{median}(\Delta z)}{1 + z_{\mathrm{spec}}}\right) \tag{4.3}$$

In the expression (4.3) Δz is the difference between photometric and spectroscopic redshift value for the same source ($z_{\mathrm{phot}} - z_{\mathrm{spec}}$). NMAD has different values if calculated using data from different apparent magnitude bins. The dimmer the sources that one lets through are, the more uncertain their photometric redshifts and consequently the bigger the deviations from the spectroscopic values will be and vice versa. We do not perform the comparison or calculate the NMAD values by our-

bin (from the paper)	σ (from the paper)	σ	
		$17 < i < 24$	$17 < i < 25$
$17 < i < 22.5$	0.008	0.015	0.024
$22.5 < i < 24$	0.015		
$24 < i < 25$	0.024		

Table 4.2: Values of σ calculated for magnitude bins from the paper describing COS-MOS CLASSIC catalog [40] and σ values adopted for our bins as described in the text above.

selves, however we adopt them from the original article that describes the COSMOS CLASSIC catalog [40] and where σ was already calculated for different magnitude bins using the above expression (equation 4.3) on a set of spectroscopic redshifts that is an upgraded version of the set we have access to. According to the paper, from comparison of COSMOS CLASSIC LePhare photometric data with spectroscopic data: $\sigma = 0.008$ (for $17 < i < 22.5$), $\sigma = 0.015$ (for $22.5 < i < 24$), and $\sigma = 0.024$ (for $24 < i < 25$), where i is apparent magnitude in i band (Subaru, HSC camera) and its minimal value in the COSMOS CLASSIC catalog [40] is ≈ 17. Here, we work with galaxies in two magnitude bins: $17 < i < 24$ and $17 < i < 25$. Our bins are unions of the first two ($i < 24$) and all three ($i < 25$) of the above sets (from the paper [40]). Calculating the σ value for a union of two or more bins from σ values for individual bins might not be trivial since the numbers of sources in them are not of the same sizes and σ depends on the value of variable i. Therefore, for each of the two unions ($i < 24$, $i < 25$) we choose its σ to be the maximal NMAD value (from all values corresponding to different sub-bins that are given in the paper). Thus, $\sigma = 0.015$ (for $17 < i < 24$) and $\sigma = 0.02$ (for $17 < i < 25$). The scheme described is visible more easily from table 4.2. Note that by determining σ values this way rather than, for example averaging σ values for different smaller bins forming the larger one, we include more data.

The wideness (height) of the truncated pyramid as defined above should be enough to cover the entire potential group, i.e. all potentially interesting structures in the third dimension. The wideness value of 6σ for $\sigma = 0.015$ equals to $\approx 325\,\mathrm{Mpc}$, calculated once again using the *Ned Wright's cosmology calculator* with the cosmological parameters: $H_0 = 70\,\mathrm{km\,s^{-1}\,Mpc^{-1}}$, $\Omega_M = 0.286$, $\Omega_\lambda = 0.714$. This value is larger than the usual group or cluster diameters, which range from a few Mpc up to $\approx 7\,\mathrm{Mpc}$ (this was disscused previously in this section). Therefore, we can calculate

the ratio of the wideness (height) of the truncated pyramid and the average diameter of groups and clusters ($R \approx 325\,\mathrm{Mpc}/7\,\mathrm{Mpc} \gtrsim 50$). We assume that the structure of interest is not more than R times larger along the line of sight than in the plane of the sky, which is very unlikely. Such a wide range in the third dimension is necessary to extract all the galaxies from the catalog with a redshift close to ≈ 0.35, taking into account the $\mathrm{phot\_z}$ error (σ).

We create another 3 sets, i.e. potential environments. The 2 of these sets only differ from the first one in the central redshift value $\overline{z}$ (and are now equal to redshift values of 44 (or 4092 since it is the same value) and 10913). The third set has the same central redshift as the first one, however is wider in the third dimension ($4\,\sigma$ instead of $3\,\sigma$). This way we prepare 4 different initial sets of galaxies (that we can call probable environments that should be large enough to contain the structures (the group and its possible substructures) that we are interested in observing. All 4 samples only contain so-called good objects ($\mathrm{FLAG\_COMBINED} = 0$, see section 3.1.2 for details) that are not inside masked areas.

Hereafter, we refer to the first sample described here as the $10' \times 10'$ environment and we present and discuss in detail the results of the analysis performed on this sample. The results of the same analysis performed on the 3 additional samples described above are consistent with what we obtain working with the $10' \times 10'$ environment sample.

4.2.3 Source density treshold

As described in section 4.2.1, by performing Voronoi tessellation we divide the $10' \times 10'$ environment into smaller regions around each optical source and assign them an associated local density ρ. Our goal is to analyze the spatial distribution of optical sources in the vicinity of our system of radio sources and possibly while doing so detect some overdense regions. Therefore, we must define what overdense means and quantify it. We need to determine a density threshold ρ_{cr}. All Voronoi cells with a local density smaller than this will be considered as underdense while all cells with a value above it will be considered as overdense regions.

To do so we introduce another set of optical sources - namely the background. This set should ideally be centered at the same coordinates. However, it should be larger than the $10' \times 10'$ environment of interest. Here its dimensions are $1° \times 0.62°$,

which is expected to be large enough. However, the set is not centered at the same coordinates as the $10' \times 10'$ environment. This is because our system of radio sources is only $\approx 7.2'$ away from the northern boundary of the COSMOS field, however a symmetric box centered at our radio system and 2 x $7.2'$ wide and high is not large enough to be a background. Therefore, we spatially extend the set by moving its boundaries, where that is possible until its aforementioned size ($1°$ x $0.62°$) is reached (this is visible more easily from figure 5.5 in the section Results). Furthermore, the background spans the same range of redshifts as the $10' \times 10'$ environment. This set of sources contains a larger number of weak, medium, and very dense areas which is exactly a property of the background.

Voronoi tessellation is, except on the $10' \times 10'$ environment of interest, also performed on its corresponding background. From the results of the latter, we calculate the mean background density $\overline{\rho_{bckg}}$ by summing the local densities of all cells and dividing the sum by the number of them. In the same way, we calculate the mean $10' \times 10'$ environment density $\overline{\rho_{env}}$ from local densities assigned to Voronoi cells resulting from the segmentation of the that area. Having this, we can move from expressing local densities assigned to single cells in both, the background and the $10' \times 10'$ environment samples in $1/\deg^2$ and instead express them in the units of the corresponding mean densities ($\overline{\rho_{bckg}}$ and $\overline{\rho_{env}}$). We then separate overdense regions (cells) from the remaining cells. For that purpose, we compare cumulative distribution functions of local densities for both samples.

The cumulative distribution function F_X of a real-valued random variable X, evaluated at x, is the probability that X will take a value less than or equal to x:

$$F_X(x) = P(X \leq x) \tag{4.4}$$

In our case, random variable X is a local density expressed in units of the mean sample density, i.e. $X = \rho/\overline{\rho_{env}}$ for the $10' \times 10'$ environment and $X = \rho/\overline{\rho_{bckg}}$ for the background sample. For each of these two samples, we create $F(X)$ starting from the corresponding list of local densities in the following way. We first sort them in ascending order and then make a histogram using Numpy.histogram. We set both, the number of histogram bins for the $10' \times 10'$ environment sample and for the background sample to the same value of 110 when working with the $i < 24$

sources, and 280 when working with the $i < 25$ sources. We further calculate the cumulative sum of histogram values by using the cumsum module from Numpy and finally multiply it by the size of a single bin to get $F(X)$. Functions are then plotted in the same diagram so that we can compare them.

From this comparison, we expect to be able to spot where the two cumulative distribution functions start to differ and that way set the density threshold that will best distinguish between the background and potential gravitationally bound structures in the $10' \times 10'$ environment. The latter would appear overdense with respect to the background density if a group or a cluster is present. However, it is important to notice that there is arbitrariness when graphically determining where and to what extent the functions coincide and at what point exactly they begin to differ. For this reason, we should not understand the threshold determined this way as the exact boundary of the background and potential structures, but more as a good guideline to where it might be.

4.2.4   Treating masked areas

Masked areas were previously discussed in section 3.1.2. and were again mentioned in section 4.2.2 in the context of filtering the data set (we only work with optical sources that are not in contaminated areas, i.e. for which $\mathrm{FLAG\_COMBINED} = 0$). The question arises how these holes in data affect the analysis and how we treat them. If we do not exclude masked areas when performing the analysis, then the average background and $10' \times 10'$ environment densities turn out to be somewhat lower. This is because the holes, in the context of the Voronoi tessellation, are extremely underdense regions. One of these two samples (densities) might be affected by this more than the other, depending on the spatial distribution of masked regions. Following this, not treating the masked regions can slightly affect the threshold ρ_{cr}. However, there was already some arbitrariness in determining the threshold value (which was previously discussed in section 4.2.3). Therefore, for the sake of simplicity, we decide not to treat them here in any special way. Due to its construction, the Voronoi tesselation method will assign larger cells to such regions and most probably none of them will pass the density threshold. Instead of leaving them out of the analysis, we rather overlay masked regions on the resulting Voronoi images (in section 5.2) using the data from 3 region files: HSC bright star masks, SuprimeCam masks,

and UltraVISTA region mask (all described in section 3.1.2).

4.3 Color-magnitude diagrams

After examining the spatial distribution of sources in the plane of the sky, we investigate the relation between the luminosities (magnitudes) and color indexes of galaxies in the $10' \times 10'$ environment of our system of radio sources. This is done by plotting color-magnitude diagrams (CMDs). As previously explained in section 1.3.3, such a diagram usually consists of three different shapes/areas namely: red sequence, blue cloud, and green valley. Detecting a well-defined red sequence in the CMD of our $10' \times 10'$ environment sample would strongly suggest that we are dealing with a galaxy group. By careful examination of the shape of the sequence and potentially detecting some substructures, it may be possible to find out more about how the environment galaxies are distributed in the third dimension, i.e. if there is one large or more groups of galaxies at slightly different redshifts. Hence, plotting CMDs opens another window on the matter of spatial distribution of optical sources in the environment. Moreover, by studying how the spatial distribution of galaxies within a group or a cluster depends on their color it is possible to find out more about its dynamical state. In relaxed groups or clusters red galaxies are found concentrated around the center, while blue galaxies are placed in outer parts.

4.3.1 Preparation of the data set

The sample we use for plotting is not exactly the $10' \times 10'$ environment defined in section 4.2.2, but rather the galaxies from that set that, according to the results of the Voronoi tesselation belong to overdense regions ($\rho > \rho_{cr}$). By choosing these we minimize the scattering in the CMD that mostly arises from sources that were included in the sample either because of projection effects, or measurment error.

4.3.2 Choice of photometry

To plot a CMD one needs a sample of galaxies together with their photometric data, i.e. magnitudes observed through at least 2 different bands. The question is which bands should be chosen for this purpose. One of the main differences between blue and red galaxies is in their spectra: the flux of red galaxies starts significantly falling

below 4000 Å (in the rest-frame of galaxies), while blue galaxies have a lot of flux at these wavelengths. Therefore, when calculating a color index it is best to choose two filters that are somewhat above and below 4000 Å in the galaxy's rest-frame. Our sources are at $z \approx 0.35$. By taking into account the definition of a redshift ($z = (\lambda_{\text{observed}} - \lambda_{\text{emitted}})/\lambda_{\text{emitted}}$), this means that the actually observed wavelength of the rest-frame 4000 Å break is at ≈ 5400 Å. Therefore, to construct the color index for our CMD, we decide to use Subaru/HSC g and r bands. The former is centered at 4847 Å and it is 1383 Å wide, while the latter is centered at 6219 Å and its width is 1547 Å. For the magnitude dimension in the CMD, we use a third Subaru/HSC band, namely the i band centered at 7699 Å and 1471 Å wide.

5 Results and discusion

5.1 Results of fitting galaxies to Sersic models

Here, we present the results of fitting the light profiles of the three galaxies (counterparts of the radio sources) to the Sersic model, using the Galfit software. This analysis was previously motivated and described in section 4.1. Galfit finds the Sersic index and effective radius values for each of the three galaxies, as well as other parameters such as the exact center of the galaxies, their total magnitudes, axis ratios, and position angles. All three galaxies have their Sersic index value close to or somewhat larger than $n = 4$. Modeling the galaxies, we managed to fit away most of their light. However, there are some residuals left, especially in the case of the optical counterpart of the radio source 4092. Some parts of the analysis can and should be done in a more advanced way (see below for the details), which is beyond the scope of this work.

5.1.1 Radio galaxy 10913

We expect the optical counterpart of the radio galaxy 10913 to be a bright elliptical, and the results of fitting to the Sersic profile agree with this expectation. The fitting results (the initial, model, and residual image) are visually presented in figure 5.1 and the values of different parameters resulting from the fit are listed in table 5.1. Galfit finds the Sersic index value to be $n = 3.946 \pm 0.005$ and the effective radius in pixels $R_e = 90.8 \pm 0.2 \,\mathrm{pixels}$. The sky background was fixed to the estimated value of $6.86716 \,\mathrm{ADU}$, as we determined apriori by calculating the median pixel value in the background box (marked in orange color in the bottom right corner of the initial and residual images in figure 5.1). Except for the galaxy, the image also contains another less bright source close to the galaxy in the plane of the sky. This additional source is not listed in the *ACS I-band Photometry Catalog* [17] of optical sources, most probably due to the combination of its low brightness and proximity to the optical counterpart of radio galaxy 10913. It is important to remove the light originating from this source when fitting the galaxy's light distribution. We did this by simultaneously fitting it away with Galfit while modeling our galaxy. Due to its ability to cover a wide range of light distributions, we once again assumed the Sersic model to fit this additional
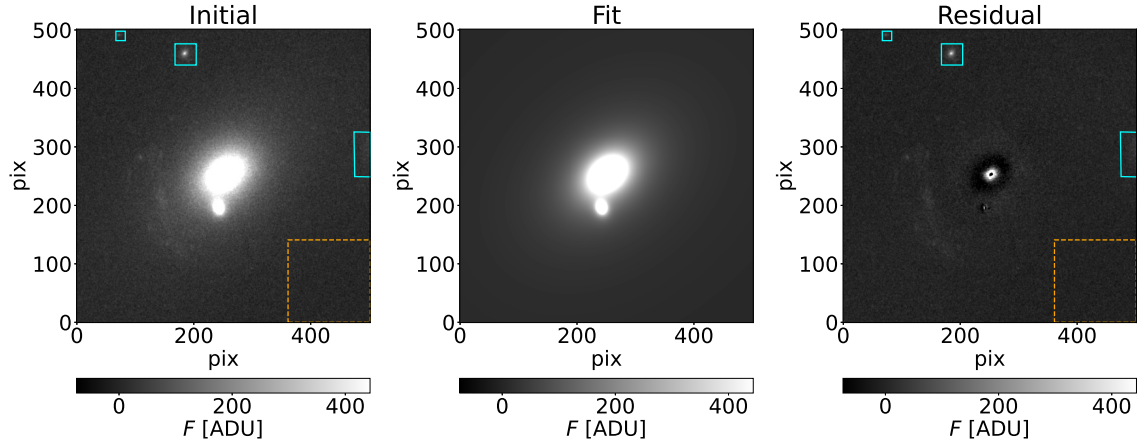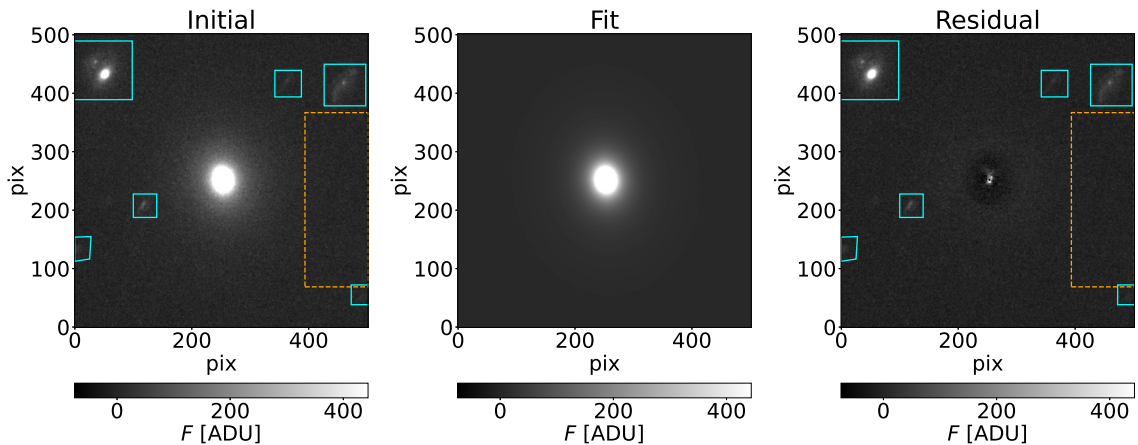
Figure 5.1: From left to right: the initial subimage from the unrotated tile containing the optical counterpart of radio galaxy 10913 (in the center) and additional sources, the model image, and the residual image created by subtracting the model from the initial image. The orange box, at the bottom right, defines the area used for estimating the sky level. Light blue polygons are masks, i.e. the pixels that were excluded from the analysis. The image scale was chosen to make the features in images visible more easily.

Parameter	Value for the galaxy	Value for the additional source
Position [pixels]	$(253.233 \pm 0.005, 253.547 \pm 0.004)$	$(243.361 \pm 0.007, 196.657 \pm 0.008)$
Integrated magnitude [mag]	12.326 ± 0.001	15.936 ± 0.002
Effective radius R_e [pixels]	90.8 ± 0.2	6.95 ± 0.03
Sersic index	3.946 ± 0.005	1.833 ± 0.009
Axis ratio	0.7195 ± 0.0005	0.770 ± 0.002
Position angle [deg]	-50.43 ± 0.07	13.0 ± 0.4

Table 5.1: Parameters obtained through fitting the image, i.e. the light distribution of the optical counterpart of radio galaxy 10913 and the light from the additional source.

source (the resulting parameters are listed in table 5.1). There are some other, dim sources in the image. These may be challenging to fit due to their low brightness so we rather mask them away. Regions of the image that were masked, i.e. not included in the Galfit analysis are marked with light blue polygons in the initial and the residual image in figure 5.1. The goodnes of this fit, i.e. the reduced χ^2 value is 0.59. By inspecting the residual panel we see that most of the galaxy's light, as well as the light of the close additional source is successfully fitted away. However, where there used to be the galaxy, one can spot a circularly-shaped residual with the dark center. The dark center of the residual pattern aligns with the galaxy's center (see the central coordinates in pixels in table 5.1). It can happen that the centers of some galaxies deviate from the models which are a good fit for the rest of the light distribution. This commonly happens due to core effects at low radii

38

[10]. This kind of over-subtracted residuals in the center sets an upper limit on the Sersic index. A larger n would cause even greater over-subtraction at the center. Therefore, this residual hints that the central profile is not steeper than ≈ 4, which we obtain by modeling its light distribution this way. Moreover, it means that the model is too bright in its central part. This may be due to more than one reason and requires additional analysis that goes beyond the scope of this work. However, a possible reason could be that a single Sersic model is too simple for analyzing this galaxy. Similar residuals were successfully removed in the previous research [26] by assuming more complex (two-component) models.

5.1.2 Radio galaxy 44

As described above, we model the light distribution of the optical counterpart of radio galaxy 44 assuming the Sersic model. The results are shown in figure 5.2, and the parameters we obtain through fitting are listed in table 5.2. Here, the
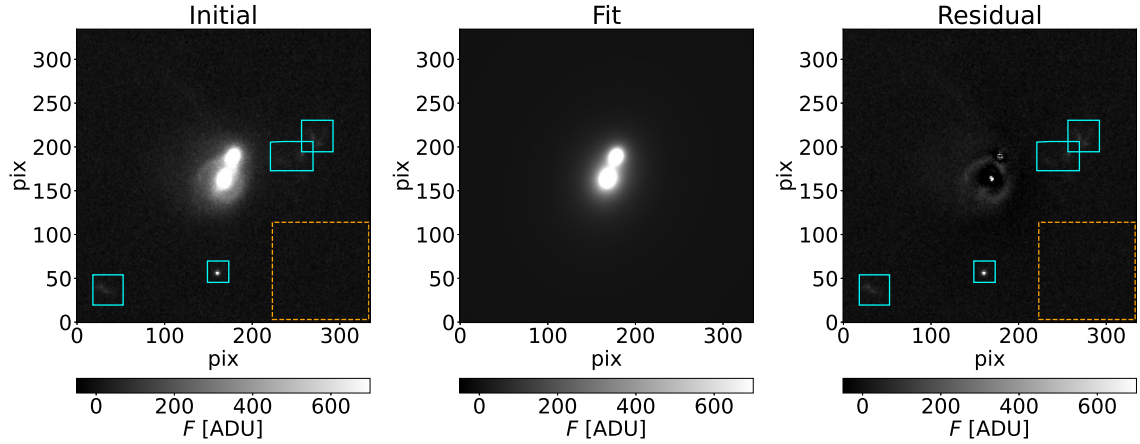

Figure 5.2: From left to right: the initial subimage from the unrotated tile containing the optical counterpart of radio galaxy 44 (in the center) and additional sources, the model image, and the residual image. The orange box, in the middle right, defines the area used for estimating the sky level. Light blue polygons represent masked areas. The image scale was chosen to make the features in images visible more easily.

fixed value of the estimated background is 5.67837 ADU, and the background box is once again shown in the initial and residual images in orange. Other sources in the image, some of them quite bright, were masked to better fit the galaxy and these regions are represented by light blue polygons in figure 5.2. The goodnes of this fit, i.e. the reduced χ^2 value is 0.82. The galaxy's light is well fitted away except for

Parameter	Value for the galaxy
Position [pixels]	$(253.980 \pm 0.005, 252.460 \pm 0.005)$
Integrated magnitude [mag]	13.346 ± 0.002
Effective radius R_e [pixels]	44.8 ± 0.2
Sersic index	4.77 ± 0.01
Axis ratio	0.8124 ± 0.0009
Position angle [deg]	7.7 ± 0.2

Table 5.2: Parameters obtained through fitting the image, i.e. the light distribution of the optical counterpart of radio galaxy 44.

the circularly-shaped residual with the dark center. The reasons and the meaning of this are the same as described in the previous section (the case of the radio galaxy 10913). However, the result here seeking for additional explanation is the Sersic index value which turns out to be greater than 4. In fact, Galfit finds the Sersic index value to be $n = 4.77 \pm 0.01$ and the effective radius in pixels $R_e = 44.8 \pm 0.2$ pixels. Elliptical galaxies are known to have their Sersic index values of about 4. The value we obtain here may be somewhat higher than 4 due to the sky background possibly being underestimated. If the sky background level was higher, the index value would be lower. This can be tested using a more advanced sky-level estimation technique. However, when fitting brightest cluster galaxies (BCGs) it is not unusual to find the index value > 4 [12]. Light profiles of BCGs are usually not as simple as those of normal galaxies. They sometimes have multiple components or extended bright halos resulting in stronger light profile curvatures [12]. Therefore, often a single Sersic function is not enough to model the light profile of a BCG. It requires additional and more advanced analysis to determine whether our result is a consequence of the underestimated sky background, oversimplified model, or a combination of both.

5.1.3 Radio source 4092

We analyze the light distribution of the optical counterpart of radio source 4092. Once again, we assume the Sersic profile. Results are shown in figure 5.3 and the final parameters are listed in table 5.3. The estimated sky level value is 1.66988 ADU. Except for the galaxy of interest (in the center of the image), there are also some other sources, the brightest of which is extremely close to the galaxy (both in the plane of the sky and along the line of sight). This additional source is listed in the *ACS I-band Photometry Catalog* [17] of optical sources, and by crossmatching with the catalog of spectroscopic redshifts (M. Salvato, 2017, private communication) we

Figure 5.3: From left to right: the initial subimage from from the unrotated tile containing the optical counterpart of radio source 4092 (in the center) and additional sources, the model image, and the residual image. The orange box, at the bottom right, defines the area used for estimating the sky level. Light blue polygons represent masked areas. The image scale was chosen to make the features in images visible more easily.

Parameter	Value for the galaxy	Value for the additional source
Position [pixels]	$(169.358 \pm 0.008, 164.302 \pm 0.009)$	$(179.019 \pm 0.006, 189.491 \pm 0.007)$
Integrated magnitude [mag]	14.241 ± 0.004	15.606 ± 0.003
Effective radius R_e [pixels]	34.2 ± 0.2	5.93 ± 0.04
Sersic index	4.37 ± 0.02	2.59 ± 0.02
Axis ratio	0.812 ± 0.002	0.770 ± 0.003
Position angle [deg]	-23.2 ± 0.4	-29.4 ± 0.5

Table 5.3: Parameters obtained through fitting the image, i.e. the light distribution of the optical counterpart of radio source 4092 and the light from the additional source.

find its redshift to be $\mathrm{spec\_z} = 0.35289$. This value is approximately the same as the redshifts of the three radio sources of interest and the galaxy group detected in X-ray (see section 3.2). However, there is no radio counterpart in the 3 GHz catalog. The image scale in figure 5.3 was carefully chosen so that it is possible to distinguish between these two close sources, i.e. so that they do not merge into a single source. The light from this additional bright source was successfully fitted away with another Sersic profile (final parameter values are also shown in table 5.3) while simultaneously modeling the galaxy. Other, less bright sources in the image were masked (light blue polygons in figure 5.3), i.e. all pixels that cover them were excluded from the analysis. The goodnes of this fit, i.e. the reduced χ^2 value is 1.39. The optical counterpart of radio source 4092 seems to be somewhat different than the other two (10913, 44). In the initial, and particularly in the residual image, one can spot an excess of light at an unusually large radius from the galaxy's center. Without

additional analysis, it is not clear what kind of feature this is. However, it is evident that it can not be fitted away with the Sersic profile. Moreover, the residual image contains no pattern as the central circularly-shaped residual with the dark center (as opposed to the previous two cases: 10913 and 44). Galfit finds the Sersic index value of $n = 4.37 \pm 0.02$ and the effective radius value in pixels $R_e = 34.2 \pm 0.2$ pixels. This interestingly shaped source requires a more detailed examination and a more complex light model to be explained.

5.2 Analysis of the spatial distribution of optical sources in the environment of radio sources via Voronoi tessellation method

Here, we present the final results of the Voronoi tessellation method (described in section 4.2) performed on the $10' \times 10'$ environment of the three radio sources (whose spatial boundaries are defined and discussed in detail in section 4.2.2), as well as a visual insight into some important parts of the analysis itself. The analysis was performed twice, once working with the more reliable data from the $10' \times 10'$ environment, i.e. only galaxies whose apparent magnitudes in HSC i band are < 24, and then on the less reliable sample also including the fainter objects with $24 < i < 25$, i.e. $i < 25$. We show and discuss the results of both and then compare them.

First, we study the spatial distribution of optical sources in the $i < 24$ sample. We divide the $10' \times 10'$ environment area into smaller cells according to the rules of Voronoi tessellation which is shown in figure 5.4. The same is done with the background sample and it is displayed in figure 5.5. Mean cell areas for these two samples given in deg^2 are:

$$\overline{A_{env}} = (1.5 \pm 0.2) \times 10^{-4} \text{ deg}^2 \quad R = 13\% \tag{5.1}$$

$$\overline{A_{bckg}} = (2.00 \pm 0.04) \times 10^{-4} \text{ deg}^2 \quad R = 2\% \tag{5.2}$$

Where the error of the mean value for each sample (the $10' \times 10'$ environment and the background) is calculated as $\sqrt{\frac{\sum_{i=1}^{N}(X_i - \overline{X})^2}{N(N-1)}}$, $X = A_{env}, A_{bckg}$ and N is the corresponding sample size. R in expressions (5.1) and (5.2) is the relative error. The mean densities of sources are calculated as mean values of sets of reciprocal values $\rho_i = 1/A_i$, $i \in [1, N]$:
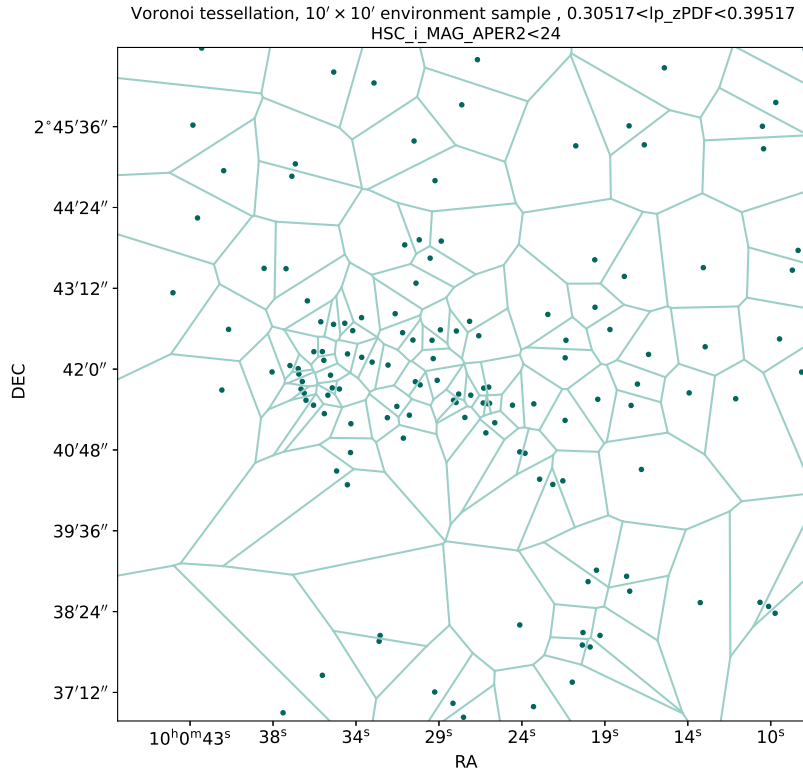
Figure 5.4: Voronoi tesselation on the $10' \times 10'$ environment ($i < 24$). Each dot, i.e. each Voronoi seed is a galaxy and the lines indicate the borders of the Voronoi cells.
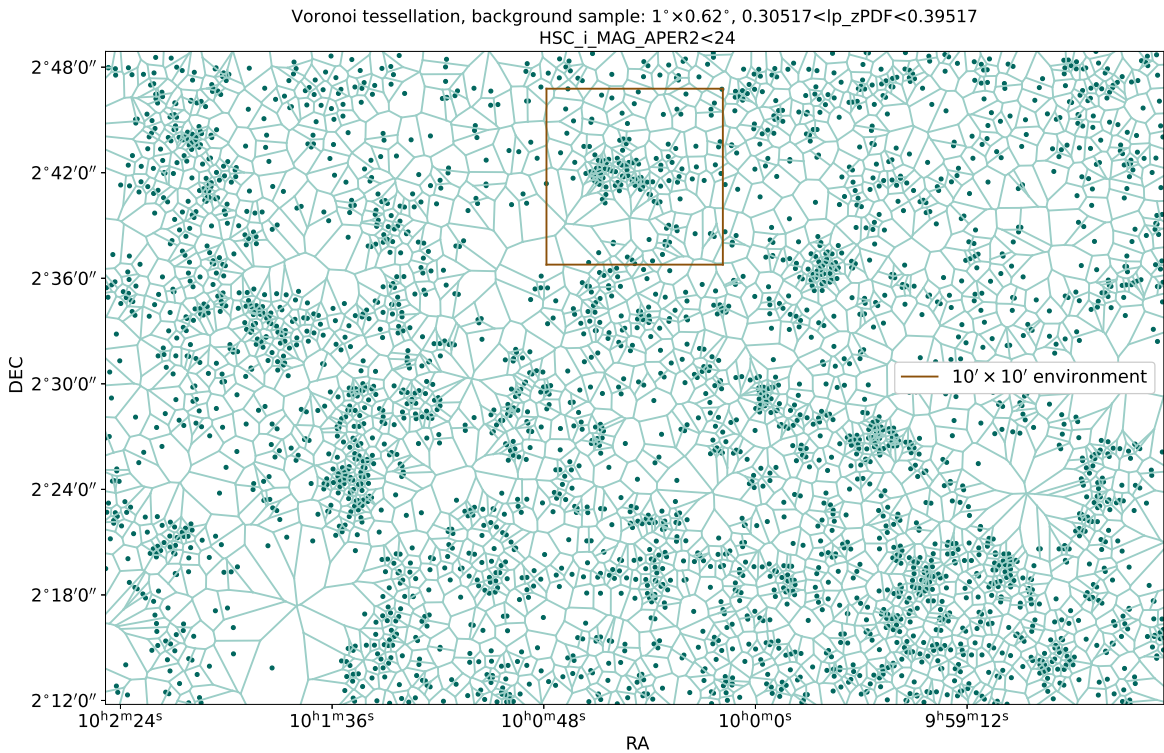
Figure 5.5: Voronoi tesselation on the background sample ($i < 24$). Each dot, i.e. each Voronoi seed is a galaxy and the lines indicate the borders of the Voronoi cells.

$$\overline{\rho_{env}} = (2.3 \pm 0.3) \times 10^4 \text{ deg}^{-2} \quad R = 13\% \tag{5.3}$$

$$\overline{\rho_{bckg}} = (1.37 \pm 0.04) \times 10^4 \text{ deg}^{-2} \quad R = 3\% \tag{5.4}$$

One can see that the mean cell areas are larger, i.e. mean source densities are lower for the background sample. This can be explained by the fact that in the $10' \times 10'$ environment, possible gravitationally bound structures, i.e. increased density of sources is expected, while the background was chosen to be large enough to also contain low and medium dense areas. Furthermore, the relative errors R are lower (3%) for the mean values calculated on the background sample since there the sources are more numerous than in the $10' \times 10'$ environment sample (where the error is 13%). Having calculated this, we express local densities in terms of $\overline{\rho_{env}}$ and $\overline{\rho_{bckg}}$ in the $10' \times 10'$ environment and the background samples respectively. We create cumulative distribution functions of local densities and compare them to find the right density threshold (for details see section 4.2.3). This is shown in figure 5.6. At lower densities distribution functions coincide. This was expected since in the $10' \times 10'$ environment sample, the larger and therefore cells with the lower local densities match the properties of the background. As the density increases, the functions start to differ, allowing us to distinguish the structures in the $10' \times 10'$ environment from the background. Determining the density value where the difference becomes significant is somewhat arbitrary. In this specific case, we single out two densities: $0.75\,\overline{\rho_{env}}$ at 0.58, i.e. at 58th percentile, and $0.95\,\overline{\rho_{env}}$ at 0.68, i.e. at 68th percentile. In case when $i < 25$ filter is applied to the $10' \times 10'$ environment, we follow the same procedure. The mean cell areas and local densities are:

$$\overline{A_{env}} = (8.7 \pm 0.7) \times 10^{-5} \text{ deg}^2 \quad R = 8\% \tag{5.5}$$

$$\overline{A_{bckg}} = (9.6 \pm 0.1) \times 10^{-5} \text{ deg}^2 \quad R = 1\% \tag{5.6}$$

$$\overline{\rho_{env}} = (3 \pm 0.2) \times 10^4 \text{ deg}^{-2} \quad R = 7\% \tag{5.7}$$

$$\overline{\rho_{bckg}} = (2.42 \pm 0.05) \times 10^4 \text{ deg}^{-2} \quad R = 2\% \tag{5.8}$$

Here, the mean cell areas (5.5) and (5.6) take larger values compared to (5.1) and (5.2), while the opposite happens with the mean source densities (5.7) and (5.8)
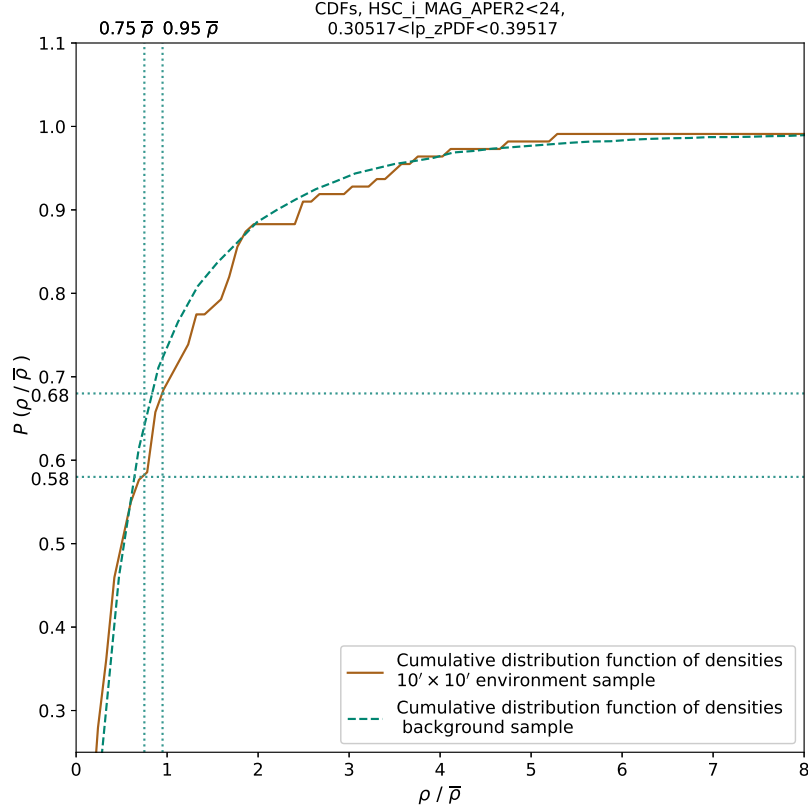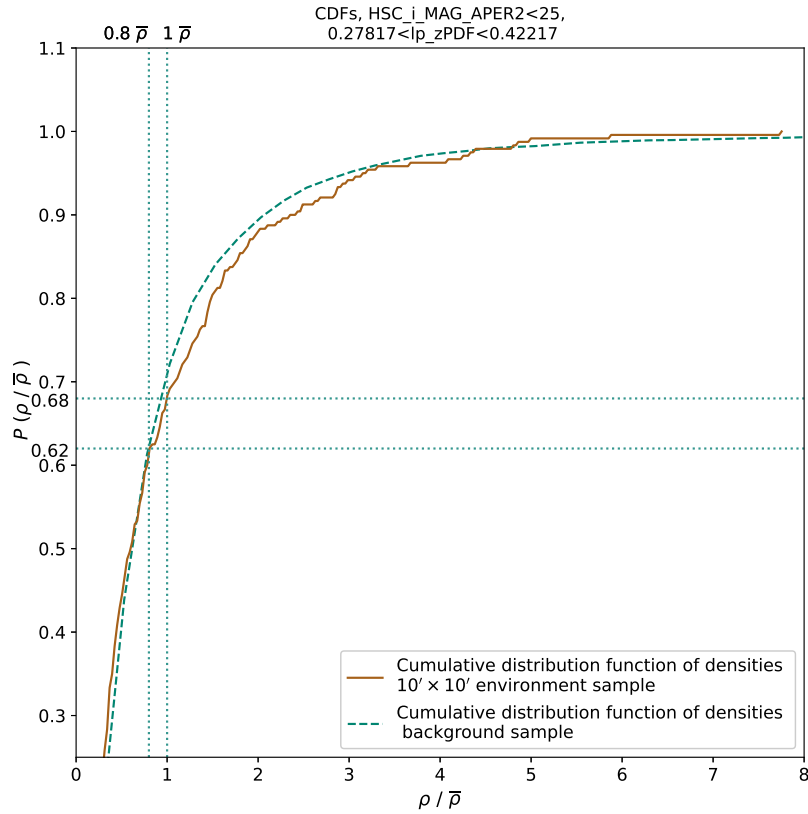
Figure 5.6: Comparison of the cumulative distribution functions of a local galaxy density for two different samples: the $10' \times 10'$ environment and the background. This is for the case $i < 24$. Visually determining the density value where the functions start to differ is somewhat arbitrary. Here, two such values are highlighted: $0.75 \overline{\rho_{env}}$ at 58th percentile, and $0.95 \overline{\rho_{env}}$ at 68th percentile.

compared to (5.3) and (5.4). This is a direct consequence of the increase in the number of sources in both, the $10' \times 10'$ environment and the background that comes with including the less bright ($24 < i < 25$) sources in the analysis. Another direct consequence is the decrease in the relative error R.

Cumulative distribution functions of local densities expressed in terms of the corresponding mean densities (5.7) and (5.8) are shown in figure 5.7. Similarly to the previous case, we visually inspect and compare the functions. Again, two density values are chosen where the functions start to differ significantly: $0.8 \overline{\rho_{env}}$ at 0.62 and $1 \overline{\rho_{env}}$ at 0.68. We use these values as density thresholds, i.e. we keep all the sources whose local densities are above and leave out the ones whose local densities are below them. The former belong to overdense regions, and may further be considered as potential members of the galaxy group. The final result - $10' \times 10'$ environment filtered by the local density is displayed in figure 5.8 and 5.9 for $i < 24$ and $i < 25$ cases respectively. In figure 5.8, the left panel shows the results obtained by

Figure 5.7: Comparison of the cumulative distribution functions of a local galaxy density for two different samples: the $10' \times 10'$ environment and the background. This is for the case $i < 25$. Two values where the functions start to differ from each other significantly are highlighted (although this is arbitrary): $0.8\,\overline{\rho_{env}}$ at 62nd percentile, and $1\,\overline{\rho_{env}}$ at 68th percentile.

using the first density threshold $\rho_{cr} = 0.75\,\overline{\rho_{env}}$, and the right one corresponds to the case $\rho_{cr} = 0.95\,\overline{\rho_{env}}$. By studying these final results, it is noticeable that sources are gathered in the central part of the images where there are also our 3 radio sources (hereafter, we refer to this observed accumulation as the large concentration of galaxies), hinting that this could indeed be a gravitationally bound structure of galaxies like a group. By inspecting the spatial distribution of the sources within this large concentration, one can spot a substructure in its eastern part[37] - a larger accumulation of optical sources tightly gathered around the radio source 4092. In the western part of the large concentration, there is also an accumulation. However, unlike the previous case (4092), here it is hard to tell if the galaxies are leaning more towards the radio galaxy 10913 or 44. It is important to highlight, that our view is partially obscured by the bright foreground stars, i.e. masked regions (previously discussed in sections 3.1.2 and 4.2.4, and here, in the final images 5.8 and 5.9, marked with

---

[37]East is on the left in all images
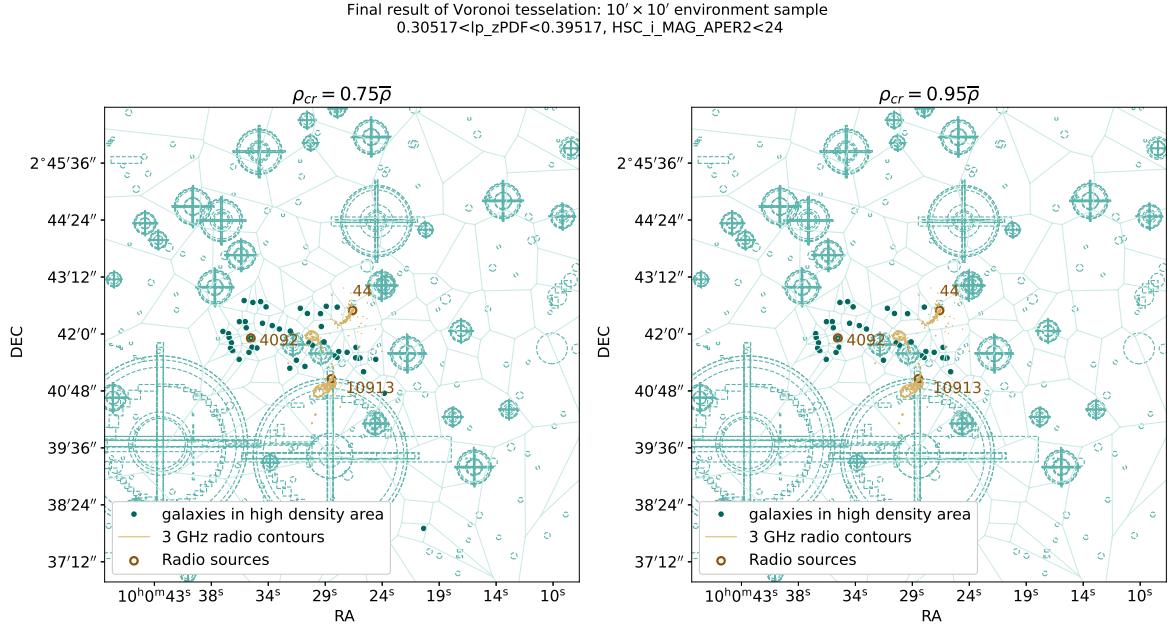
Figure 5.8: Final results of the Voronoi tessellation performed on the $10' \times 10'$ environment ($i < 24$), presented for two different density thresholds: $\rho_{cr} = 0.75\overline{\rho_{env}}$ (left) and $\rho_{cr} = 0.95\overline{\rho_{env}}$ (right). Only galaxies in areas with $\rho > \rho_{cr}$ are shown in images (dark blue points). Light blue circles and polygons represent masked areas in the COSMOS CLASSIC catalog [40] that was the source of data for performing the analysis. The three radio sources, i.e. their optical counterparts are highlighted with dark brown circles, while their radio contours are shown in light brown color.
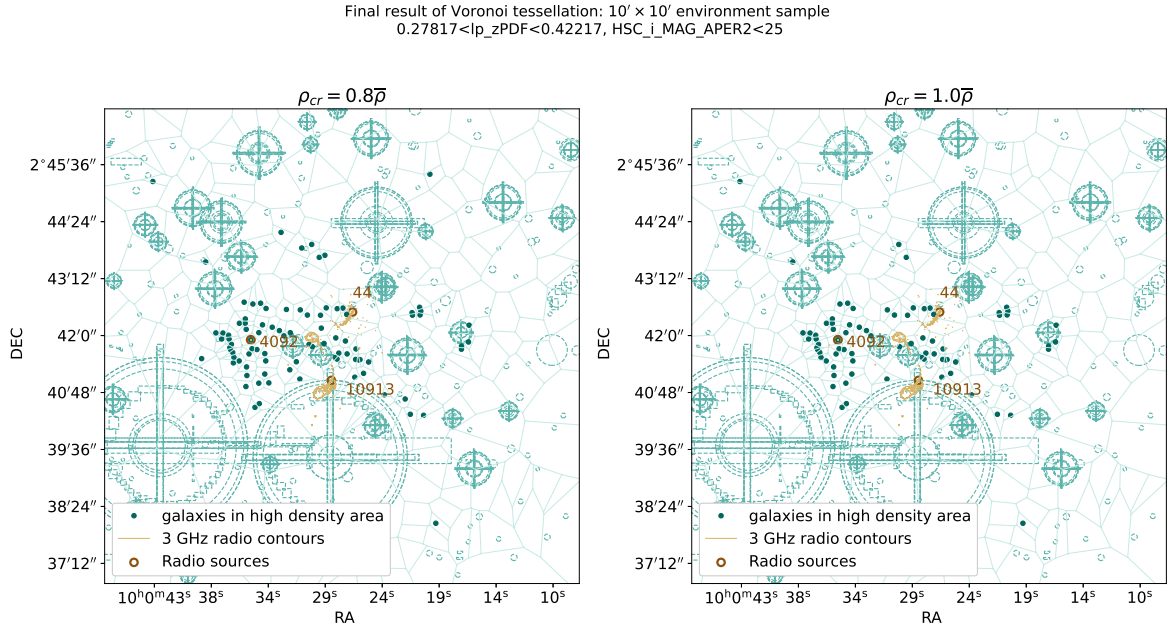
Figure 5.9: Final results of the Voronoi tessellation performed on the $10' \times 10'$ environment ($i < 25$), presented for two different density thresholds: $\rho_{cr} = 0.8\overline{\rho_{env}}$ (left) and $\rho_{cr} = 1\overline{\rho_{env}}$ (right). Only galaxies in areas with $\rho > \rho_{cr}$ are shown in images. Marks and colors are the same as in figure 5.8.

blue circles/shapes). There are two such regions in the middle of the large concentration of galaxies and some more on the outskirts of it, meaning these might not be the actual outskirts. These masked areas limit our ability to study the exact extent of, or the spatial distribution of sources within the detected large concentration of galaxies. Figure 5.9 presents the final results of Voronoi tesselation performed on the $i < 25$ sample of galaxies and filtered by the local density. The main difference from the final results of the Voronoi tessellation performed on the $i < 24$ set is that since the initial number of sources is larger, the sources in overdense areas that appear in the final results are also more numerous (see figures 5.8 and 5.9 to compare). However, one should be careful when examining the result because by including the dimmer sources the room for error grows, i.e. there is a greater chance that a source ended up in the initial set by accident (since its measured and from that calculated properties are less accurate). A lot of these new sources that appear in the final image (figure 5.9) adhere closely to the already existing accumulations of sources (substructures) detected in the results from the previous case (figure 5.8) and discussed above. This encourages the idea of keeping them since it is likely that they are gravitationally bound to the previously detected substructures. However, in some cases, when the new sources are not so closely attached to the already recognized accumulations, it is hard to distinguish whether the new sources are leaning towards them or just "floating" in space. If the latter was the case, they would most likely belong to the background. An example of this kind of confusion is the newly formed accumulation of optical sources placed under (towards the south) the radio source 4092. These few sources may be a part of the background. However, they also may be an extension of the larger accumulation of sources that is visible around the 4092 radio source. On the other hand, some of the new sources seem to form new accumulations. Two examples of that, clumps consisting of 4-5 galaxies are visible in figure 5.9. The first one is centered at: $\text{RA} \approx 10^h\ 00^m\ 31^s$, $\text{DEC} \approx 2°\ 43'\ 48''$ and the other one at $\text{RA} \approx 10^h\ 00^m\ 21^s$, $\text{DEC} \approx 2°\ 42'\ 36''$. These clumps may either be a part of the background, or new, little accumulations that are a bit further from the rest of the structures, but still gravitationally bound to it.

A possible explanation for the distribution of sources detected and described in both cases above lies in the idea that the large concentration is a galaxy group found in the process of formation by merging of smaller groups of galaxies that correspond,

i.e. are roughly centered on the three individual radio sources. This scenario would agree with the somewhat irregular shape of the large concentration and with the existence of more than one bright AGN in it. It would also help to explain the bent radio jets of the radio galaxies 10913 and 44. If this was the case, it seems that the mutual merging of the groups of galaxies around 10913 and 44 would be at a more advanced stage, compared to their merging with the rest, i.e. the third group around the radio source 4092. Moreover, it would be possible that the little clumps of galaxies, detected outside the large central concentration are gravitationally attracted to it and await a similar fate of merging in the future. However, it is impossible to move from these speculations toward conclusions by solely analyzing the spatial distribution of optical sources in the environment of the radio sources. In order to be able to better understand the distribution that we observe, we have to reach out for other, complementary methods, to utilize spectroscopic, rather than photometric data, and to study the area at other wavelengths.

5.3   Color-magnitude diagrams

Here, we present the color-magnitude diagrams (CMDs). The diagrams were created using only optical sources from the overdense regions in the $10' \times 10'$ environment, i.e. using the results of the Voronoi tessellation (preparing samples that we use for the CMDs and choosing photometry was previously discussed in detail in section 4.3). Therefore, the results here are organized in a similar way as the ones in the previous section (5.2). We present a total of 4, i.e. two pairs of diagrams: one pair of CMDs for the case when $i < 24$ filter is applied, and the other pair for the case when $i < 25$ data is used when performing the Voronoi tessellation. The difference between the two CMDs in a pair is in the density threshold used to filter out the sources in less dense regions (threshold values were previously determined in section 5.2). Figures 5.10 and 5.11 display CMDs created for the $i < 24$ and $i < 25$ cases respectively and the corresponding color index histograms. Histograms were created using the Numpy.histogram function in Python with the bins='auto' [38] option. In both images, we additionally detect and mark sources that besides the photometric redshift, also

---

[38]bins='auto' automatically determines a width of bins h based on a given data set, i.e. their count as $ceil(range/h)$. It prefers to use Sturges estimator of bin width for small and Freedman Diaconis estimator for larger sets of data
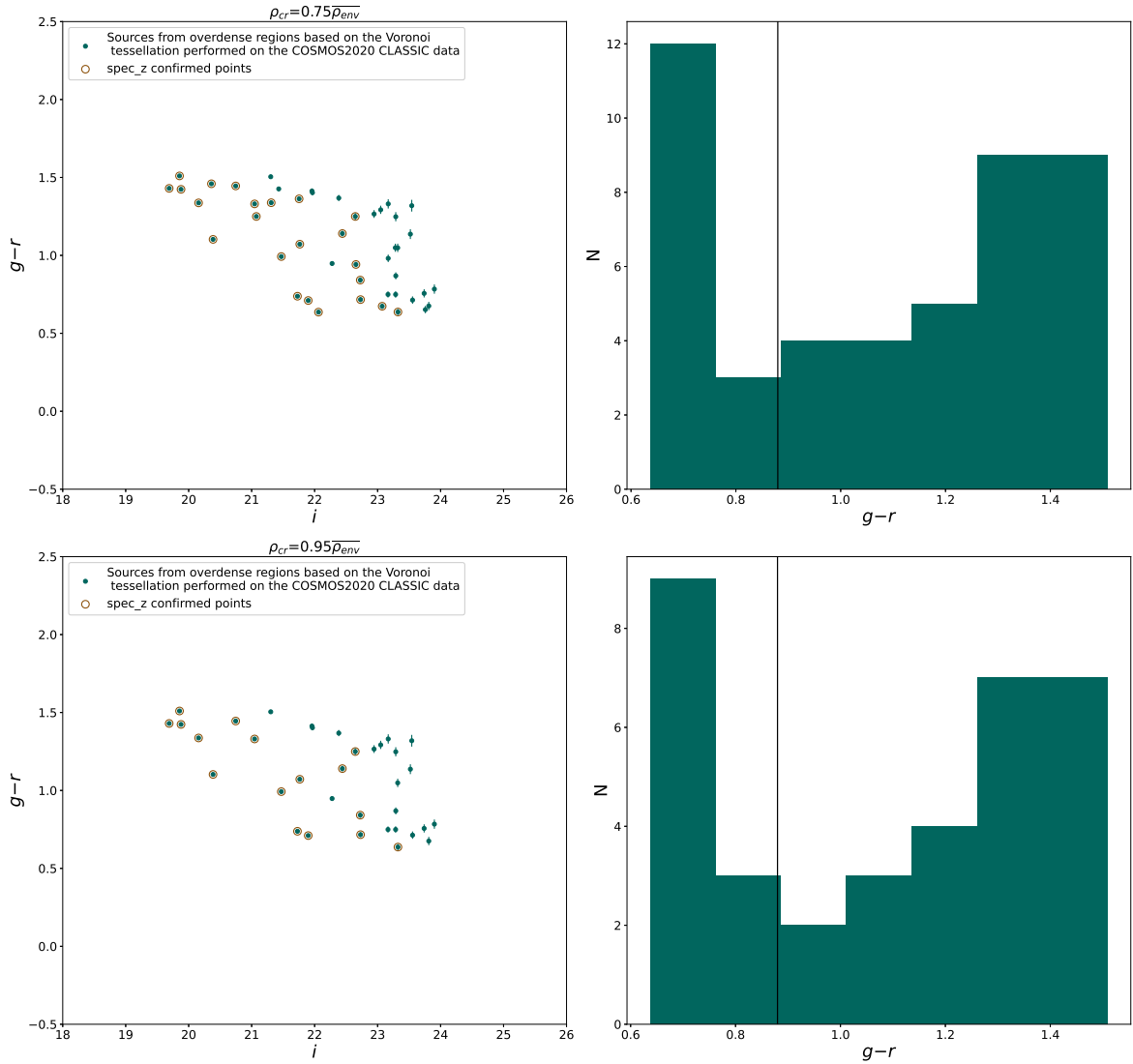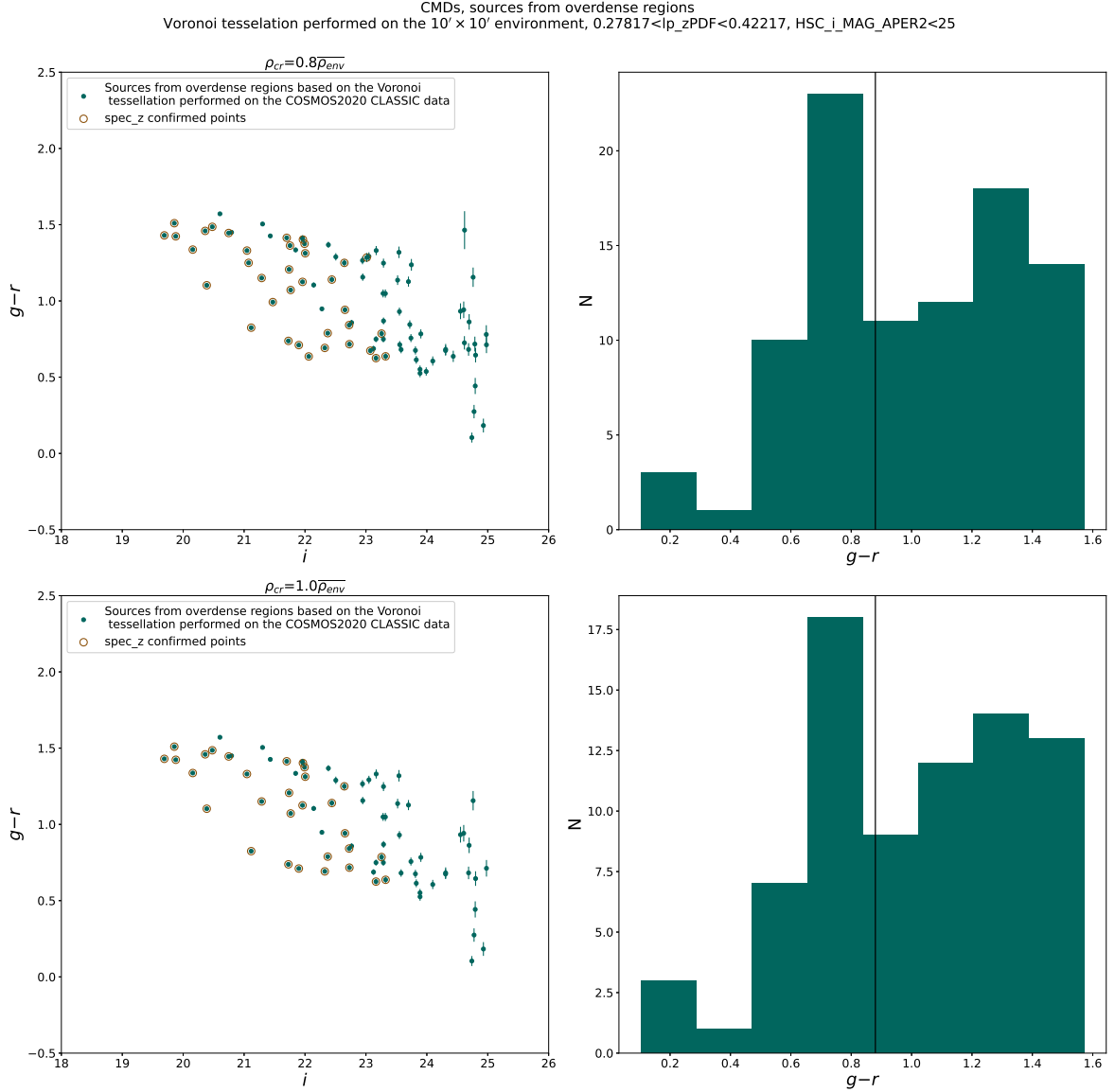
Figure 5.10: Galaxy color-magnitude diagrams created using only galaxies from $i <$ 24, $10' \times 10'$ environment sample that lie in overdense areas (shown in figure 5.8), i.e. with $\rho > \rho_{cr}$ for $\rho_{cr} = 0.75\overline{\rho_{env}}$ (top left panel) and $\rho_{cr} = 0.95\overline{\rho_{env}}$ (bottom left panel). The Y axis displays color indices, i.e. Subaru HSC g and r bands magnitude difference (with the corresponding error bars), and Subaru i band magnitude is on the X axis. Galaxies that also have spectroscopic redshifts, and those values are within the redshift bin used to filter their photometric counterparts are highlighted with light brown circles. Each of the two CMDs also has the corresponding $g-r$ color index histogram (top and bottom right panles for $\rho_{cr} = 0.75\overline{\rho_{env}}$ and $\rho_{cr} = 0.95\overline{\rho_{env}}$, respectively. The black line indicates a rough boundary between more blue and more red galaxies.)

have more accurate spectroscopic redshift and these two values lie in the same range used to filter the catalog to prepare the environment sample ($[\overline{z} - 3\sigma, \overline{z} + 3\sigma]$). In other words, these are sources that have not ended up in the $10' \times 10'$ environment due to their photometric redshift errors and they should be given more weight when

Figure 5.11: Galaxy color-magnitude diagrams created using only galaxies from $i < 25$, $10' \times 10'$ environment sample that lie in overdense areas (shown in figure 5.9), i.e. with $\rho > \rho_{cr}$ for $\rho_{cr} = 0.8\overline{\rho_{env}}$ (top left panel) and $\rho_{cr} = 1\overline{\rho_{env}}$ (bottom left panel). The CMDs are shown with the corresponding color index histograms. The marks and colors are the same as in figure 5.10.

studying the result. For all points, we also plot the corresponding color index (y-axis) error bars, calculated from error values for the HST g and r band magnitudes. The CMDs are made using apparent instead of absolute magnitudes in order not to introduce additional uncertanities due to inaccuracies in the source distances along the line of sight. This should not be a problem since the distances between the sources are negligible compared to their distance from us along the line of sight and therefore the differences between apparent magnitudes of different sources should reflect the ones in their absolute magnitudes.

A long ($\approx 6\,\mathrm{mag}$), nearly horizontal structure is well recognizable in figure 5.11. This is likely a red sequence supporting the idea of the existence of a galaxy group. A similar, however, somewhat shorter (along the x-axis) structure is visible in figure 5.10. This is due to filtering out the dimmer sources ($24 < i < 25$) from the sample of galaxies. Some of the dimmer sources, present in the CMD in figure 5.8, might be members of the potential galaxy group, while the others are there due to error in their photometric redshift. However, this is not a surprise, given that the upper limit of the apparent magnitude, which would mark a strict cut between good (correct) and bad (less correct) data, is impossible to set as such. With cutting off data that is less reliable, also comes a possibility of excluding good data. Furthermore, note (in figures 5.11 and 5.12) that there are two strong color peaks in the CMDs, i.e. in the adjacent histograms that correspond to bluer (the left peak) and redder (the right peak) galaxies.

The recognized structure is $\approx 1\,\mathrm{mag}$ wide along the y-axis, which is also noticeable from the corresponding histograms. It is possible that the sequence would be less wide, i.e. better defined have we worked with spectroscopic instead of photometric redshifts, which remains to be investigated in future work. One possibility, that we test here is that this is not one sequence, but it consists of two or maybe even more sequences/parts that would correspond to potential galaxy groups around (approximately centered on) different radio soruces, laying at slightly different redshifts. We highlight here that, if this was the case it would still be hard to distinguish between different substructures since the difference (in redshift) would be very small and the fact that the potential groups may be in a process of merging would make it even harder. We perform a test, extracting the sources that are closer to each of the three radio sources (44, 10913, and 4092) than to the remaining two of them in the plane of the sky, and then we plot those data on the CMD in another color so we could see if they form their own sequence that we can distinguish from the rest (along the y-axis). The results are shown for $i < 25$, $\rho_{cr} = 0.8\overline{\rho_{env}}$ case in figure 5.12. By visually inspecting the three panels corresponding to the three different versions of this test (one for each radio source), one can easily see that neither of the sets constructed this way stands out from the rest. We end up with a similar result when performing the test on the three remaining samples ($i < 25$, $\rho_{cr} = 1\overline{\rho_{env}}$; $i < 24$, $\rho_{cr} = 0.75\overline{\rho_{env}}$; $i < 24$, $\rho_{cr} = 0.95\overline{\rho_{env}}$). There are more possible reasons for
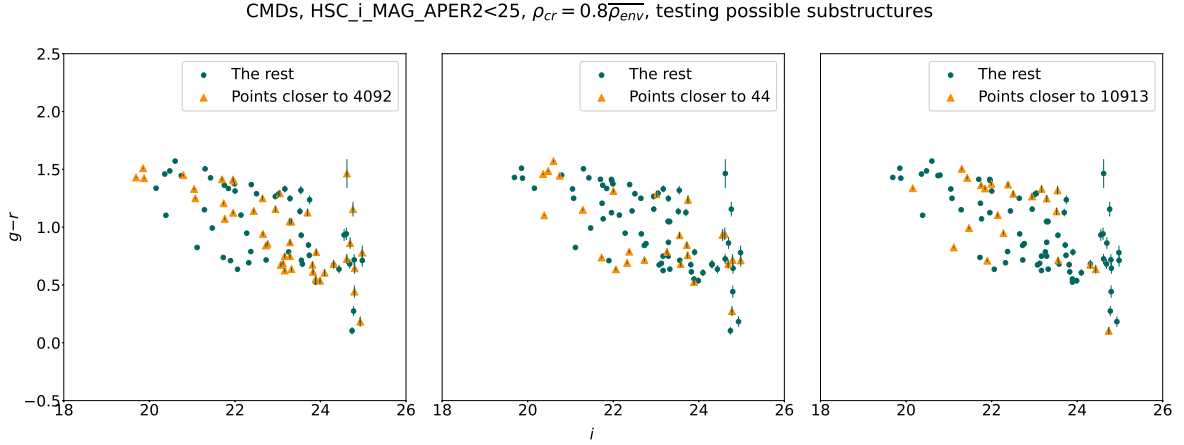
Figure 5.12: Color-magnitude diagram created using galaxies from $i < 25$, $\rho > 0.8\overline{\rho_{env}}$ sample plotted in three different versions, i.e. with galaxies that are closer to each of the three radio sources: 10913, 44, and 4092 being specially marked (orange triangles). No pattern is noticeable in the dependence of the position of a galaxy in the CMD diagram on its position in the plane of the sky (its proximity to one of the radio sources).

this, beginning with the fact that we are working with photometric redshifts, which are not as precise as spectroscopic redshifts. Furthermore, it could be that the CMD does not consist of more but only has one distinguishable sequence, i.e. if smaller galaxy groups were merging, at this point they would be pretty close to each other and already well mixed, however, still not in a relaxed state. Furthermore, the test (which is in 2d only) may be too simple to work in this case. Moreover, here we used the coordinates of the three radio sources as a good approximation for potential groups' centers. A-priori determining the centers of the potential groups by using a more advanced method (for example, the center of X-ray emission or similar) would possibly result in a different test outcome. It may also be a combination of some or all of the above reasons.

We also perform another simple test as follows: we extract all sources from the $i < 25$, $\rho_{cr} = 0.8\overline{\rho_{env}}$ sample that are assigned with a spectroscopic redshift value (marked with light brown circles in figure 5.11) and we plot the histogram of these values. Generally, different choices in the number of histogram bins give different results. Therefore it is important to determine the best one for a given data set. The histogram is shown in figure 5.13 with 4 different binning options: 'auto', 30, 40, and 50. By studying the histograms it is hard to tell if there is one or more smaller groups of galaxies at slightly different redshifts that are merging. When bins=30, there seem to be two different peaks. However, when bins=40 they disappear, i.e. the
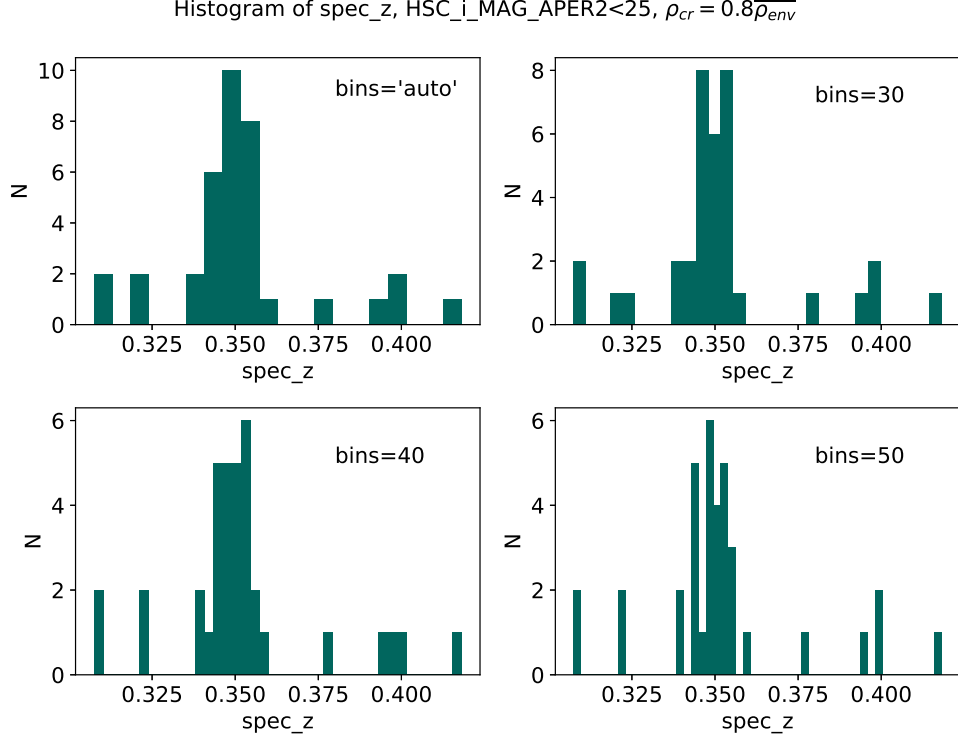
Figure 5.13: Histogram of spectroscopic redshifts of the galaxies from $i < 25$, $\rho > 0.8\overline{\rho_{env}}$ sample (only the ones that have one). Histogram is plotted with different binning options: 'auto', 30, 40, and 50.

distribution again shows just one large concentration of sources around $z_{\mathrm{spec}} \approx 0.35$. We conclude that, with the data set we use, it is not possible to detect two or more distinct galaxy group candidates merging along the third axis (the line of sight). This, however, does not exclude the possibility that a merger exists. It could be either that with this data set we do not have a proper resolution to distinguish between different substructures in the third dimension, or the merger could be mostly taking a place in the plane of the sky.

Finally, we divide the sources into two groups: the bluer ones and the redder ones. We visually determine the rough boundary between the two by inspecting the color index histograms (the black line between the two peaks in figures 5.10 and 5.11). We once again plot the sources in the $(\mathrm{RA}, \mathrm{DEC})$ plane, i.e. we plot the Voronoi diagram in different colors (red for the redder ones and blue for the bluer ones) to test if there exist some patterns in how the sources are spatially distributed depending on their color index. If the potential galaxy group is relaxed, the expected outcome would be to find the redder sources in the central part and the bluer more on the outskirts of the previously detected, large concentration of galaxies. We do this with sources from
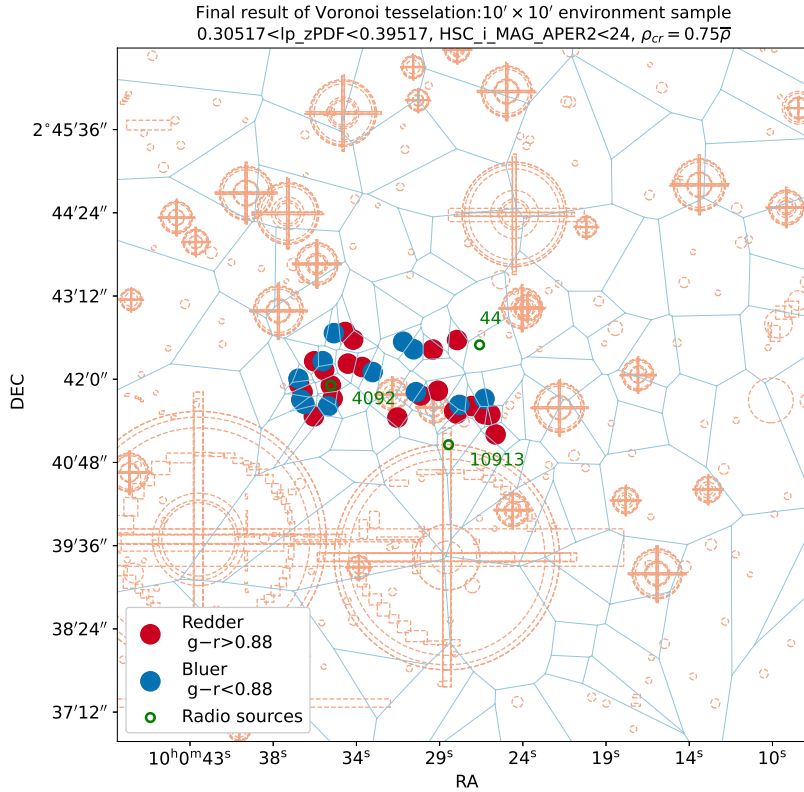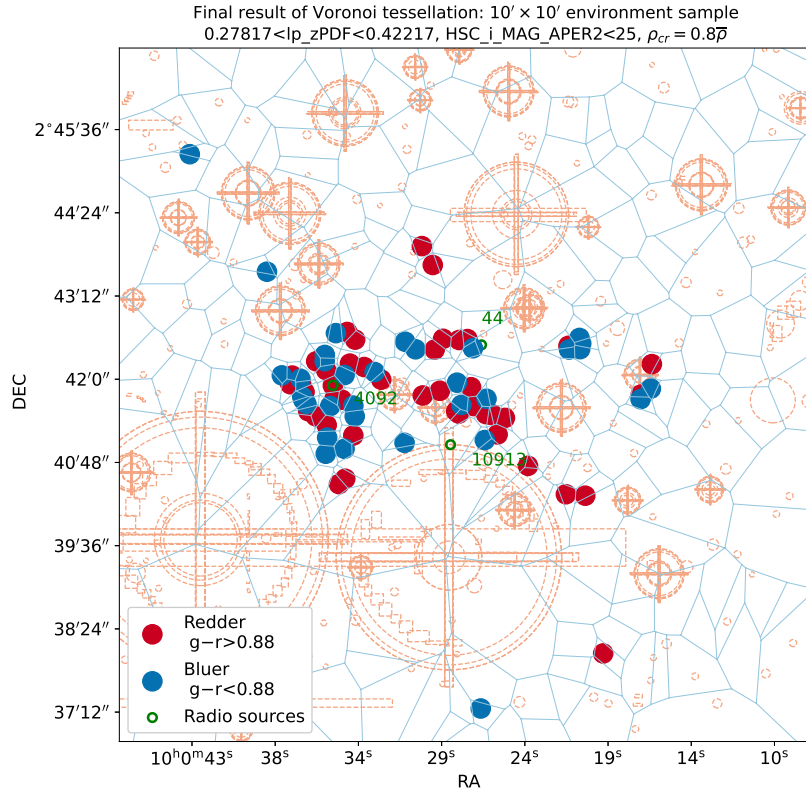
Figure 5.14: Bluer and redder galaxies in the final result of the Voronoi tessellation performed on the environment sample with $i < 24$. Only galaxies with $\rho > 0.75\overline{\rho_{env}}$ are shown. The result presented is the same one as in the left panel of figure 5.8. The only difference is that galaxies are presented in two different colors depending on their color index value. The index value above which galaxies are considered as redder (0.88) was roughly determined by visually inspecting the corresponding color index histogram (upper right panel in figure 5.10).

two samples: $i < 24$, $\rho_{cr} = 0.75\overline{\rho_{env}}$ and $i < 25$, $\rho_{cr} = 0.8\overline{\rho_{env}}$. In both cases ($i < 24$ and $i < 25$) we choose lower from the two density thresholds to work with more data. This is better for creating histograms and it should make detecting patterns in the spatial distribution of the sources depending on their color index easier. For the latter reason, we also plot the sources (points) much larger than in the previous figures. The results are shown in figures 5.14 and 5.15. It seems that there are somewhat more blue sources in the eastern substructure around the radio source 4092 than in the western part where radio galaxies 10913 and 44 reside. However, both, redder and bluer sources are located in the center as well as in the outer parts of the large concentration of galaxies, suggesting that we are likely dealing with a non-relaxed group of galaxies.

Figure 5.15: Bluer and redder galaxies in the final result of the Voronoi tessellation performed on the $10' \times 10'$ environment sample with $i < 25$. Only galaxies with $\rho > 0.8\overline{\rho_{env}}$ are shown. The result presented is the same as in the left panel of figure 5.9. with the difference that galaxies are presented in two different colors depending on their color index value. The index value above which galaxies are considered as redder (0.88) was roughly determined by visually inspecting the corresponding color index histogram (upper right panel in figure 5.11).

6 Conclusion

In this work, we studied three radio sources (10913, 44, and 4092) from the COS-MOS field, i.e. their optical counterparts and their $10' \times 10'$ environment. Two of them (radio galaxies 10913 and 44) have interestingly shaped (extended and bent) morphology, and all three sources lie within a massive galaxy group previously detected through the X-ray emission from its intra-cluster medium. This is consistent with radio sources (especially wide-angle tail galaxies) being often found in centers of galaxy groups or clusters. The main goal here was to investigate this system, i.e. the sources and their environment in the optical regime, as a step towards a better understanding of both, their radio shape and the formation and evolution process of the hosting galaxy group. Optical light distributions of the three galaxies were modeled with Galfit, assuming the Sersic profile and resulting in Sersic index values: 3.946 ± 0.005, 4.77 ± 0.01, and 4.37 ± 0.02 for 10913, 44, and 4092 respectively. According to the results of modeling (both model parameters and residual images), the optical counterparts of radio galaxies 10913 and 44 seem to be elliptical galaxies, possibly with a core. This agrees with the expectations since radio galaxies are usually hosted by bright ellipticals. The light distribution in the central part of the optical counterpart of radio source 4092 follows the Sersic profile well. However, there is an excess of light in its outer parts that can not be fitted away with the same Sersic profile. This galaxy seems to be different from the other two and needs to be investigated further. Errors in the obtained Sersic indices are mostly due to the combination of the insufficiently well-estimated sky level value and the over-simplicity of the used light models, encouraging further research and the use of more advanced methods in estimating the sky level and modeling. Furthermore, we studied the spatial distribution of optical sources in the $10' \times 10'$ environment of the radio sources using the Voronoi tesselation method. An overdensity of galaxies at optical wavelengths was detected around the three radio sources, as expected from the fact that there is a galaxy group detected in X-ray. Optical sources from the more dense areas were extracted as the most probable members of the potential group. This was done according to the a-priori estimated density threshold value, i.e. more different values (and the results for all cases are presented here) since estimating the threshold density is somewhat arbitrary. At all density thresholds, these optical sources (galaxies)

form a large concentration that most probably corresponds to the mentioned group. Moreover, substructures, i.e. smaller accumulations of galaxies within the large concentration are noticeable. The one around radio source 4092, in the eastern part of the large concentration, is best defined, i.e. distinguishable from the rest. The existence of substructures hints that the potential group is not relaxed. Color-magnitude diagrams were created for the most probable members of the potential galaxy group, showing a clearly visible, $\approx 6\,\mathrm{mag}$ long, $\approx 1\,\mathrm{mag}$ wide, and nearly horizontal feature. It is likely a red sequence, suggesting that we are probably dealing with a galaxy group. The color scatter in the sequence may be smaller have we worked with the more precise spectroscopic redshifts instead of photometric redshifts. However, this and other factors that could affect its wideness remain to be investigated. Furthermore, the most probable members of the potential group were divided into two classes by their color index, the redder ones, and the bluer ones, and their spatial distribution (within the potential group) in dependence on their color was studied. Both, redder and bluer galaxies are present in the central as well as in the outer parts of the large concentration (with somewhat more of the bluer ones in its eastern part, around radio source 4092). The latter result, together with the others indicates that the potential group that we analyzed here may not be relaxed. We might have caught it in the process of its creation through the merging of different smaller galaxy groups around each radio source. This scenario offers a possible explanation for the bent shape of jets of radio galaxies 10913 and 44, which could be a consequence of their interaction with the intra-cluster medium while moving through it, with a relative speed being significantly high. The matter requires further research, not just in the optical regime, but also at other wavelengths (especially radio and X-ray).

7 Prošireni sažetak

7.1 Kratki uvod i ciljevi rada

U ovom radu pobliže istražujemo tri radioizvora iz polja COSMOS [33]: 10913, 44 i 4092, ovdje nazvane prema njihovim identifikatorima iz kataloga na $3\,\mathrm{GHz}$ [35]. Sva tri izvora nalaze se unutar iste, masivne grupe galaksija prethodno detektirane na crvenom pomaku $z \approx 0.35$ putem rendgenske emisije od međugalaktičkog medija (*COSMOS X-ray Group Catalog* [9]). Radiogalaksije 10913 i 44 imaju izduženu radiomorfologiju, dok je 4092 točkasti radiovalni izvor. Radiomorfologija galaksija 10913 i 44 nije samo izdužena, već su, štoviše, njihovi mlazovi savijeni u C oblik. Takva morfologija obično se povezuje s boravkom galaksije u grupi ili skupu galaksija. Savijen oblik mlazova pripisuje se interakciji između plazme u mlazovima i međugalaktičkog medija, koji ispunjava prostor između galaksija u skupu ili grupi. Interakcija se događa prilikom njihovog relativnog gibanja, a istraživanja su pokazala da su za takav scenarij potrebne velike relativne brzine [20; 1; 23]. Takve brzine mogu se naći u dinamičnim sustavima (grupama i skupovima) galaksija koji nisu regularni i opušteni, već prolaze kroz proces gravitacijskog međudjelovanja i/ili spajanja s drugim obližnjim sustavima [27; 19; 8; 29; 30]. Savijena radiomorfologija, uz činjenicu da su galaksije prostorno smještene unutar masivne grupe galaksija upućuje na to da bi se i ovdje moglo raditi o takvom slučaju. Kako bi se bolje razumio proces nastanka i razvoja detektirane grupe domaćina te objasnio oblik radio emisije galaksija, nužno je proučavati kako same galaksije, tako i njihovu okolinu. U ovom radu, analiziramo galaksije i njihovu okolinu, dimenzija $10' \times 10'$ (u nastavku teksta, $10' \times 10'$ okolina), na optičkim valnim duljinama.

Prvo, modeliramo raspodjelu svjetla galaksija koristeći program Galfit. Potom, izdvajamo sve optičke izvore koji čine $10' \times 10'$ okolinu radiogalaksija i analiziramo njihovu prostornu raspodjelu metodom Voronoi teselacije. To činimo kako bismo vidjeli postoje li kakva prostorna zgušnjenja te ako da, kako su raspoređena. Provodimo dodatnu analizu nad galaksijama iz $10' \times 10'$ okoline koje su izdvojene kao najvjerojatniji članovi potencijalne grupe galaksija (prema kriteriju gustoće, na temelju rezultata Voronoi teselacije). Kreiramo dijagrame ovisnosti boje o magnitudi galaksija (u nastavku teksta, magnituda-boja dijagrami) kako bismo ispitali vezu između njihovog sjaja i indeksa boje te ispitujemo ovisi li prostorna raspodjela galaksija, odnosno nji-

hov položaj unutar potencijalne grupe o njihovoj boji.

7.2 Podaci

S obzirom na to da je primarni cilj ovog rada optička analiza galaksija i njihova bliskog okruženja, uglavnom radimo s optičkim/blisko infra-crvenim podacima. Ipak, kako bismo mogli bolje motivirati izbor galaksija te bolje razumjeti konačan rezultat potrebni su nam i podaci na drugim valnim duljinama (radiovalno i rendgensko područje). Izvori i podaci su preuzeti iz pregleda neba *Cosmic Evolution Survey* [33] (COSMOS[39]). Radi se o području na nebeskoj sferi, veličine 2 kvadratna stupnja, centriranom na $\mathrm{RA} = 10^h \ 00^m \ 28.6^s$ i $\mathrm{DEC} = +02° \ 12' \ 21.0''$. Ovo je područje dosad opažano gotovo svim većim svjetskim teleskopima, na raznim valnim duljinama (od radiovalnog do rendgenskog područja elektromagnetskog spektra), odnosno postoji mnogo prikupljenih podataka (kataloga i mapa).

Za modeliranje profila svjetla galaksija koristimo slike (mape fluksa), izdvojene iz nerotiranih blokova podataka [14], opaženih u polju COSMOS (f814w filter), detektorom *Wide Field Channel* (WFC) na kameri *Advanced Camera for Surveys* (ACS) teleskopa *Hubble Space Telescope*[40] (HST). U svrhu prezentiranja optičkih ekvivalenata radiogalaksija zajedno s njihovim radio konturama koristimo slike izdvojene iz mozaika [14], koji je dobiven rotiranjem i spajanjem HST-ACS-WFC blokova podataka [14]. U svrhu analize prostorne raspodjele galaksija u $10' \times 10'$ okolini te izrade dijagrama magnituda-boja, koristimo izvore i pripadne podatke o njima (položaji, fotometrijski crveni pomak, magnitude kroz različite filtere) iz *COSMOS2020 CLASSIC* kataloga [40] (u daljnjem tekstu COSMOS CLASSIC). Prilikom uporabe ovog kataloga, vodimo računa o maskiranim područjima, odnosno područjima gdje su podaci zagađeni zbog svijetle zvijezde na doglednici ili defekta kamere. Izvore iz takvih područja odbacujemo (isključujemo iz procesa analize). Na tim mjestima, ostaju rupe u podacima, odnosno veća područja bez izvora. To, u manjoj mjeri, utječe na rezultat analize prostorne raspodjele izvora. Takva područja, u analizi raspodjele optičkih izvora u $10' \times 10'$ okolini radiogalaksija, ne tretiramo posebno, ali su označena u konačnim rezultatima (slikama). Uz fotometrijske crvene pomake, koji su brojniji, ali manje pouzdani, koristimo i spektroskopski utvrđene vrijednosti crvenog pomaka

---

[39]https://cosmos.astro.caltech.edu/page/astronomers
[40]HST - Hubble Space Telescope: https://www.stsci.edu/hst

iz javno nedostupnog kataloga (privatna komunikacija, M. Salvato, 2017.).

Radio podaci korišteni su za predstavljanje tri radiogalaksije od interesa te kako bi se objasnila motivacija za njihov odabir. Koristimo radio mape na $3\,\mathrm{GHz}$ (*VLA-COSMOS 3 GHz continuum mosaic* [35]) i na $1.4\,\mathrm{GHz}$ (*VLA-COSMOS Deep 1.4 GHz mosaic* [31]).

Rendgenski podaci korišteni su ovdje u svrhu dodatnog proučavanja $10' \times 10'$ okoline radiogalaksija, točnije prepoznavanja grupe galaksija koja je njihov domaćin. Koristimo katalog *COSMOS X-ray Group Catalog* [9], koji sadrži grupe galaksija u polju COSMOS, detektirane putem rendgenskog zračenja, podrijetlom od njihovog međugalaktičkog medija.

7.3 Radio izvori od interesa i njihova radio svojstva

Tri radiogalaksije od interesa predstavljene su u tablici 7.1 zajedno s informacijama o njihovom položaju, fluksu zračenja na $3\,\mathrm{GHz}$ te spektroskopskim i fotometrijskim vrijednostima crvenog pomaka. Radi se o međusobno bliskim, svijetlim galaksijama na $z \approx 0.35$.

3 GHz ID	Ime	RA	DEC	3 GHz fluks [μ Jy]	spec_z	phot_z CLASSIC
10913	COSMOSVLA3 J100028.28+024103.3	150.1179	2.6843	32090.0	0.34926	/
44	COSMOSVLA3 J100026.49+024229.7	150.1104	2.7083	2250.2	0.35062	0.3412
4092	COSMOSVLA3 J100035.05+024154.6	150.1461	2.6985	28.3	0.35062	0.3506

Tablica 7.1: Izvori, njihova imena i fluks zračenja na $3\,\mathrm{GHz}$ preuzeti iz kataloga na $3\,\mathrm{GHz}$ [35]. Položaj na nebeskoj sferi i fotometrijski crveni pomak iz COSMOS CLASSIC kataloga [40] te spektrometrijski crveni pomak preuzet iz internog kataloga kolaboracije COSMOS (privatna komunikacija, M. Salvato, 2017).

Radiogalaksije 44 i 10913 prikazane su na $3\,\mathrm{GHz}$ i $1.4\,\mathrm{GHz}$ na slikama 7.1 i 7.2, dok je radioizvor 4092 prikazan na $3\,\mathrm{GHz}$ na slici 7.3, a s obzirom na to da se radi o točkastom izvoru, gotovo isto bi izgledao i na $3\,\mathrm{GHz}$. Slika 7.4 prikazuje sva tri radioizvora u kontekstu njihova okruženja. Radio konture s prethodnih slika prikazane su preko slike u blisko infracrvenom (UltraVISTA[41] $\mathrm{K_s}$), a dodatno je, svijetlo zelenom bojom, označena grupa galaksija prethodno detektirana u rendgenskom području. Karakteristike ove grupe galaksija preuzete su iz kataloga *COS-MOS X-ray Group Catalog* [9]: RA $= 10^h\ 00^m\ 28.21^s$, DEC $= +02°\ 41'\ 33.07''$,

---

[41]https://ultravista.org/
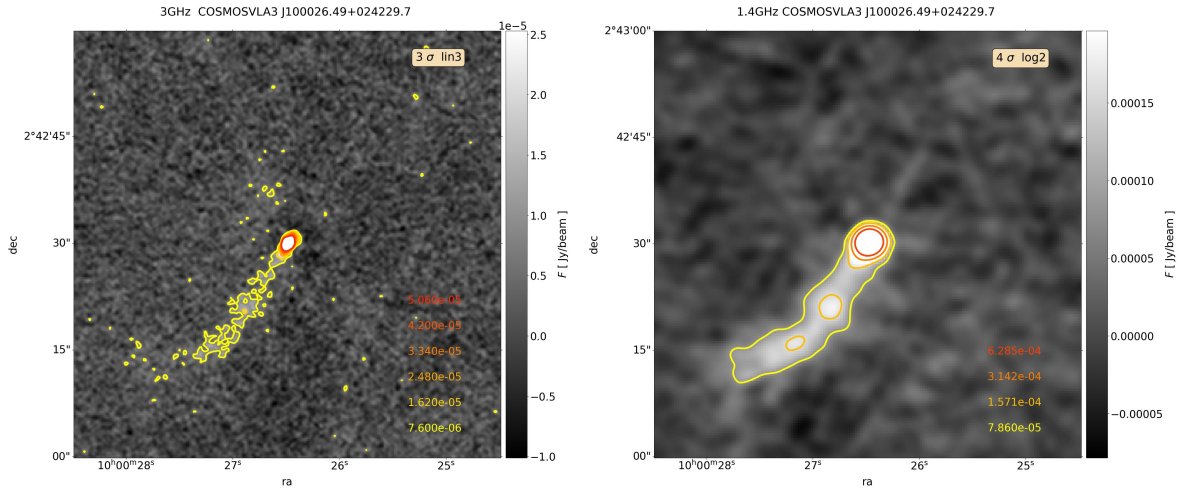
Slika 7.1: Radiokonture za radiogalaksiju 44 na 2 različite frekvencije: $3\,\mathrm{GHz}$ (lijevo) i $1.4\,\mathrm{GHz}$ (desno). Oznaka u gornjem desnom kutu svake od slika pokazuje detalje modela kontura. Prikazuje vrijednost gustoće fluksa na kojoj konture počinju te skalu kontura. Skala je ili logaritamska s bazom 2 (log2), što je ovdje slučaj na $3\,\mathrm{GHz}$ ili linearna (lin N), gdje je N korak između dvaju vrijednosti kontura, što je ovdje korišteno na $1.4\,\mathrm{GHz}$, kako bi se konture bolje razabirale jedne od drugih. Skala slike je od -4σ do 10σ, gdje je σ medijan lokalnog rms (engl. *root mean squared*) šuma. Različite konture predstavljene su u različitim bojama, a odgovarajuće vrijednosti gustoće fluksa prikazane su u istim bojama, u donjem desnom kutu slika.
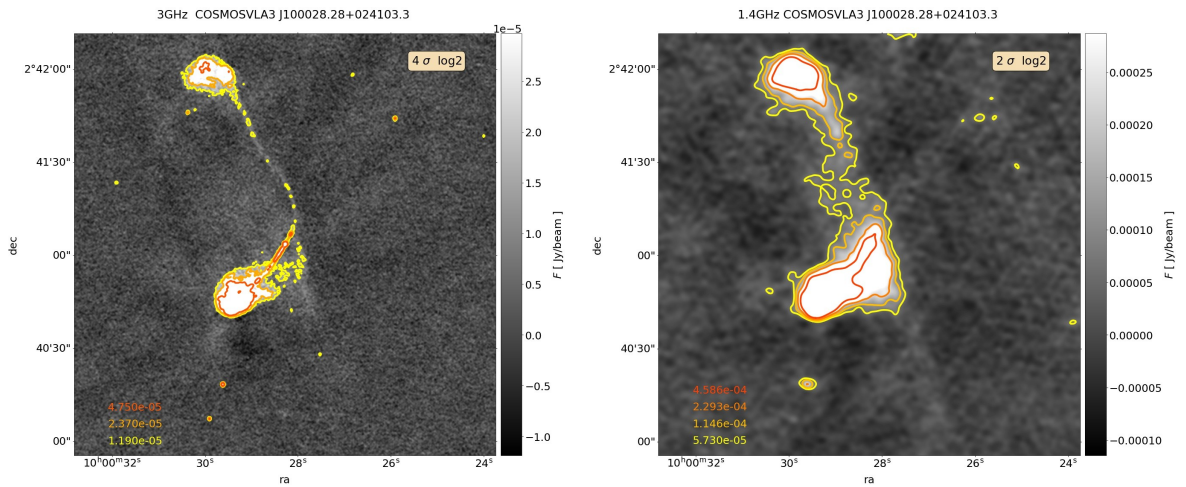
Slika 7.2: Konture za radiogalaksiju 10913 na 2 različite frekvencije: $3\,\mathrm{GHz}$ (lijevo) i $1.4\,\mathrm{GHz}$ (desno). Oznake u gornjem desnom kutu slika pokazuju detalje modela kontura. Na obje frekvencije, konture su prikazane (i najbolje su međusobno razlučene) na logaritamskoj skali s bazom 2. Skala slike je od -4σ do 10σ, gdje je σ medijan lokalnog rms (engl. *root mean squared*) šuma.

$z = 0.349$, $r_{200} = 2.8'$, $m_{200} = (9.1 \pm 0.3) \times 10^{13}\,M_\odot$. Ovdje je r_{200} radijus na kojem je gustoća međugalaktičkog medija 200 puta veća od kritične gustoće svemira[42], a koji je korišten za prikaz grupe na slici 7.4.

---

[42]Kritična gustoća svemira je gustoća materije koja odgovara ravnom svemiru: $\rho_c \approx 10^{-26} kg/m^3$
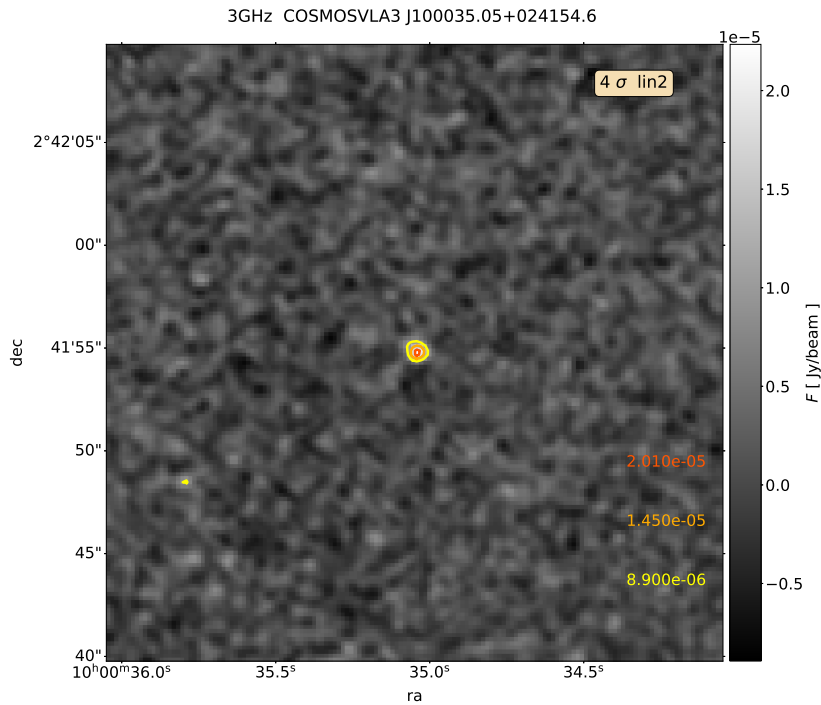
Slika 7.3: Konture za radioizvor 4092 na $3\,\mathrm{GHz}$. Oznaka u gornjem desnom kutu pokazuje detalje modela kontura. Upotrebljena je logaritamska skala s bazom 2. Skala slike je od -4σ do 10σ, gdje je σ medijan lokalnog rms (engl. *root mean squared*) šuma.

7.4   Prilagodba svjetla galaksija na modele

Kako bismo modelirali raspodjelu optičkog svjetla galaksija, koristimo Galfit. Galfit je astronomski softver koji upotrebljava matematičke funkcije kako bi opisao profile svjetla galaksija i/ili njihovih pojedinih komponenti. U svrhu ove analize, upotrijebili smo slike galaksija izdvojene iz nerotiranih blokova podataka [14] dobivenih procesuiranjem *Hubble Space Telescope* (HST) - *Advanced Camera For Surveys* (ACS) - *Wide Field Channel* (WFC) opažanja polja COSMOS kroz f184w filter.

Kako bi prilagodba svjetla na profile bila što uspješnija, unaprijed su (za Galfit) pripremljeni slika funkcije širenja točke (engl. *point spread function*) te za svaku od tri slike galaksija, pripadna lista/slika piksela koji ne bi trebali biti uključeni prilikom modeliranja (maske). Slike galaksija, zbog naknadnog procesuiranja [14] prije svoje objave, nisu iste rezolucije kao slika funkcije širenja točke, koja proizlazi direktno iz karakteristika detektora na ACS kameri. Galfit zahtjeva da te dvije slike budu jednake rezolucije ili da slike galaksija budu lošije rezolucije za cjelobrojni faktor. Stoga je funkcija širenja točke pripremljena pomoću softvera TinyTim [15] s namjerno većom rezolucijom od $(\mathrm{dx}, \mathrm{dy}) = (0.010, 0.010)\ \mathrm{arcsec/pixel}$ kako bi bila za cjelobrojni faktor
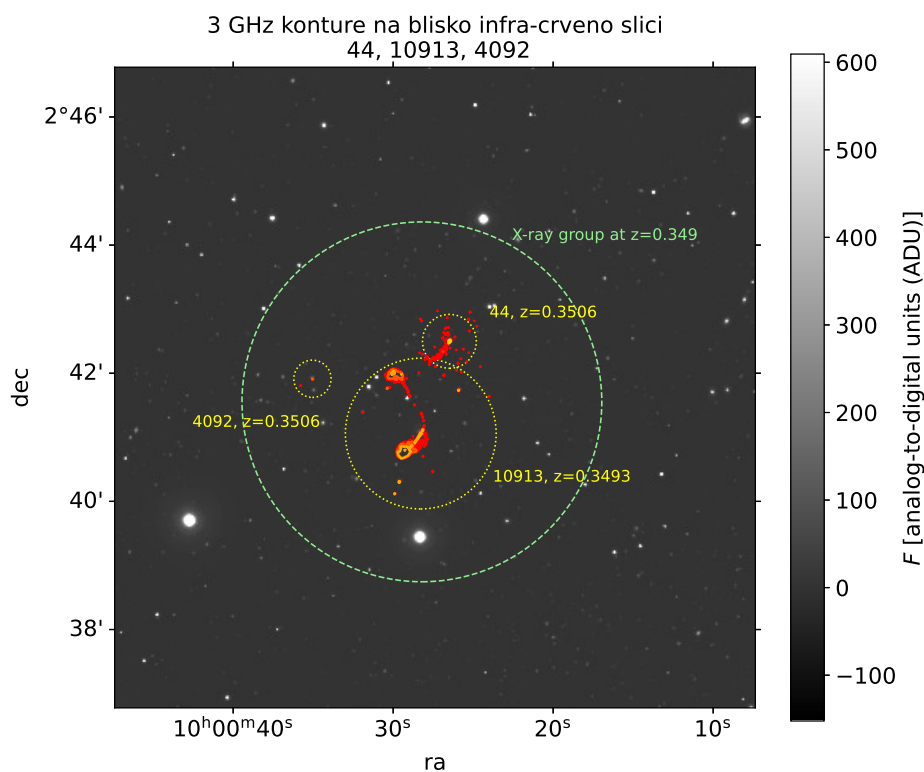
Slika 7.4: Sva tri izvora u kontekstu njihovog okruženja, tj. njihove radiokonture superponirane na sliku u blisko infracrvenom području (UltraVISTA K_s). Pojedini izvori zaokruženi su žutom bojom kako bi se lakše istaknuli u odnosu na svoju okolinu na slici, a veći, svijetlozeleni krug predstavlja grupu galaksija, detektiranu u rendgenskom području (*COSMOS X-ray Group Catalog* [9]). Radijus grupe r_{200} uzet je iz kataloga, a predstavlja radijus na kojem je gustoća međuzvijezdanog medija 200 puta veća od kritične gustoće svemira.

bolja od rezolucije slika galaksija $(\mathrm{dx}, \mathrm{dy}) = (0.030, 0.030)$ arcsec/pixel. Maskirana područja određena su vizualnim analiziranjem slika galaksija u programu DS9 [11] te su označena svijetlo plavim poligonima na konačnim slikama. Maskirani su svi izvori koji nisu sama galaksija, a koji nisu mogli biti istovremeno (tijekom procesa modeliranja svjetla galaksije) modelirani drugim profilom na jednostavan način. Za nekolicinu svijetlih izvora na slikama, primijenjeno je ovo posljednje rješenje istovremenog modeliranja, pri čemu je pretpostavljen Sersicov profil (opisan u nastavku teksta) za dodatni izvor. Isti profil korišten je i za prilagodbu svjetla galaksija. Za potrebe analize, unaprijed je procijenjen nivo (svjetlina) pozadine, odnosno neba na pojedinim slikama te je fiksiran na tu vrijednost prilikom procesa prilagodbe svjetla. Svjetlina neba određena je za svaku od tri slike kao medijan vrijednosti fluksa unutar pripadnog poligona (dijela slike) koji obuhvaća samo uzorak pozadine. Poligoni su, na svakoj od tri slike, određeni vizualnom analizom u DS9 [11], a u konačnim

rezultatima modeliranja (slike 7.5, 7.6 i 7.7), označeni su narančastom bojom.

Radioizvori, u optičkom području, uglavnom odgovaraju svijetlim, masivnim, eliptičnim galaksijama. Takve galaksije često su dobro opisane Sersicovim profilom, od kojeg i mi polazimo u prilagođavanju svjetla galaksija na modele [44; 43]:

$$I(R) = I_e \exp \left\{ -b_n \left[\left(\frac{R}{R_e} \right)^{1/n} - 1 \right] \right\} \tag{7.1}$$

Ovdje je R projicirana udaljenost od centra galaksije, R_e efektivni radijus, odnosno radijus koji obuhvaća pola ukupnog svjetla koje galaksija emitira, dok je n Sersicov indeks, odnosno mjera zakrivljenosti profila. Koristeći ovdje opisanu metodu, dobivamo za vrijednosti Sersicovog indeksa i efektivnog radijusa R_e galaksija u pikselima: $n = 3.946 \pm 0.005$, $R_e = 90.8 \pm 0.2$ piksela za 10913, $n = 4.77 \pm 0.01$, $R_e = 44.8 \pm 0.2$ piksela za 44 te $n = 4.37 \pm 0.02$, $R_e = 34.2 \pm 0.2$ piksela za 4092. Vizualno su rezultati modeliranja prikazani na slikama 7.5, 7.6 i 7.7., a liste svih parametara dobivenih modeliranjem galaksija (i drugih izvora na slikama) nalaze se u tablicama 7.2, 7.3 i 7.4 za optičke ekvivalente radioizvora 10913, 44 i 4092 respektivno. Prilikom modeliranja svjetla optičkih ekvivalenata radio izvora 10913 i 4092, također je istovremeno provedeno modeliranje njima bliskih, svijetlih izvora kako bi se oni uklonili, odnosno kako njihovo svjetlo ne bi utjecalo na rezultat za glavne izvore.

Parametar	Vrijednost za galaksiju	Vrijednost za dodatni izvor
Pozicija [pikseli]	$(253.233 \pm 0.005, 253.547 \pm 0.004)$	$(243.361 \pm 0.007, 196.657 \pm 0.008)$
Integrirana magnituda [mag]	12.326 ± 0.001	15.936 ± 0.002
Efektivni radijus R_e [pikseli]	90.8 ± 0.2	6.95 ± 0.03
Sersicov indeks	3.946 ± 0.005	1.833 ± 0.009
Omjer osi	0.7195 ± 0.0005	0.770 ± 0.002
Pozicijski kut [stupnjevi]	-50.43 ± 0.07	13.0 ± 0.4

Tablica 7.2: Parametri dobiveni prilagodbom svjetla galaksije (optičkog ekvivalenta radiogalaksije 10913) i dodatnog izvora na Sersicove modele.

U rezultatima su, za svaku od tri galaksije, prikazani početna slika galaksije nad kojom se provodi modeliranje, slika modela izvrijednjenog za parametre koji su dobiveni modeliranjem te rezidualna slika, odnosno svjetlo koje ostaje kad se od početne slike oduzme slika modela. Galfit, uz svako modeliranje, daje i pripadnu χ^2 vrijednost, koja je svojevrstan matematički pokazatelj koliko je model dobar za dani set podataka. χ^2 vrijednosti za modeliranje slika optičkih ekvivalenata radioizvora

Parametar	Vrijednost za galaksiju
Pozicija [pikseli]	$(253.980 \pm 0.005, 252.460 \pm 0.005)$
Integrirana magnituda [mag]	13.346 ± 0.002
Efektivni radijus R_e [pikseli]	44.8 ± 0.2
Sersicov indeks	4.77 ± 0.01
Omjer osi	0.8124 ± 0.0009
Pozicijski kut [stupnjevi]	7.7 ± 0.2

Tablica 7.3: Parametri dobiveni prilagodbom svjetla galaksije (optičkog ekvivalenta radiogalaksije 44) na Sersicov model.

Parametar	Vrijednost za galaksiju	Vrijednost za dodatni izvor
Pozicija [pikseli]	$(169.358 \pm 0.008, 164.302 \pm 0.009)$	$(179.019 \pm 0.006, 189.491 \pm 0.007)$
Integrirana magnituda [mag]	14.241 ± 0.004	15.606 ± 0.003
Efektivni radijus R_e [pikseli]	34.2 ± 0.2	5.93 ± 0.04
Sersicov indeks	4.37 ± 0.02	2.59 ± 0.02
Omjer osi	0.812 ± 0.002	0.770 ± 0.003
Pozicijski kut [stupnjevi]	-23.2 ± 0.4	-29.4 ± 0.5

Tablica 7.4: Parametri dobiveni prilagodbom svjetla galaksije (optičkog ekvivalenta radioizvora 4092) i dodatnog izvora na Sersicove modele.
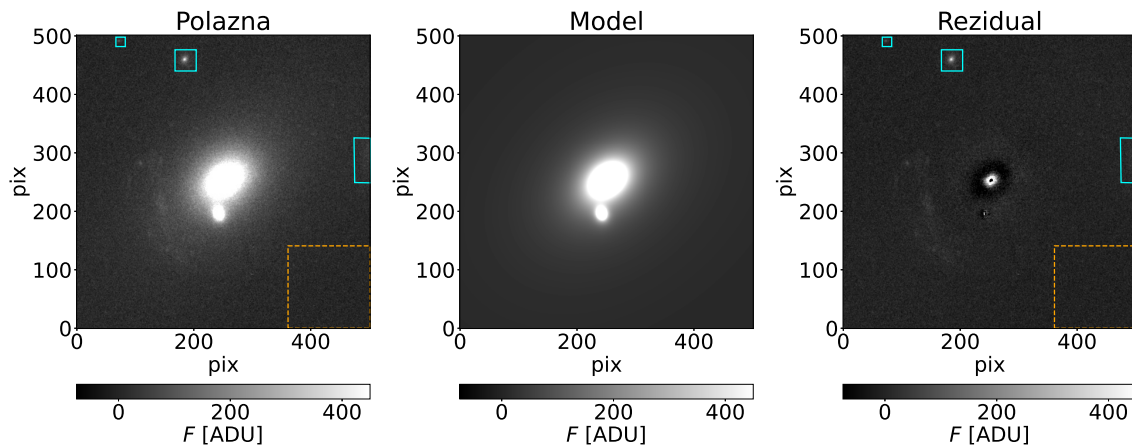
Slika 7.5: Redom, s lijeva na desno: slika izdvojena iz nerotiranog bloka HST-ACS-WFC podataka koja sadržava optički ekvivalent radiogalaksije 10913 (izvor u centru slike) te dodatne izvore, slika modela i rezidualna slika (dobivena oduzimanjem modela od polazne slike). Područje sa slike korišteno za procjenjivanje pozadine, odnosno svjetline neba označeno je narančastim poligonom u donjem, desnom kutu. Svijetlo plavi poligoni su maskirana područja, odnosno pikseli koji su isključeni iz analize. Skala slike (u jedinicama ADU - engl. *analog-to-digital units*) odabrana je s ciljem da objekti na slikama budu jasnije vidljivi.

10913, 44 i 4092 su redom: 0.59, 0.82 i 1.39. Međutim, već proučavanjem rezidualnih slika, moguće je procijeniti koliko je modeliranje bilo uspješno. Vidimo sa slika 7.5, 7.6 i 7.7 da je modeliranjem uspješno uklonjena većina svjetla. Ipak, u rezidualnim slikama za galaksije 44 i 10913, moguće je uočiti centralni kružni objekt s tamnim središtem. Takav oblik pokazuje nam da korišteni model svjetla daje prevelike
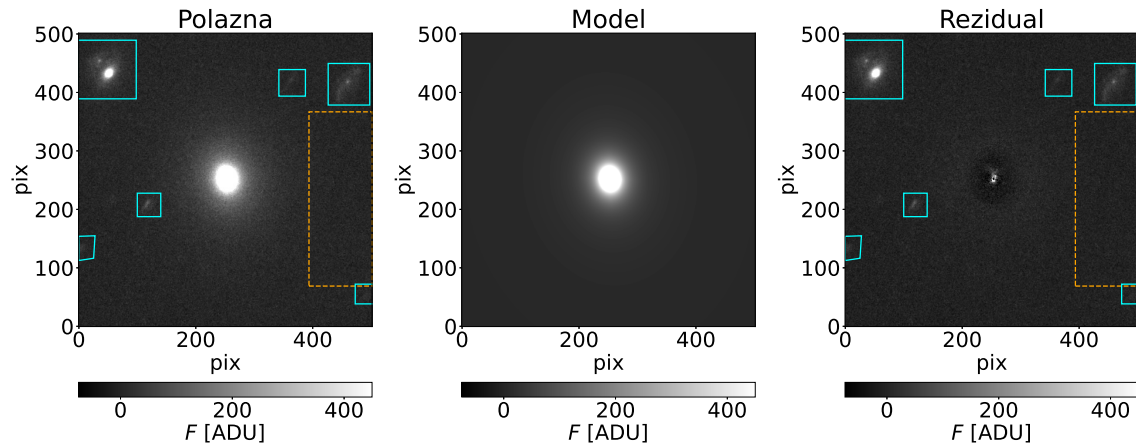
Slika 7.6: Redom, s lijeva na desno: slika izdvojena iz nerotiranog bloka HST-ACS-WFC podataka koja sadržava optički ekvivalent radiogalaksije 44 (izvor u centru slike) te dodatne izvore, slika modela i rezidualna slika. Područje sa slike korišteno za procjenjivanje pozadine, odnosno svjetline neba označeno je narančastim poligonom uz desni rub. Svijetlo plavi poligoni su maskirana područja. Skala slike (u jedinicama ADU - engl. *analog-to-digital units*) odabrana je s ciljem da objekti na slikama budu jasnije vidljivi.
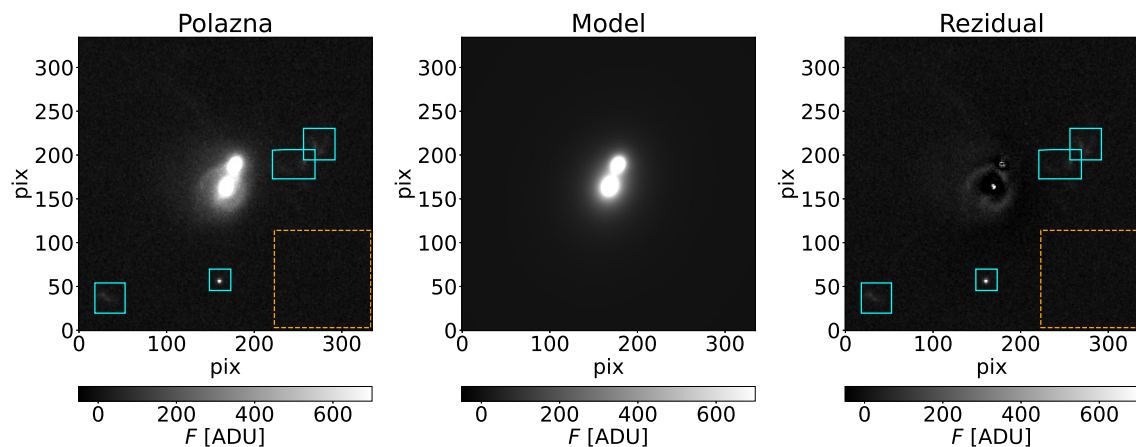
Slika 7.7: Redom, s lijeva na desno: slika izdvojena iz nerotiranog bloka HST-ACS-WFC podataka koja sadržava optički ekvivalent radio izvora 4092 (izvor u centru slike) te dodatne izvore, slika modela i rezidualna slika. Narančasti poligon (donji desni kut) označava područje korišteno za procjenjivanje svjetline neba. Svijetlo plavi poligoni su maskirane regije. Skala slike (u jedinicama ADU - engl. analog-to-digital units) odabrana je s ciljem da objekti na slikama budu jasnije vidljivi.

vrijednosti u samom centru galaksije te ujedno postavlja gornju granicu za Sersicov indeks. Događa se da svjetlost u središtima galaksija odudara od modela koji dobro opisuju ostatak galaksije, a često je uzrok postojanje jezgre galaksije [10]. Kako bi se profil svjetla mogao bolje modelirati, potrebno je koristiti složeniji model od samo Sersicove funkcije. Kod treće galaksije, optičkog ekvivalenta radioizvora 4092, ne nailazimo na takav oblik u centralnom dijelu. Međutim, u ovom slučaju, ostaje višak

svjetla u vanjskim dijelovima galaksije koji se ne može dobro modelirati korištenim Sersicovim profilom. Točnost konačnih rezultata modeliranja također ovisi o procjeni svjetline neba (koja je napravljena unaprijed). Bolje modeliranje raspodjele svjetla zahtjeva složenije modele i naprednije metode u procjeni svjetline neba.

7.5 Analiza prostorne raspodjele optičkih izvora u okolini radioizvora metodom Voronoi teselacije

Radiogalaksije, odnosno njihovi svijetli optički ekvivalenti često leže u središtima grupa ili skupova galaksija. Svojstva radiogalaksija mogu uvelike ovisiti o karakteristikama njihova okruženja, stoga ih uvijek valja promatrati u kontekstu njihove okoline. Radioizvori 10913, 44 i 4092 nalaze se unutar granica ($r < r_{200}$, vidi poglavlje 7.3) iste grupe galaksija, prethodno detektirane u polju COSMOS putem rendgenskog zračenja od međugalaktičkog medija. Mi izdvajamo optičke izvore koji čine blisku okolinu ovog radiosustava te potom analiziramo njihovu prostornu raspodjelu metodom Voronoi teselacije. Veličinu okoline radioizvora nad kojom provodimo analizu određujemo tako da ona bude dovoljno velika da bi mogla obuhvatiti potencijalne strukture poput grupa ili skupova galaksija, ali ne prevelika kako analiza ne bi postala bespotrebno komplicirana i/ili zahtjevna. Stoga, izdvajamo sve optičke izvore iz COSMOS CLASSIC kataloga [40] unutar $10' \times 10'$ područja na nebeskoj sferi, centriranog na RA i DEC koordinatama dobivenim usrednjavanjem položaja radiogalaksija 10913 i 44. U trećoj dimenziji, odnosno duž doglednice filtriramo izvore prema pravilu $z \in [\overline{z} - 3\sigma,\, \overline{z} + 3\sigma]$. Ovdje je $\overline{z}$ srednja vrijednost spektrometrijskih crvenih pomaka radioizvora, a σ je mjera preciznosti fotometrijskih crvenih pomaka izvedena kroz usporedbu s njihovim spektroskopskim verzijama [40]. Dodatno su primijenjeni filter za maskirana područja (propušteni su samo izvori u nemaskiranim područjima) te filter na iznos Subaru/HSC i magnitude (u jednom slučaju, propušteni svi izvori s magnitudom $i < 24$, a u drugom $i < 25$). Bitno je napomenuti kako je vrijednost gore objašnjenog parametra σ, pa tako i debljina uzorka galaksija u trećoj dimenziji drugačija za slučaj $i < 24$ i slučaj $i < 25$. Galaksije većeg sjaja, odnosno one s manjom i magnitudom imaju bolje/preciznije izmjerene, pa tako i iz toga posredno određene veličine, uključujući i vrijednost fotometrijskog crvenog pomaka. Stoga je pripadni σ manji u slučaju $i < 24$ uzorka i iznosi 0.015, dok za slučaj $i < 25$ iznosi
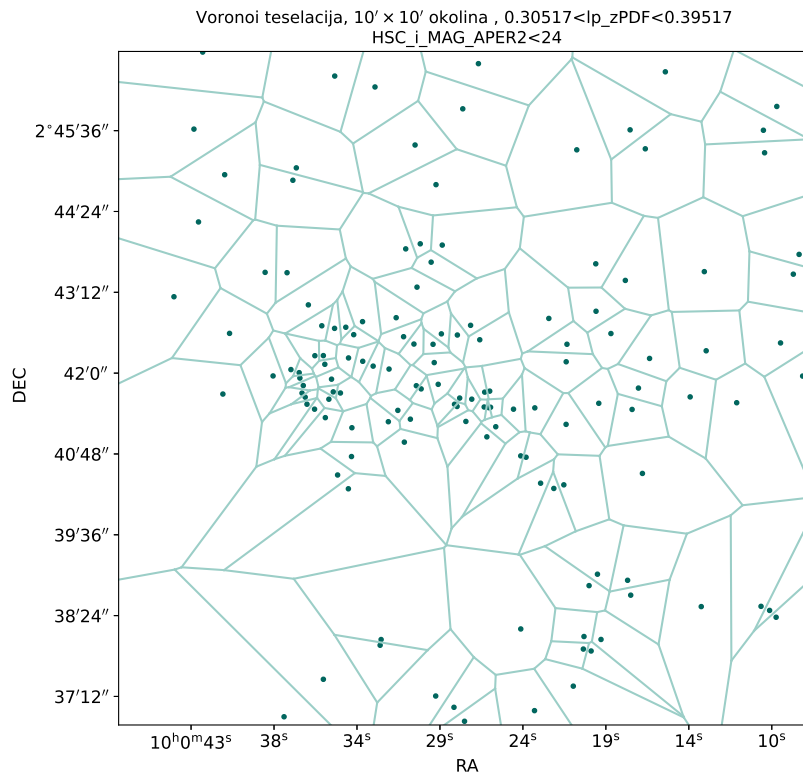
Slika 7.8: Voronoi teselacija na uzorku $10' \times 10'$ okoline sustava radioizvora 10913, 44 i 4092. Uzorak galaksija filtriran je po magnitudi prema $i < 24$. Svaka točka je jedno Voronoi sjeme, odnosno jedna galaksija, a linije označavaju granice Voronoi ćelija.

0.024.

Analiza prostorne raspodjele optičkih izvora provedena je metodom Voronoi teselacije. Radi se o metodi koja dijeli ukupno područje (površinu) u više manjih poligona (Voronoi ćelija) od kojih svaki pripada točno jednoj točki (Voronoi sjemenu), u ovom slučaju galaksiji. Sve prostorne točke unutar pojedine ćelije bliže su datom Voronoi sjemenu (galaksiji) nego bilo kojem drugom iz uzorka nad kojim se provodi analiza. Što je manje galaksija u nekom području, to će površine ćelija biti veće, a njihovi inverzi ($\rho_i = 1/A_i$, gdje i ide po svim galaksijama, odnosno ćelijama) manji. Ova metoda omogućuje da kvantificiramo i međusobno usporedimo lokalne gustoće galaksija u različitim dijelovima $10' \times 10'$ okoline radioizvora.

Kako bismo posebno izdvojili one galaksije iz $10' \times 10'$ okoline koje se nalaze u područjima s povećanom lokalnom gustoćom izvora, odnosno najvjerojatnije članove potencijalne grupe galaksija, prvo određujemo prag gustoće ρ_{cr}. To činimo uspoređivanjem kumulativnih funkcija raspodjele (distribucije) lokalnih gustoća galaksija, dobivenih provođenjem Voronoi teselacije na dva različita uzorka galaksija, gore opisanom
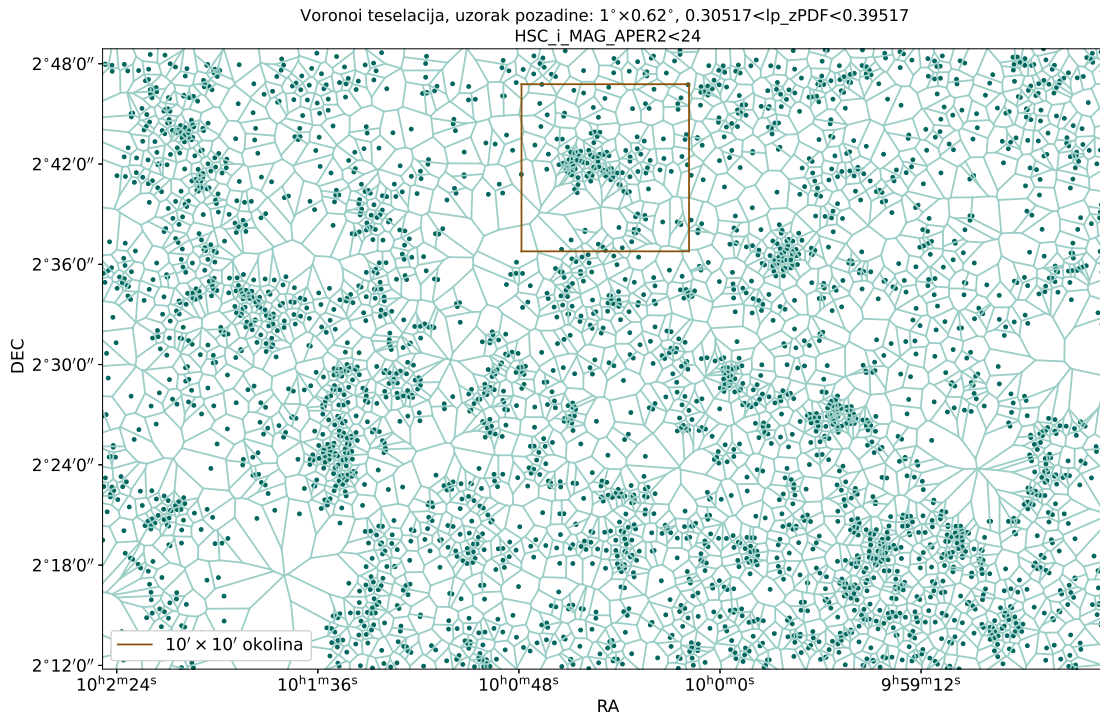
Slika 7.9: Voronoi teselacija na većem uzorku sa svojstvima pozadine. Uzorak galaksija filtriran je po magnitudi prema $i < 24$. Svaka točka je jedno Voronoi sjeme, odnosno jedna galaksija, a linije označavaju granice Voronoi ćelija.

uzorku $10' \times 10'$ okoline te na većem uzorku, koji ima svojstva pozadine. Uzorak sa svojstvima pozadine dobiven je izdvajanjem veće površine na nebeskoj sferi, centrirane na istim koordinatama. U trećoj dimenziji, širina ovog uzorka odgovara širini uzorka $10' \times 10'$ okoline. Ovako izdvojen uzorak galaksija obuhvaća više područja slabe, srednje i povećane gustoće, dok je očekivano da će u $10' \times 10'$ okolini radioizvora biti višak područja povećane gustoće (zbog potencijalno gravitacijski vezanih struktura). Voronoi dijagrami, izrađeni provođenjem Voronoi teselacije na uzorcima $10' \times 10'$ okoline radioizvora i pozadine (oba filtrirana prema $i < 24$), prikazani su na slikama 7.8 i 7.9. Pripadne kumulativne funkcije raspodjele lokalne gustoće prikazane su na slici 7.10. Vizualnom usporedbom, određujemo gdje (pri kojoj gustoći izvora) se funkcije počinju značajno razlikovati. Tu graničnu vrijednost gustoće uzimamo kao prag (ρ_{cr}) na kojem se strukture poput grupa galaksija, u $10' \times 10'$ okolini, počinju značajno isticati u odnosu na pozadinu. Granična vrijednost ρ_{cr}, određena opisanom metodom, pomalo je proizvoljna, zbog čega je treba shvatiti više kao procjenu, nego kao točnu vrijednost. Istom metodom, analizirana je i prostorna raspodjela optičkih izvora u $10' \times 10'$ okolini sustava radioizvora s magnitudom $i < 25$. Pripadne kumulativne funkcije raspodjele prikazane su na slici
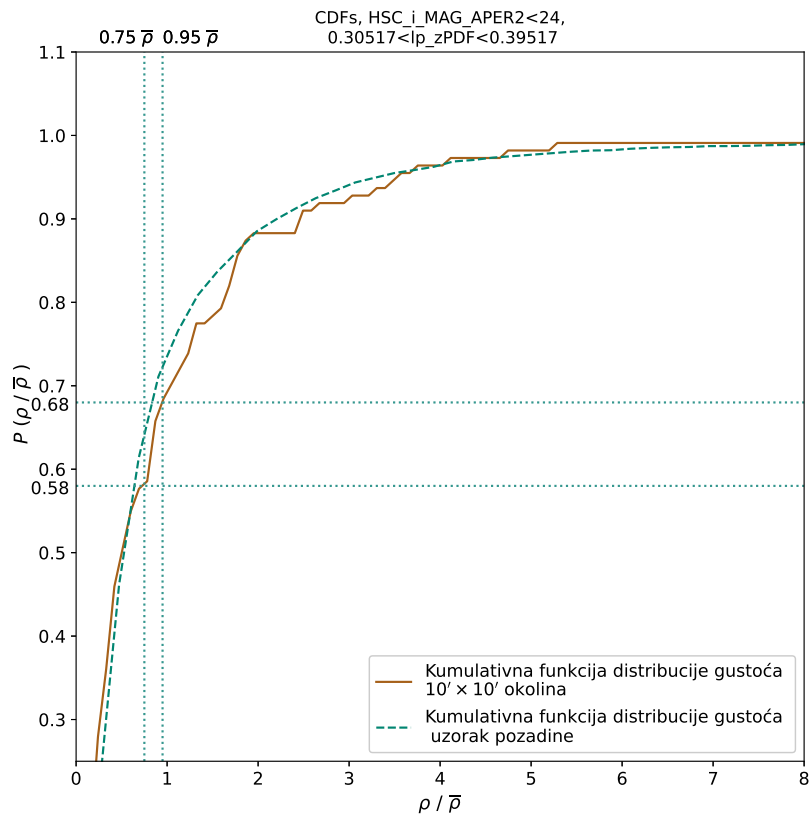
Slika 7.10: Usporedba kumulativnih funkcija raspodjele lokalne gustoće galaksija za dva različita uzorka, $10' \times 10'$ okolina sustava radioizvora i veći uzorak sa svojstvima pozadine. Uzorci su filtrirani prema uvjetu na magnitudu $i < 24$. Izdvojene su dvije vrijednosti lokalne gustoće (na pomalo proizvoljan način) na kojima se funkcije počinju značajno međusobno razlikovati: $0.75\,\overline{\rho_{env}}$ na $58.$ percentilu, i $0.95\,\overline{\rho_{env}}$ na $68.$ percentilu.

7.11. Konačni rezultati za slučaj $i < 24$, odnosno $10' \times 10'$ okolina radioizvora filtri-rana ($\rho > \rho_{cr}$) prema pragovima gustoće ρ_{cr} određenim usporedbom kumulativnih funkcija, prikazani su na slici 7.12. Za slučaj $i < 25$, konačni rezultati prikazani su na slici 7.13. Rezultati analize provedene nad uzorkom filtriranom prema $i < 24$ slični su onima u slučaju $i < 25$. Glavna je razlika u tom što, u prvom slučaju, od početka radimo s manje izvora, pa nakon primjene filtera za gustoću ($\rho > \rho_{cr}$) također ostaje manje izvora. U oba slučaja, uočavamo veću koncentraciju galaksija u centru, koja se prostorno poklapa s grupom galaksija prethodno detektiranom u rendgenskom po-dručju. Unutar ove koncentracije, uočljive su podstrukture, od kojih se najbolje ističe nakupina galaksija oko radioizvora 4092 u istočnom dijelu[43]. U zapadnom dijelu koncentracije, galaksije su također zgusnute, ali nije jasno priklanjaju li se neke od njih više izvoru 10913 ili 44. Moguće je da se ovdje radi o spajanju manjih grupa

---

[43]Istok je na lijevo na svim slikama
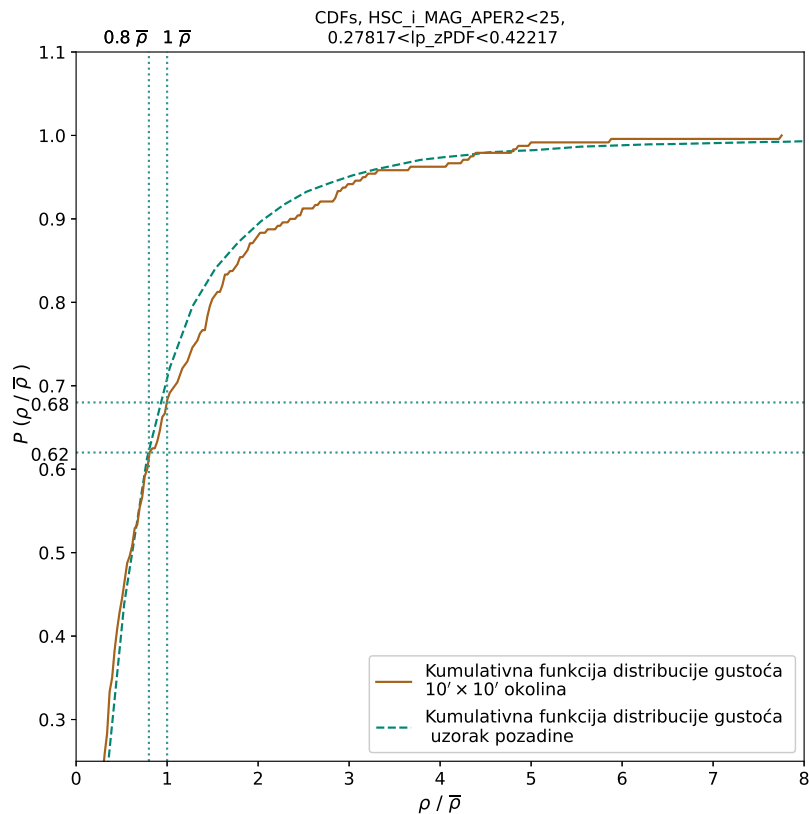
Slika 7.11: Usporedba kumulativnih funkcija raspodjele lokalne gustoće galaksija za dva različita uzorka: $10' \times 10'$ okolina sustava radioizvora i uzorak sa svojstvima pozadine. Uzorci galaksija su filtrirani prema uvjetu na magnitudu $i < 25$. Dvije vrijednosti gustoće izdvojene su na slici kao vrijednosti gdje se funkcije počinju značajno međusobno razlikovati: $0.8\, \overline{\rho_{env}}$ na 62. percentilu, i $1\, \overline{\rho_{env}}$ na 68. percentilu.

galaksija (potencijalno smještenih oko različitih radioizvora), pri čemu su potencijalne grupe oko radiogalaksija 10913 i 44 međusobno u naprednijoj fazi spajanja u odnosu njihovo spajanje s potencijalno trećom grupom oko radioizvora 4092, koja se približava s istoka.

7.6 Dijagrami magnituda-boja

Nakon analize prostorne raspodjele galaksija u $10' \times 10'$ okolini sustava tri radioizvora te izdvajanja onih iz gušćih područja, na ovom posljednjem uzorku, istražujemo vezu između luminoziteta (magnituda) i boje (indeksa boje) galaksija. To činimo izrađujući dijagrame magnituda-boja. Takvi dijagrami (za galaksije) obično se sastoje od tri različita područja/oblika: crveni niz, plavi oblak i zelena dolina. Crveni niz uglavnom sačinjavaju eliptične galaksije sa starom zvjezdanom populacijom te koje se često nalaze u skupovima/grupama galaksija. Plavi oblak sačinjavaju uglavnom

Slika 7.12: Konačni rezultati Voronoi teselacije provedene na uzorku $10' \times 10'$ okoline filtriranom prema $i < 24$. Prikazane su samo galaksije (tamno plave točke) iz područja gdje je lokalna gustoća veća od praga gustoće $\rho > \rho_{cr}$, za dva različita praga: $\rho_{cr} = 0.75\overline{\rho_{env}}$ i $\rho_{cr} = 0.95\overline{\rho_{env}}$. Svjetloplavi krugovi i poligoni označavaju maskirana područja iz COSMOS CLASSIC kataloga [40]. Tri radioizvora (odnosno njihovi optički ekvivalenti) istaknuti su tamnosmeđim krugovima, a njihove radiokonture prikazane su u svjetlosmeđoj boji.

Konačan rezultat Voronoi teselacije: 10′ × 10′ okolina
0.27817<lp_zPDF<0.42217, HSC_i_MAG_APER2<25
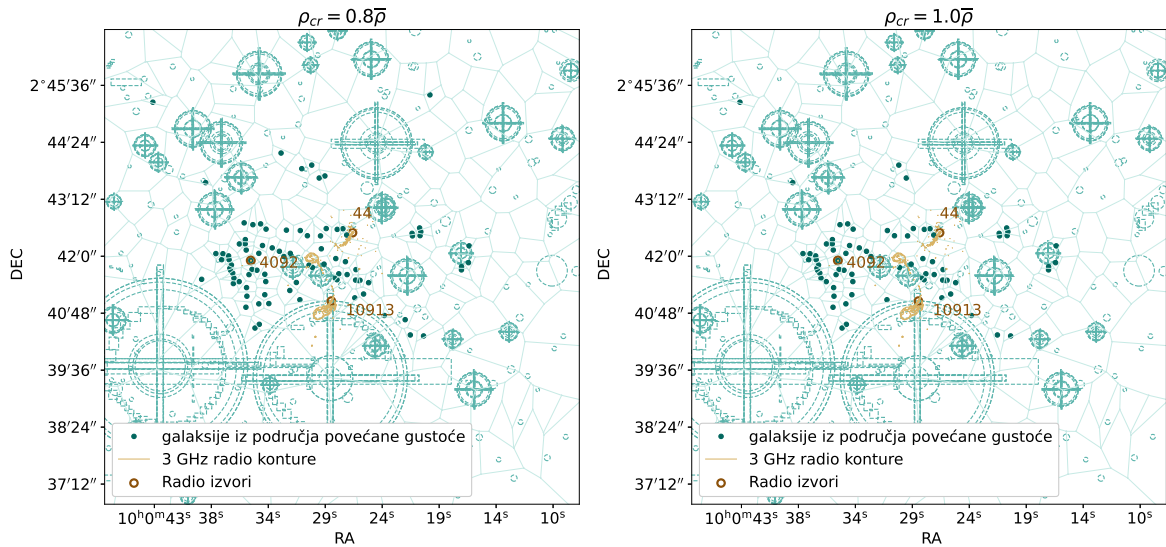
Slika 7.13: Konačni rezultati Voronoi teselacije provedene na uzorku $10' \times 10'$ okoline filtriranom prema $i < 25$. Prikazane su samo galaksije iz područja gdje je lokalna gustoća veća od praga gustoće $\rho > \rho_{cr}$, za dva različita praga: $\rho_{cr} = 0.8\overline{\rho_{env}}$ i $\rho_{cr} = 1\overline{\rho_{env}}$. Oznake i boje su iste kao na slici 7.12.

spiralne galaksije s mlađom zvjezdanom populacijom, odnosno u kojima još uvijek dolazi do formacije zvijezda. Zelena dolina je prijelazno područje. Ovo je prikazano na slici 7.14, a bitno je napomenuti da luminozitet galaksije kroz K_s filter dobro aproksimira njenu zvjezdanu masu (omjer mase i luminoziteta galaksije, engl. *mass-to-light ratio*)[13]. Detektiranje crvenog niza u dijagramu magnituda-boja za naš
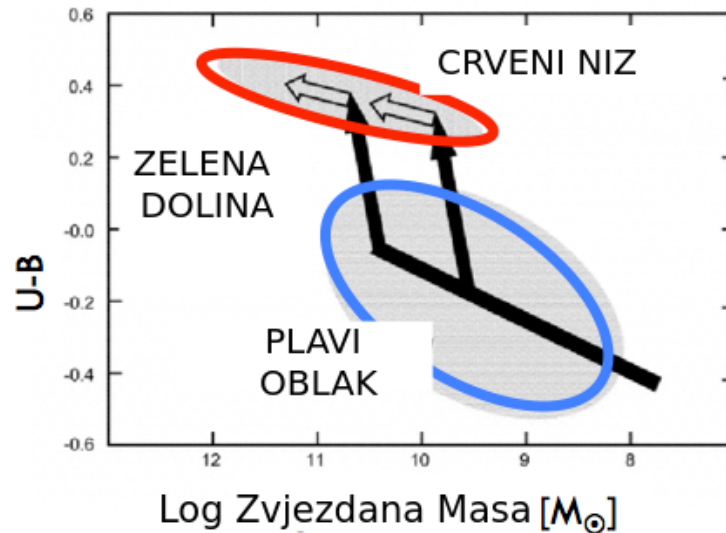
Slika 7.14: Tri različita područja/oblika koji se javljaju u dijagramima magnituda-boja za galaksije. Slika je preuzeta iz [6] te su engleski nazivi i oznake na dijagramu prevedeni na hrvatski.

uzorak galaksija (koje zadovoljavaju kriterij povećane gustoće), upućivao bi na to da se ovdje vjerojatno radi o grupi galaksija. Moguće je detaljnim proučavanjem izgleda, konkretno, oblika i debljine niza te eventualnim prepoznavanjem podstruktura u njemu, saznati više o raspodjeli optičkih izvora iz okoline radioizvora u trećoj dimenziji. Štoviše, proučavanjem kako prostorna raspodjela optičkih izvora unutar velike koncentracije (prethodno detektirane u rezultatima Voronoi teselacije i predstavljene u poglavlju 7.5) ovisi o njihovoj boji, može se otkriti više o dinamičkom stanju potencijalne grupe. Naime, u opuštenim grupama i skupovima, crvene galaksije su uglavnom smještene u njihovom centralnom dijelu, dok se plave nalaze u vanjskim dijelovima.

U svrhu izrade dijagrame magnituda-boja za galaksije, koristimo podatke o njihovim magnitudama kroz 3 različita filtera, preuzete iz COSMOS CLASSIC kataloga. Oduzimanjem vrijednosti magnituda kroz Subaru/HSC g i r filtere, dobivamo indekse boje. Filteri su birani tako da jedan bude centriran na manjim, a drugi na većim valnim duljinama od tzv. granice na 4000 Å (u sustavu galaksija), odnosno

≈ 5400 Å u sustavu iz kojeg se opaža (za galaksije na $z \approx 0.35$). Naime, poznato je da crvene galaksije imaju značajan pad fluksa ispod te vrijednosti, dok plave imaju mnogo fluksa. Centralne valne duljine ovih filtera su 4847 Å (za g) i 6219 Å (za r). Za treću magnitudu, koja je prikazana na x-osi dijagrama, koristimo Subaru/HSC i filter, čija je centralna valna duljina 7699 Å.
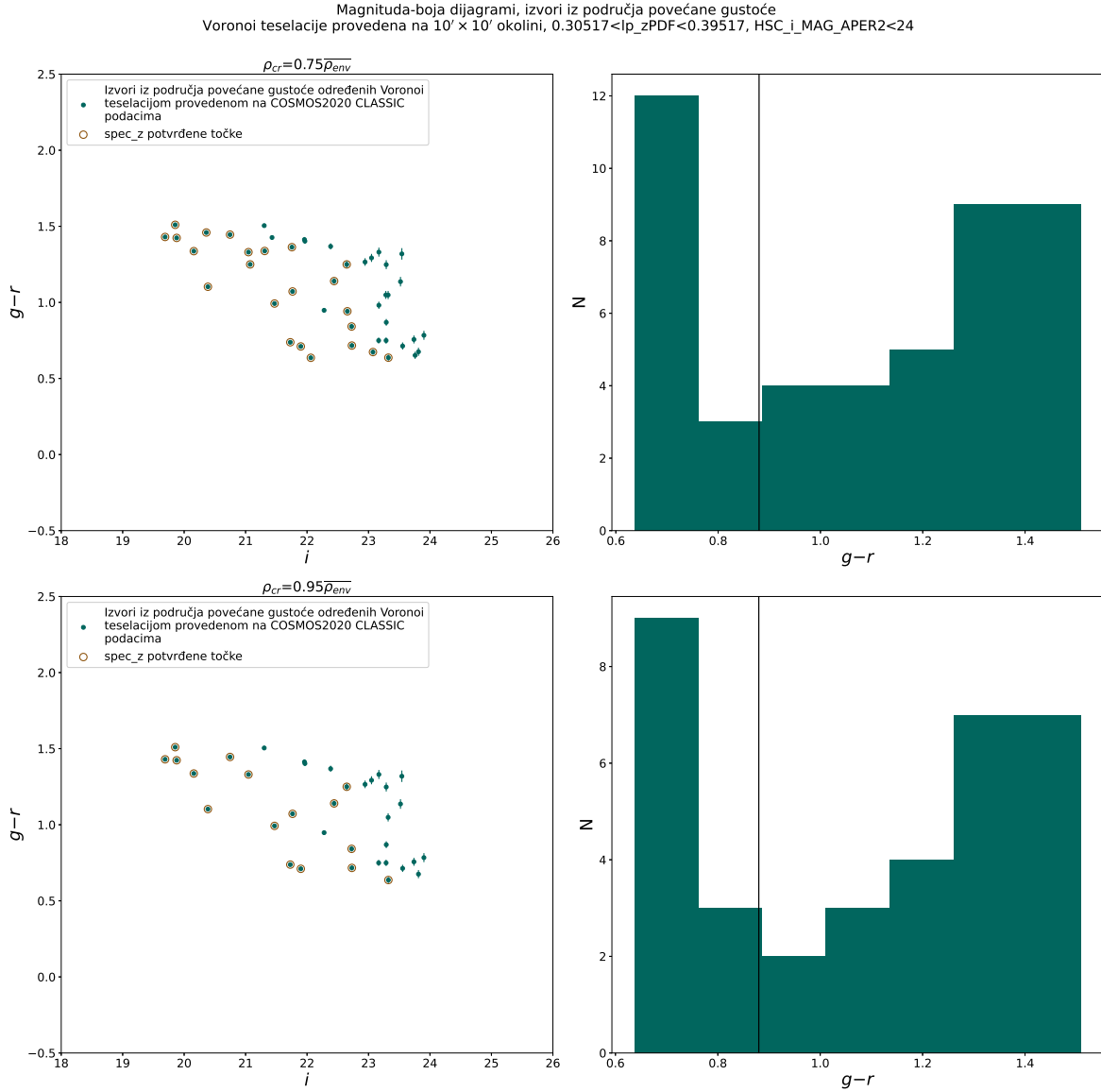
Slika 7.15: Magnituda-boja dijagrami za galaksije, izrađeni koristeći samo galaksije iz $i < 24$ uzorka koje pripadaju područjima povećane gustoće izvora ($\rho > \rho_{cr}$ za $\rho_{cr} = 0.75\overline{\rho_{env}}$ (gornji lijevi panel) i $\rho_{cr} = 0.95\overline{\rho_{env}}$ (donji lijevi panel)). Y-os prikazuje indekse boje, odnosno razlike magnituda opaženih kroz Subaru HSC g i r filtere (s pripadnim rasponima pogreške), a Subaru i magnituda je na x-osi. Galaksije koje imaju spektroskopske crvene pomake, i te vrijednosti su unutar raspona korištenog za filtriranje fotometrijskih crvenih pomaka prilikom izdvajanja $10' \times 10'$ okoline radioizvora, istaknute su svjetlosmeđim krugovima. Uz svaki od dva dijagrama, prikazan je i pripadni histogram indeksa boje (desni paneli), a crna linija na $g - r = 0.88$ predstavlja grubu granicu između plavijih i crvenijih galaksija.
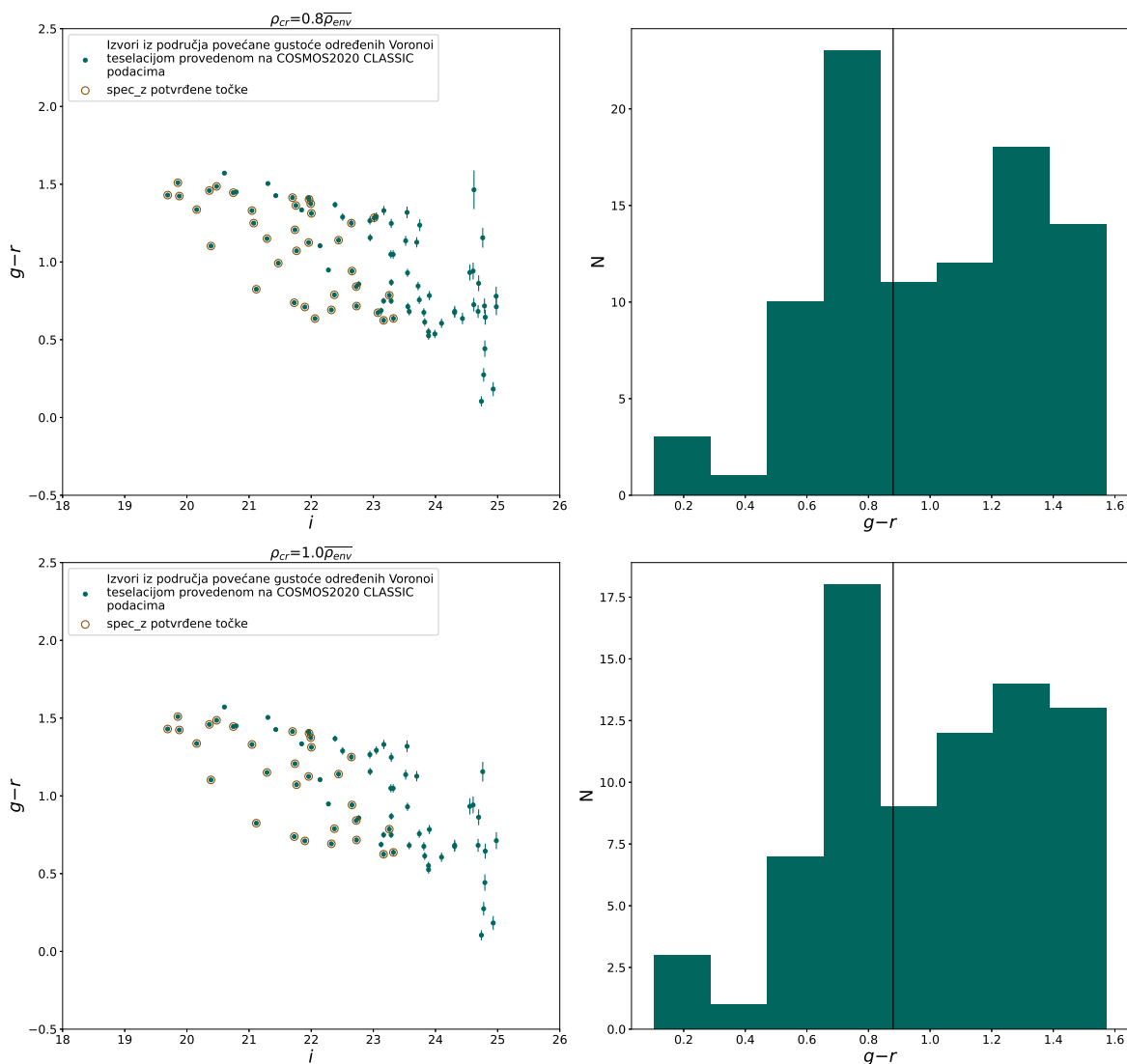
Slika 7.16: Magnituda-boja dijagrami za galaksije, izrađeni koristeći samo galaksije iz $i < 25$ uzorka koje leže u područjima povećane gustoće izvora ($\rho > \rho_{cr}$ za $\rho_{cr} = 0.8\overline{\rho_{env}}$ (gornji lijevi panel) i $\rho_{cr} = 1\overline{\rho_{env}}$ (donji lijevi panel)). Dijagrami su prikazani uz odgovarajuće histograme indeksa boje. Oznake i boje su iste kao na slici 7.15.

Dijagrame izrađujemo koristeći galaksije iz gušćih (gustoća izvora) područja u $10' \times 10'$ okolini radioizvora koji su izdvojeni $\rho > \rho_{cr}$ filterom. To radimo za oba uzorka galaksija, $i < 24$ i $i < 25$. U oba slučaja, određena su po 2 praga gustoće (ρ_{cr}) usporedbom kumulativnih funkcija raspodjele lokalnih gustoća dobivenih provođenjem Voronoi teselacije na uzorcima $10' \times 10'$ okoline i pozadine. Predstavljamo 4 dijagrama magnituda-boja za slučajeve: $i < 24$, $\rho_{cr} = 0.75\overline{\rho_{env}}$; $i < 24$, $\rho_{cr} = 0.95\overline{\rho_{env}}$; $i < 25$, $\rho_{cr} = 0.8\overline{\rho_{env}}$ te $i < 25$, $\rho_{cr} = 1\overline{\rho_{env}}$. Dijagrami su prikazani na slikama 7.15 za $i < 24$ slučaj, tj. 7.16 za $i < 25$ slučaj. Za svaki od dijagrama, izrađen je i pripadni histogram indeksa boje te je prikazan zajedno s dijagramom (desni paneli na
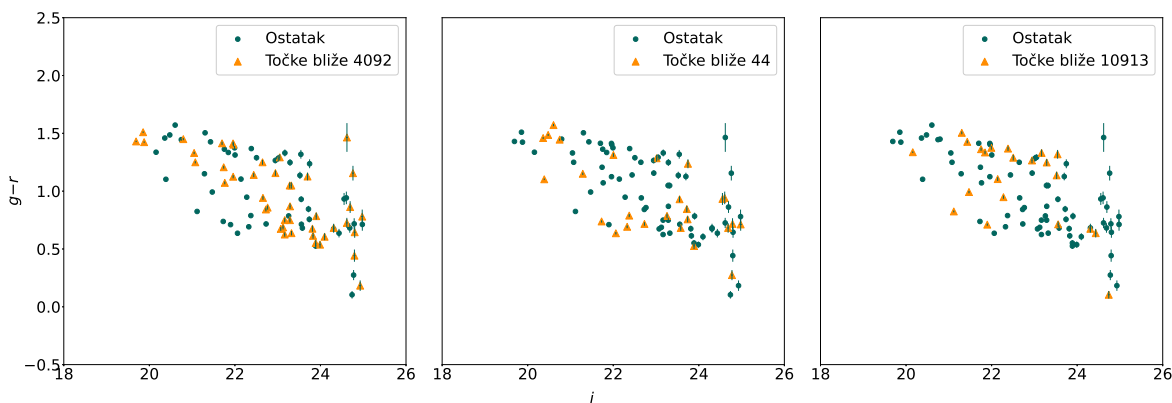
Slika 7.17: Dijagram magnituda-boja izrađen za galaksije iz $10' \times 10'$ okoline radioizvora, filtrirane prema $i < 25$, $\rho > 0.8\overline{\rho_{env}}$ te prikazan u tri različite verzije. U svakoj od verzija, posebno su označene (narančasti trokuti) galaksije koje su, u ravnini neba, bliže pojedinom od radioizvora: 10913, 44 i 4092. Ni u jednom od tri slučaja, ne postoji jasno uočljiv obrazac u ovisnosti položaja galaksije na dijagramu magnituda-boja o njenoj udaljenosti od pojedinog radioizvora.

slikama 7.15 i 7.16). Histogrami su izrađeni Numpy.histogram funkcijom u Pythonu, a pritom je broj odjeljaka određen opcijom bins='auto'. Odabirući tu opciju, dajemo Numpy.histogram funkciji da automatski odluči koja je najbolja metoda za izračun potrebnog broja odjeljaka na temelju broja podataka, a potom, koristeći odabranu metodu, izračuna optimalan broj odjeljaka.

Na dijagramima za slučaj $i < 24$ (slika 7.15), uočljiva je $\approx 6\,\mathrm{mag}$ dugačka, gotovo vodoravna struktura koja najvjerojatnije odgovara crvenom nizu. Takav rezultat predlaže da se ovdje vjerojatno radi o grupi galaksija. Slična struktura može se opaziti i u dijagramima magnituda-boja za slučaj $i < 25$. U tom slučaju, dijagrami sadržavaju više izvora, odnosno uključene su i manje sjajne galaksije ($24 < i < 25$). S uključivanjem ovih posljednjih, javljaju se i veće pogreške u magnitudama, pa tako i u indeksu boje. U oba slučaja ($i < 24$ i $i < 25$), niz je $\approx 1\,\mathrm{mag}$ širok (duž y-osi), što je moguće vidjeti i iz pripadnih histograma boje. Moguće je da bi niz bio manje širok, odnosno bolje definiran kad bi se ista analiza provela uz uporabu preciznijih, spektroskopskih crvenih pomaka, što valja biti dodatno istraženo u budućem radu.

Nadalje, istražujemo mogućnost da se ne radi o jednom, već o više crvenih nizova koji pripadaju potencijalnim, manjim grupama galaksija (moguće oko pojedinih radioizvora). U tom slučaju potencijalne grupe bi se spajale, tvoreći veću koncentraciju izvora koju opažamo. Takvi nizovi bi mogli biti na međusobno malo drugačijim crvenim pomacima, odnosno pomaknuti jedni u odnosu na druge duž y-osi. U svrhu
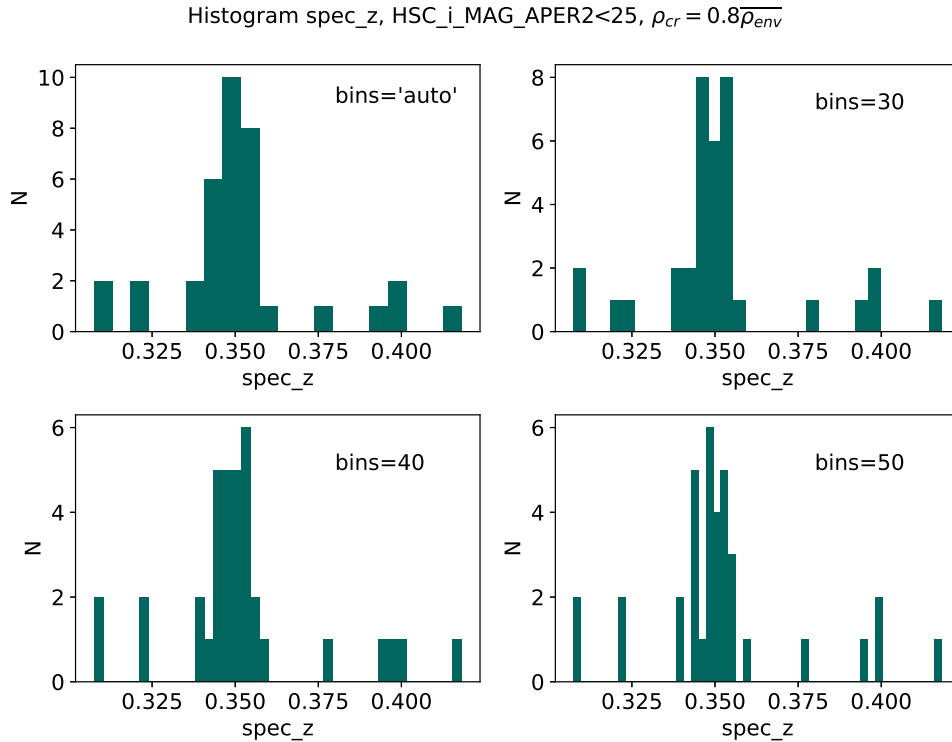
Slika 7.18: Histogram spektroskopskih crvenih pomaka galaksija iz uzorka $i < 25$, $\rho > 0.8\overline{\rho_{env}}$. Histogram je izrađen uz različite opcije broja odijeljaka: 'auto', 30, 40, i 50.

ispitivanja ove mogućnosti, proveden je jednostavan test, rezultati kojega su ovdje prikazani za provođenje na uzorku galaksija $i < 25$, $\rho_{cr} = 0.8\overline{\rho_{env}}$. Ti su rezultati konzistentni s onima koji se dobivaju provođenjem istog testa na preostala 3 uzorka ($i < 24$, $\rho_{cr} = 0.75\overline{\rho_{env}}$; $i < 24$, $\rho_{cr} = 0.95\overline{\rho_{env}}$ te $i < 25$, $\rho_{cr} = 1\overline{\rho_{env}}$). Izdvajamo sve izvore koji su, u ravnini neba, bliži pojedinom od 3 radioizvora, nego preostalim dvoma. Tako, dobivamo 3 skupine galaksija koje bi mogle biti članovi potencijalnih manjih grupa galaksija oko 3 radioizvora. Bitno je napomenuti da ovu metodu koristimo zbog njene jednostavnosti te da je, pri izdvajanju najvjerojatnijih članova potencijalnih, manjih grupa, moguće koristiti i druge, točnije metode što izlazi izvan okvira ovog rada. Podijelivši galaksije u 3 skupine, ponovo izrađujemo magnituda-boja dijagrame, ukupno njih 3. Pritom, u svakome od njih, posebno označavamo (ističemo) galaksije iz pojedine skupine u odnosu na ostale. Rezultati ovoga prikazani su na slici 7.17. Analizirajući rezultate, nije moguće reći da galaksije, iz bilo koje od ove tri skupine, formiraju zaseban crveni niz odvojen od ostataka. Izvori iz sve tri skupine protežu se duž čitave širine početnog niza ($\approx q\,\mathrm{mag}$). Više je mogućih razloga za ovakav rezultat, počevši od činjenice da radimo s manje preciznim, fotometrijskim cr-

venim pomacima. Također, moguće je da se zaista ne može detektirati više od jednog niza, odnosno da su različite potencijalne grupe međusobno vrlo blizu u trećoj dimenziji. Nadalje, moguće da je test, koji se oslanja isključivo na udaljenosti u ravnini neba, prejednostavan za ovaj slučaj, a također rezultati testa bi moguće bili drugačiji ako bi se za procjenu središta potencijalnih, manjih grupa galaksija koristila naprednija metoda (npr. središte rendgenske emisije). Moguće je i da se radi o kombinaciji nekih od ili svih gore navedenih razloga.
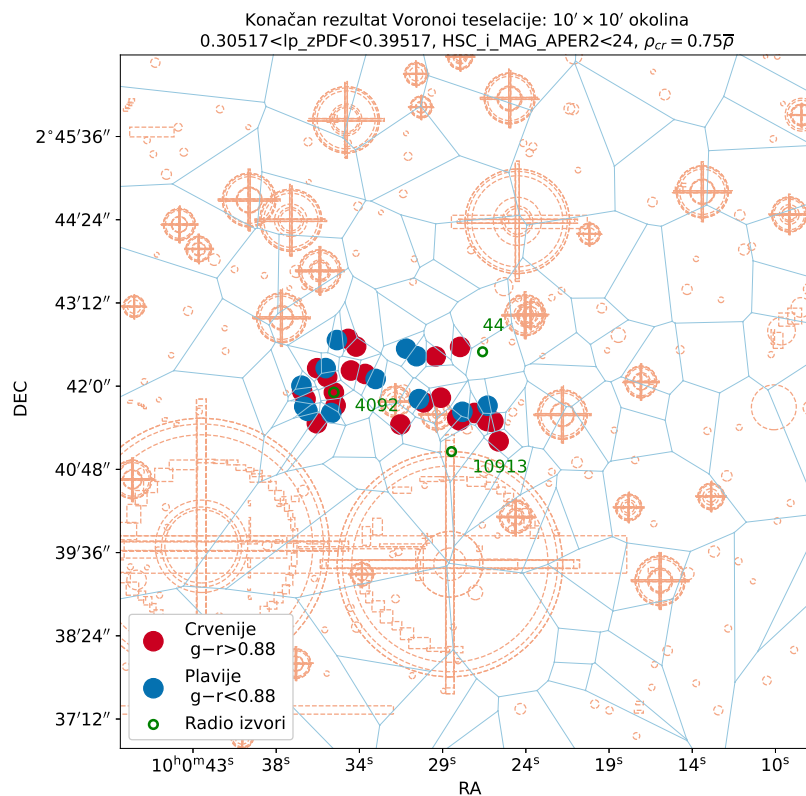
Slika 7.19: Podjela na plavije i crvenije galaksije u konačnom rezultatu Voronoi teselacije provedene na uzorku $10' \times 10'$ okoline radiogalaksija te filtrirane prema $i < 24$. Prikazane su samo galaksije koje zadovoljavaju uvjet $\rho > 0.75\overline{\rho_{env}}$. Prezentirana slika odgovara onoj prikazanoj na gornjem lijevom panelu slike 7.12. Jedina razlika je da su galaksije prikazane u dvije različite boje (crvena i plava), ovisno o vrijednosti indeksa boje. Vrijednost indeksa boje iznad kojeg se galaksije smatraju crvenijima (0.88) grubo je procijenjena iz pripadnog histograma boje u gornjem desnom panelu slike 7.12.

Kako bismo bolje ispitali raspodjelu galaksija u trećoj dimenziji, provodimo još jedan, jednostavan test, koristeći preciznije spektroskopske crvene pomake. Ovdje prikazujemo rezultate za $i < 25$, $\rho_{cr} = 0.8\overline{\rho_{env}}$ uzorak galaksija. Koristeći spektroskopske vrijednosti crvenog pomaka za galaksije iz ovog uzorka (u slučaju da ih imaju) izrađujemo histograme vrijednosti crvenog pomaka, kako bismo ispitali je
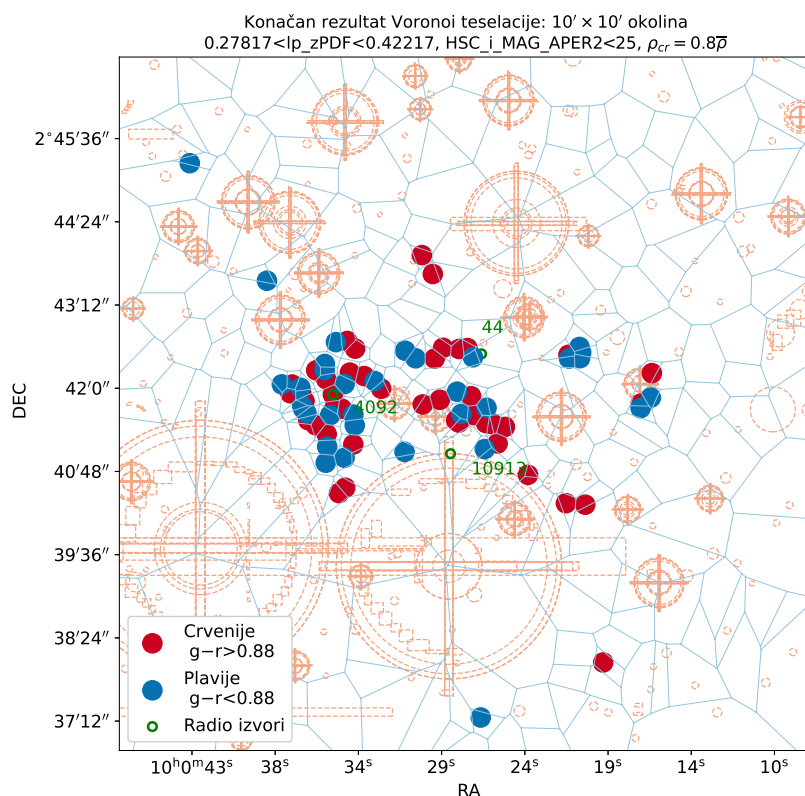
Slika 7.20: Podjela na plavije i crvenije galaksije u konačnom rezultatu Voronoi teselacije provedene na uzorku $10' \times 10'$ okoline radiogalaksija te filtrirane prema $i < 25$. Prikazane su samo galaksije koje zadovoljavaju uvjet $\rho > 0.8\overline{\rho_{env}}$. Prezentirana slika odgovara onoj prikazanoj na gornjem lijevom panelu slike 7.13. Jedina razlika je da su galaksije prikazane u dvije različite boje (crvena i plava), ovisno o vrijednosti indeksa boje. Vrijednost indeksa boje iznad kojeg se galaksije smatraju crvenijima (0.88) grubo je procijenjena iz pripadnog histograma boje u gornjem desnom panelu slike 7.13.

li moguće uočiti više od jednog vrha u histogramu, odnosno podstrukture unutar prethodno detektirane koncentracije galaksija u trećoj dimenziji. Izgled histograma malo se razlikuje u ovisnosti o broju odjeljaka koji se koriste. Stoga, na slici 7.18, prikazujemo rezultate za 4 različita odabira broja odjeljaka: 'auto', 30, 40 i 50. Opcija 'auto' prethodno je opisana u ovom poglavlju u kontekstu izrade histograma indeksa boje. Proučavajući histograme, nije moguće jasno uočiti više od jednog vrha, odnosno reći radi li se o jednoj ili više manjih nakupina galaksija na međusobno bliskim vrijednostima crvenih pomaka, koje se spajaju. U gornjem desnom kutu slike 7.18, histogram s 30 odjeljaka daje naznake o postojanju dva šiljka, ali na ostalim histogramima to nije vidljivo. Možemo zaključiti da, s ovim skupom spektroskopskih crvenih pomaka, nije moguće detektirati više od jedne koncentracije galaksija, koja se nalazi na $z_{\text{spec}} \approx 0.35$. Moguće je da skup podataka s kojima radimo, tj. nje-

gova brojnost, nije dostatna za detektiranje suptilnih razlika u crvenom pomaku i/ili da se potencijalni proces spajanja manjih koncentracija (potencijalnih manjih grupa) većinom događa u ravnini neba.

Naposljetku, istražujemo ovisi li položaj galaksija unutar velike, prethodno detektirane koncentracije o njihovoj boji te ako da, na koji način. Ovo radimo koristeći izvore iz dva različita (od ukupno 4) uzorka galaksija, $i < 24$, $\rho_{cr} = 0.75\overline{\rho_{env}}$ i $i < 25$, $\rho_{cr} = 0.8\overline{\rho_{env}}$. Kako bismo olakšali uočavanje potencijalne ovisnosti, točke koje označavaju galaksije prikazane su nešto većima. U oba slučaja, vizualno je procijenjena granica između plavijih (koje zapravo nisu zaista plave jer su njihovi indeksi boja i dalje pozitivni, vidi dijagrame magnituda-boja) i crvenijih galaksija na histogramu boje (slike 7.15 i 7.16). Ta granica prikazana je crnom linijom na histogramima na slikama 7.15 (gornji desni panel) i 7.16 (gornji desni panel). Ponovo prikazujemo konačne rezultate Voronoi teselacije (Voronoi dijagrame koji sadržavaju samo galaksije koje su zadovoljile uvjet gustoće $\rho > \rho_{cr}$) uz sljedeću razliku. Posebno, crvenom bojom, označavamo crvenije galaksije, a plavom bojom plavije galaksije. Ovo je prikazano na slici 7.19 za uzorak $i < 24$, $\rho_{cr} = 0.75\overline{\rho_{env}}$, odnosno na slici 7.20 za uzorak $i < 25$, $\rho_{cr} = 0.8\overline{\rho_{env}}$.

Iz ovako izrađenih dijagrama, možemo uočiti da postoji blagi višak plavijih izvora u istočnom dijelu velike koncentracije, oko radioizvora 4092. Ipak, i plaviji i crveniji izvori mogu se naći u unutrašnjim, kao i u vanjskim dijelovima velike koncentracije. Ovakav rezultat upućuje na to da je potencijalna grupa galaksija (koja bi odgovarala velikoj koncentraciji izvora) neopuštena.

7.7 Zaključak

U ovom radu, proučavani su radioizvori iz polja COSMOS: 10913, 44 i 4092, odnosno njihovi optički ekvivalenti te njihova $10' \times 10'$ okolina na optičkim valnim duljinama. Radiogalaksije 10913 i 44 imaju izduženu i savijenu radio morfologiju. Sva tri radioizvora prostorno su smješteni unutar masivne grupe galaksija, prethodno detektirane putem rendgenske emisije od međugalaktičkog medija. Ovo je konzistentno s činjenicom da se radiogalaksije (pogotovo one sa savijenim mlaznicama) često nalaze oko središta grupa i skupova galaksija. Glavni cilj ovog rada bio je istražiti navedeni sustav, odnosno tri galaksije i njihovu okolinu na optičkim valnim

duljinama, kao korak prema boljem razumijevanju kako njihovog savijenog oblika u radiovalnom području, tako i procesa nastajanja i razvoja grupe galaksija koja je njihov domaćin. Profili svjetla optičkih ekvivalenata tri radioizvora modelirani su softverom Galfit, a pritom je pretpostavljen Sersicov profil. To je rezultiralo Sersicovim indeksima: 3.946 ± 0.005, 4.77 ± 0.01 i 4.37 ± 0.02, za redom 10913, 44 i 4092. Prema rezultatima modeliranja (dobiveni parametri modela i rezidualne slike), čini se kako su optički ekvivalenti radiogalaksija 10913 i 44 eliptične galaksije, moguće s jezgrom, što je u skladu s očekivanjima. Rezultati modeliranja za optički ekvivalent radioizvora 4092 pokazuju kako središnji dio galaksije dobro slijedi Sersicov profil. Međutim, javlja se višak (rezidual) svjetla u vanjskim dijelovima galaksije, koji se ne može dobro modelirati istim Sersicovim profilom te treba biti dodatno istražen. Pogreške u dobivenim vrijednostima Sersicovog indeksa uglavnom su posljedica kombinacije nedovoljno dobro procijenjene svjetline neba te prejednostavnosti korištenih modela svjetla. U budućem radu, planirano je provođenje modeliranja uz korištenje naprednijih tehnika u procijeni svjetline neba i modeliranju. Nadalje, koristeći metodu Voronoi teselacije, analizirali smo prostornu raspodjelu optičkih izvora (galaksija) u $10' \times 10'$ okolini radioizvora. Uočena je povećana gustoća optičkih izvora oko tri radioizvora, što je očekivan rezultat s obzirom na to da je prethodno, na istom mjestu, detektirana grupa galaksija putem rendgenskog zračenja. Galaksije iz područja povećane gustoće, unutar $10' \times 10'$ okoline, izdvojene su kao najvjerojatniji članovi potencijalne grupe. Ovo je provedeno prema unaprijed procijenjenom pragu gustoće, tj. prema više različitih pragova s obzirom na to da je određivanje praga pomalo proizvoljno (te su prikazani rezultati za sve slučajeve, odnosno pragove). Neovisno o pragu koji je korišten, uočeno je da galaksije iz područja s povećanom gustoćom izvora formiraju veliku koncentraciju, koja se prostorno poklapa sa spomenutom grupom (detektiranom putem rendgenske emisije). Štoviše, uočene su i podstrukture unutar velike koncentracije galaksija, od kojih se najbolje ističe nakupina optičkih izvora oko radioizvora 4092. Postojanje ovakvih podstruktura može biti znak da potencijalna grupa galaksija nije opuštena. Za najvjerojatnije članove potencijalne grupe (galaksije iz područja povećane gustoće izvora, izabrane prema 4 različita praga gustoće ρ_{cr}) izrađeni su dijagrami magnituda-boja. Na dijagramima je jasno vidljiva gotovo vodoravna, $\approx 6\,\mathrm{mag}$ dugačka i $\approx 1\,\mathrm{mag}$ široka struktura. Vrlo vjerojatno se radi o crvenom nizu, što je u skladu s idejom da

se ovdje radi o grupi galaksija. Moguće je da bi širina niza, odnosno njegovo rasipanje u boji bilo manje kad bi se umjesto manje preciznih, fotometrijskih crvenih pomaka koristili spektroskopski crveni pomaci, što se treba dodatno istražiti u budućem radu. Nadalje, najvjerojatniji članovi potencijalne grupe galaksija podijeljeni su u dvije klase, crvenije i plavije galaksije, ovisno o njihovom indeksu boje. Proučavan je njihov raspored u prostoru (unutar velike koncentracije galaksija, odnosno potencijalne grupe) u ovisnosti o njihovoj boji. Obje klase, crvenije i plavije galaksije, prisutne su kako u središnjem, tako i u vanjskim dijelovima velike koncentracije (s nešto više plavijih u istočnom dijelu koncentracije, oko radioizvora 4092). Ovaj posljednji rezultat, uz ostale, ukazuje na to da potencijalna grupa nije opuštena. Moguće je da je opažena usred procesa svojeg nastajanja kroz spajanje različitih, manjih grupa galaksija. Ovakav scenarij bi potencijalno mogao objasniti savijen oblik mlaznica radiogalaksija 10913 i 44. Naime, takav oblik mogao bi biti posljedica njihovog međudjelovanja s međugalaktičkim medijem prilikom njihovog relativnog gibanja značajno velikom brzinom. Kako bi se bolje istražila ova mogućnost, potrebna je daljnja analiza, ne samo u optičkom području, već i na drugim valnim duljinama (posebice radiovalnim i rendgenskim).

7.8 HR nazivi slika i tablica

Nazivi slika

Nazivi tablica

References

[1] *Beers Timothy C. et al.* : Kinematics and Dynamics of the MKW/AWM Poor Clusters // aj. 1995. 109. pg. 874.

[2] *Begelman M. C. et al.* : A twin-jet model for radio trails // nat. 1979. 279. pg. 770–773.

[3] *Burns J. O.* : The structure and environment of the wide-angle tailed radio galaxy 1919+479. // mnras. 1981. 195. pg. 523–533.

[4] *Caltech .* : What is COSMOS? 2022. [Online; accesseed 31-Oct-2022] https://cosmos.astro.caltech.edu/page/public.

[5] *Condon James J., Ransom Scott M.* : Essential Radio Astronomy. 2016.

[6] *Faber S. M. et al.* : Galaxy Luminosity Functions to z~1 from DEEP2 and COMBO-17: Implications for Red Galaxy Formation // apj. 2007. 665, 1. pg. 265–294.

[7] *Fanaroff B. L., Riley J. M.* : The morphology of extragalactic radio sources of high and low luminosity // mnras. 1974. 167. pg. 31P–36P.

[8] *Gomez P. L. et al.* : The Cluster Dynamics, X-Ray Emission, and Radio Galaxies in Abell 578 = Abell 1569 // aj. 1997. 114. pg. 1711.

[9] *Gozaliasl G. et al.* : Chandra centres for COSMOS X-ray galaxy groups: differences in stellar properties between central dominant and offset brightest group galaxies // mnras. 2019. 483, 3. pg. 3545–3565.

[10] *Hyde J. B. et al.* : A search for the most massive galaxies - III. Global and central structure // mnras. 2008. 391, 4. pg. 1559–1576.

[11] *Joye W. A., Mandel E.* : New Features of SAOImage DS9 // Astronomical Data Analysis Software and Systems XII. 295. 2003. pg. 489. (Astronomical Society of the Pacific Conference Series).

[12] *Kluge M. et al.* : Structure of Brightest Cluster Galaxies and Intracluster Light // apjs. 2020. 247, 2. pg. 43.

[13] *Kodama Tadayuki, Bower Richard.* : The K_s-band luminosity and stellar mass functions of galaxies in z~1 clusters // mnras. 2003. 346, 1. pg. 1–12.

[14] *Koekemoer A. M. et al.* : The COSMOS Survey: Hubble Space Telescope Advanced Camera for Surveys Observations and Data Processing // apjs. 2007. 172, 1. pg. 196–202.

[15] *Krist John E. et al.* : 20 years of Hubble Space Telescope optical modeling using Tiny Tim // Optical Modeling and Performance Predictions V. 8127. 2011. pg. 81270J. (Society of Photo-Optical Instrumentation Engineers (SPIE) Conference Series).

[16] *Lallo Matthew D. et al.* : Temporal optical behavior of HST: focus, coma, and astigmatism history // Society of Photo-Optical Instrumentation Engineers (SPIE) Conference Series. 6270. 2006. pg. 62701N. (Society of Photo-Optical Instrumentation Engineers (SPIE) Conference Series).

[17] *Leauthaud A. et al.* : Weak Gravitational Lensing with COSMOS: Galaxy Selection and Shape Measurements // apjs. 2007. 172, 1. pg. 219–238.

[18] *Loewenstein M.* : Chemical Composition of the Intracluster Medium // Origin and Evolution of the Elements. 2004. pg. 422.

[19] *Loken C. et al.* : Radio Jet Propagation and Wide-Angle Tailed Radio Sources in Merging Galaxy Cluster Environments // apj. 1995. 445. pg. 80.

[20] *Malumuth Eliot M. et al.* : Dynamics of Clusters of Galaxies with Central Dominant Galaxies. I. Galaxy Redshifts // aj. 1992. 104. pg. 495.

[21] *Massey Richard et al.* : Pixel-based correction for Charge Transfer Inefficiency in the Hubble Space Telescope Advanced Camera for Surveys // mnras. 2010. 401, 1. pg. 371–384.

[22] *McCracken H. J. et al.* : UltraVISTA: a new ultra-deep near-infrared survey in COSMOS // aap. 2012. 544. pg. A156.

[23] *Oegerle William R., Hill John M.* : Dynamics of cD Clusters of Galaxies. IV. Conclusion of a Survey of 25 Abell Clusters // aj. 2001. 122, 6. pg. 2858–2873.

[24] *Oklopčić A. et al.* : A wide-angle tail galaxy at z = 0.53 in the COSMOS field // memsai. 2011. 82. pg. 161.

[25] *Padovani P. et al.* : Active galactic nuclei: what's in a name? // aapr. 2017. 25, 1. pg. 2.

[26] *Peng Chien Y. et al.* : Detailed Structural Decomposition of Galaxy Images // aj. 2002. 124, 1. pg. 266–293.

[27] *Pinkney J. et al.* : 1919+479: Big WAT in a Poor Cluster // aj. 1994. 108. pg. 2031.

[28] *Rijksuniversiteit Groningen .* : Virialization. 2022. [Online; accesseed 30-July-2022] https://www.astro.rug.nl/ gpopp/actzoek/virialization.html.

[29] *Sakelliou I. et al.* : What bent the jets in 4C 34.16? // mnras. 1996. 283, 2. pg. 673–682.

[30] *Sakelliou Irini, Merrifield Michael R.* : The origin of wide-angle tailed radio galaxies // mnras. 2000. 311, 3. pg. 649–656.

[31] *Schinnerer E. et al.* : The VLA-COSMOS Survey. IV. Deep Data and Joint Catalog // apjs. 2010. 188, 2. pg. 384–404.

[32] *Schneider P.* : Extragalactic Astronomy and Cosmology. 2006.

[33] *Scoville N.* : The Cosmic Evolution Survey: COSMOS // From Z-Machines to ALMA: (Sub)Millimeter Spectroscopy of Galaxies. 375. 2007. pg. 166. (Astronomical Society of the Pacific Conference Series).

[34] *Smolčić V. et al.* : A Wide-Angle Tail Radio Galaxy in the COSMOS Field: Evidence for Cluster Formation // apjs. 2007. 172, 1. pg. 295–313.

[35] *Smolčić V. et al.* : The VLA-COSMOS 3 GHz Large Project: Continuum data and source catalog release // aap. 2017. 602. pg. A1.

[36] *Smolčić V. et al.* : The VLA-COSMOS 3 GHz Large Project: Multiwavelength counterparts and the composition of the faint radio population // aap. 2017. 602. pg. A2.

[37] *Swinburne University of Technology* . : Synchrotron emission. 2022. [Online; accessed 30-July-2022] https://astronomy.swin.edu.au/cosmos/S/Synchrotron+Emission.

[38] *Swinburne University of Technology* . : Elliptical galaxy. 2022. [Online; accessed 26-July-2022] https://astronomy.swin.edu.au/cosmos/E/Elliptical+Galaxy.

[39] *Swinburne University of Technology* . : Intra-cluster medium. 2022. [Online; accessed 30-July-2022] https://astronomy.swin.edu.au/cosmos/I/Intra-cluster+Medium.

[40] *Weaver J. R. et al.* : COSMOS2020: A Panchromatic View of the Universe to z 10 from Two Complementary Catalogs // apjs. 2022. 258, 1. pg. 11.

[41] *Wikipedia contributors* . : Spectral index — Wikipedia, The Free Encyclopedia. 2019. [Online; accessed 28-December-2021].

[42] *Wikipedia contributors* . : Radio galaxy — Wikipedia, The Free Encyclopedia. 2021. [Online; accessed 26-December-2021].

[43] *Wikipedia contributors* . : Sérsic profile — Wikipedia, The Free Encyclopedia. 2021. [Online; accessed 26-July-2022].

[44] *Wikipedia contributors* . : Elliptical galaxy — Wikipedia, The Free Encyclopedia. 2022. [Online; accessed 26-July-2022].

[45] *Zelinka I. et al.* : Intelligent Astrophysics. 2021.

[46] *de Gasperin F. et al.* : A radio spectral index map and catalogue at 147-1400 MHz covering 80 per cent of the sky // mnras. 2018. 474, 4. pg. 5008–5022.